



University of Kentucky
UKnowledge

Theses and Dissertations--Chemical and
Materials Engineering

Chemical and Materials Engineering

2015

SYNTHESIS, STRUCTURE, PROPERTIES AND APPLICATIONS OF NANOPOROUS SILICON AND PALLADIUM

Xu Jiang

University of Kentucky, jessie-jiang@hotmail.com

[Right click to open a feedback form in a new tab to let us know how this document benefits you.](#)

Recommended Citation

Jiang, Xu, "SYNTHESIS, STRUCTURE, PROPERTIES AND APPLICATIONS OF NANOPOROUS SILICON AND PALLADIUM" (2015). *Theses and Dissertations--Chemical and Materials Engineering*. 50.
https://uknowledge.uky.edu/cme_etds/50

This Doctoral Dissertation is brought to you for free and open access by the Chemical and Materials Engineering at UKnowledge. It has been accepted for inclusion in Theses and Dissertations--Chemical and Materials Engineering by an authorized administrator of UKnowledge. For more information, please contact UKnowledge@lsv.uky.edu.

STUDENT AGREEMENT:

I represent that my thesis or dissertation and abstract are my original work. Proper attribution has been given to all outside sources. I understand that I am solely responsible for obtaining any needed copyright permissions. I have obtained needed written permission statement(s) from the owner(s) of each third-party copyrighted matter to be included in my work, allowing electronic distribution (if such use is not permitted by the fair use doctrine) which will be submitted to UKnowledge as Additional File.

I hereby grant to The University of Kentucky and its agents the irrevocable, non-exclusive, and royalty-free license to archive and make accessible my work in whole or in part in all forms of media, now or hereafter known. I agree that the document mentioned above may be made available immediately for worldwide access unless an embargo applies.

I retain all other ownership rights to the copyright of my work. I also retain the right to use in future works (such as articles or books) all or part of my work. I understand that I am free to register the copyright to my work.

REVIEW, APPROVAL AND ACCEPTANCE

The document mentioned above has been reviewed and accepted by the student's advisor, on behalf of the advisory committee, and by the Director of Graduate Studies (DGS), on behalf of the program; we verify that this is the final, approved version of the student's thesis including all changes required by the advisory committee. The undersigned agree to abide by the statements above.

Xu Jiang, Student

Dr. Thomas John Balk, Major Professor

Dr. Thomas Dziubla, Director of Graduate Studies

SYNTHESIS, STRUCTURE, PROPERTIES AND APPLICATIONS OF
NANOPOROUS SILICON AND PALLADIUM

DISSERTATION

A dissertation submitted in partial fulfillment of the requirements for the
degree of Doctor of Philosophy in the College of Engineering
at the University of Kentucky

By

Xu Jiang

Lexington, Kentucky

Director: Dr. Thomas John Balk, Professor of Materials Engineering

Lexington, Kentucky

Copyright © Xu Jiang 2015

ABSTRACT OF DISSERTATION

Nanoporous (np) materials with pore size below 100 nanometers exist naturally in biological and mineral structures, and synthetic np materials have been used industrially for centuries. Np materials have attracted significant research interest in recent decades, as the development of new characterization techniques and nanotechnology allow the observation and design of np materials at a new level. This study focuses on two np materials: nanoporous silicon (np-Si) and nanoporous palladium (np-Pd).

Silicon (Si), because of its high capacity to store lithium (Li), is increasingly becoming an attractive candidate as anode material for Li ion batteries (LIB). One significant problem with using Si as an anode is the large strain that accompanies charge-discharge cycling, due to swelling of the Si during Li insertion and deinsertion. Np-Si offers a large amount of free volume for Li absorption, which could allow the anode material to swell without cracking. A new method to fabricate thin films of high-purity (100% Si content) np-Si, which is promising as an anode material for LIB, is demonstrated and discussed in this study. Microstructural characterization, chemical analysis, battery performance testing and mechanical behavior of thin film np-Si are discussed here.

Palladium (Pd) is considered an ideal and reliable hydrogen sensor and storage material, due to its fast response and selectivity for hydrogen gas. This research not only demonstrates a method to fabricate np-Pd thin films, but also proposes a method to fabricate bulk np-Pd. The uniformly crack-free and sponge-like np-Pd thin film provides high sensitivity to low concentrations of H₂, showing promise as a hydrogen sensor material. Stress changes during hydrogenation/dehydrogenation were measured using wafer curvature. For bulk np-Pd, ultra-fine pore sizes were achieved by electrochemically dealloying bulk PdNi alloy. Mechanical behavior of bulk np-Pd was studied using in-situ transmission electron microscopy (TEM). Scanning electron microscopy (SEM) and x-ray diffraction were also used to characterize the structure and morphology of np-Pd.

This doctoral research has involved the optimization of fabrication conditions and investigations of microstructural evolution during processing, yielding an improved understanding of the properties, mechanical behavior and potential applications of np-Si and np-Pd.

KEYWORDS: Nanoporous, Silicon, Palladium, Thin films, Microstructure, Mechanical behavior

Student's Signature

Date

SYNTHESIS, STRUCTURE, PROPERTIES AND APPLICATIONS OF
NANOPOROUS SILICON AND PALLADIUM

By
Xu Jiang

Dr. John Balk

Director of Dissertation

Dr. Thomas Dziubla

Director of Graduate Studies

August 24th, 2015

Date

To my husband Wei, my son Albert, Mom and Dad

ACKNOWLEDGMENTS

I would like to thank many people who have helped me for my PhD study, the research work presented in this dissertation would not have been possible without their support. First, I gratefully thank my advisor Dr. T. John Balk for his academic guidance and support, he encouraged me through every step through the past 5 years.

I thank all the members who serve as my committee: Dr. Yang-Tse Cheng who always inspired me with new ideas, Dr. Matthew J. Beck who always challenged me to think deeper, and Dr. Stephen E. Rankin who is always helpful to all my questions.

I thank Dr. J. Todd Hastings for serving as my outside committee member. I thank Dr. Fuqian Yang and Dr. Thomas Dziubla for serve as my DGS. I thank Dr. Jia Ye, Mr. Larry Rice and Dr. Dali Qian from EMC. I would also like to thank my colleagues as well as friends who shared discussions, knowledge and ideas: Lei Wang, Nicolas Briot, Phillip Swartzentruber, Dr. Ye Sun, Juchuan Li and all my group members.

I am also indebted to my family, my parents Chongxi Jiang and Lijuan Wang. Particularly, utmost appreciation to my husband Wei Wen and my little son Albert, whose love and encouragement promoted the accomplishment of this dissertation. This material is based upon work supported by the National Science Foundation under Grant No. CMMI-1301184. I also acknowledge support of the Electron Microscopy Center at the University of Kentucky. Thanks for University of Kentucky Graduate School and Department of Chemical and Materials Engineering for their financial support of this work. I am very thankful to all the people who had helped me to finish my doctoral study.

TABLE OF CONTENTS

LIST OF TABLES.....	vii
LIST OF FIGURES.....	viii
Chapter 1. Introduction	1
1.1 Introduction of nanoporous Si and nanoporous Pd	1
1.2 Motivation and hypotheses	3
1.3 Outline of dissertation	5
Chapter 2. Background	7
2.1 Nanoporous Si (np-Si) and lithium ion batteries (LIB)	7
2.1.1 Battery, LIB and Si anode LIB	7
2.1.2 Nanostructured Si anode LIB	12
2.2 Nanoporous-Pd based H ₂ sensor	15
2.2.1 H ₂ sensor and H-Pd system	15
2.2.2 Hydridation and dehydridation of np-Pd	17
2.3 Mechanical behavior of np structured materials	18
2.4 Deposition and Dealloying	21
Chapter 3. Experimental	24
3.1 Preparation of np-Si thin film.....	24
3.1.1 Deposition of SiMg precursor alloy thin film	24
3.1.2 Np-Si thin film preparation via dealloying	24
3.2 Preparation of np-Pd thin film	25
3.2.1 Deposition of PdNi alloy thin film	25
3.2.2 Np-Pd thin film preparation via dealloying.....	26
3.3 Preparation of bulk np-Pd.....	27
3.3.1 Vacuum arc-melting.....	27
3.3.2 Bulk np-Pd preparation via electrochemical dealloying	27
3.4 Characterization.....	28
3.4.1 SEM and EDS	28
3.4.2 TEM and in-situ TEM	29

3.4.3	XPS.....	32
Chapter 4.	Novel method for fabrication of nanoporous Silicon via dealloying in H ₂ O	33
4.1	Introduction	33
4.2	Experimental.....	35
4.3	Results and Discussion	36
4.3.1	Optimization of the SiMg precursor composition	36
4.3.2	Optimization of the dealloying procedure, morphology and film stress evolution during dealloying	40
4.3.3	Amorphous np-Si and crystallized np-Si	49
4.3.4	XPS study of the np-Si film	52
4.3.5	Thermal cycle stress study of the np-Si film	56
4.3.6	Approaching micro-meter thick np-Si film.....	57
4.4	Summary	60
Chapter 5.	Nanoporous Si thin film negative electrode lithium ion battery	62
5.1.	Introduction	62
5.2.	Experimental.....	64
5.3.	Results and discussion	66
5.4.	Summary	74
Chapter 6.	Mechanical behavior of nanoporous Silicon.....	75
6.1	Introduction	75
6.2	Experimental.....	77
6.3	Results and Discussion	78
6.4	Summary	89
Chapter 7.	Response of nanoporous Palladium thin films to hydrogen gas	90
7.1	Instruction.....	90
7.2	Experiments	91
7.3	Results and Discussion	93
7.4	Summary	101
Chapter 8.	Transfer from single layer np-Pd to multi-layer np-Pd thin films	103
8.1	Introduction	103

8.2	Experimental	104
8.3	Results and Discussion	105
8.4	Summary	112
Chapter 9.	Bulk nanoporous Pd with ultra-fine pore size.....	114
9.1	Introduction	114
9.2	Experimental	115
9.3	Results and discussion	117
9.3.1	Microstructure study of np-Pd dealloyed from Pd ₁₄ Ni ₈₆ precursor alloy	117
9.3.2	Microstructure study of np-Pd dealloyed from Pd ₁₈ Ni ₈₂ precursor alloy	121
9.3.3	Microstructure study of np-Pd dealloyed from Pd ₂₀ Co ₈₀ precursor alloy.....	130
9.3.4	Micro-pillar compression test of bulk np-Pd	131
9.4	Summary	136
Chapter 10.	Conclusions and future work	137
10.1	Conclusion remarks.....	137
10.2	Suggestion for future work	139
Reference	142
Vita	149

LIST OF TABLES

Table 4.1 Chemical composition ratio of as-deposited Au interlayer sample.....	48
Table 4.2 Chemical composition ratio of as-dealloyed Au interlayer sample	49
Table 4.3 EDS result of the 100nm as deposited SiMg film.....	55
Table 4.4 Various dealloying precurdure that has been applied on to 600nm SiMg films	59
Table 8.1 Schematic diagram of 4 multilayer samples	106
Table 8.2 Composition of multilayer samples	107
Table 9.1 List of the free corrosion dealloying condition of Pd ₁₄ Ni ₈₆	118
Table 9.2 EDS spot scan result on the top layer of as-melted and as-dealloyed PdNi alloy.....	126
Table 9.3 XRD parameters and scan results of Ni, Pd and PdNi alloy	127

LIST OF FIGURES

Figure 1.1 Hypotheses schematic of the fabrication of np-Si and LIB cycling	4
Figure 2.1 The specific capacity of various electrochemically active metal elements	9
Figure 2.2 (a) Li-Si phase diagram (b) composition dependence of the potential in the Li-Si system	11
Figure 2.3 (a) Schematic of the multi-source magnetron sputtering system (b) The sputtering process.....	22
Figure 3.1 Si-Mg phase diagram.....	25
Figure 3.2 Flow chart of fabrication of np-Si thin film, the substrate is co-deposited with Si and Mg followed by dealloying with suitable etchant.....	25
Figure 3.3 (a) Schematic of in-situ TEM indentation (b) Wedge Si wafer	30
Figure 4.1 Variation of Si content along a Si-Mg compositional gradient sample. The locations marked (a)-(e) yielded porous structures during dealloying and were evaluated to identify the optimal precursor alloy for fabricating np-Si	39
Figure 4.2 Microstructures of np-Si created from precursor films with different Si content. Micrographs (a)-(e) correspond to the compositions indicated in Figure 4.1. The film in (c) exhibited the best microstructure in terms of open-cell porosity and interconnected ligaments	40
Figure 4.3 Microstructural evolution during dealloying, after (a) 1min, (b) 8 min,	

(c) 12 min, (d) 20 min, (e) 4 hours, (f) 18 hours, and (g),(h) 24 hours.

Pores appeared quickly during dealloying, although it took much longer

to establish a fully porous structure45

Figure 4.4 Film stress and Si content measured at different stages of dealloying.

The sample was removed from solution, rinsed and dried in order to

track the film stress. Composition was measured using witness samples

that were dealloyed along with the larger wafer used for measuring stress

.....46

Figure 4.5 Morphologies of np-Si films with different interlayers. (a) Ta interlayer;

(b) Ta and Si interlayers; (c) Si interlayer; (d) Cr interlayer; (e) Au

interlayer. In all cases, a stable open-cell structure was achieved,

although the average ligament size and structural details of the np

network varied with interlayer material48

Figure 4.6 EDS spectrum of the as-dealloyed Au interlayer sample49

Figure 4.7 Morphology of 200 nm np-Si film with Au interlayer (a) in the as-

dealloyed condition and (b) after vacuum annealing at 400 °C for 1 hour.

The ligament structure is coarser after annealing, but is still nanoporous

.....50

Figure 4.8 Micrographs (a)-(c) show TEM results for as-dealloyed np-Si: (a) BF

image, (b) selected area diffraction pattern from the np-Si film, (c) high

resolution image. The absence of diffraction spots in (b) and lack of

lattice fringes in (c) indicate that as-dealloyed np-Si is amorphous.

Micrographs (d)-(f) show TEM results for np-Si that was annealed at 400 °C in vacuum for 1 hour: (d) dark-field STEM image, (e) selected area diffraction pattern, (f) high resolution image. Images (d) and (f) indicate that the annealed np-Si is at least partially crystalline	51
Figure 4.9 TEM EDS line scan result	53
Figure 4.10 Depth profile scan of 100 nm as deposited SiMg film	55
Figure 4.11 The Si2p peak in the (a) as deposited film and (b) as dealloyed film	56
Figure 4.12 Thermal cycling stress evaluation of 100nm precursor np-Si thin film ...	57
Figure 4.13 Morphology of as dealloyed 300nm precursor film (a) and (b) plane view morphology, (c) cross section view	58
Figure 4.14 cross section images of (a) as deposited 600 nm film	59
Figure 4.15 Stress mapping of the as-deposited SiMg films (a) 500 nm as-deposited film (b) 100nm as-deposited film	60
Figure 5.1 (a) and (b) are SEM morphology of the sample Cr interlayer sample dealloyed with distilled water for 24 hours under different magnification; (c) and (d) are the as-deposited and as-dealloyed sample cross section, respectively	67
Figure 5.2 Cycling performance of 100nm np-Si with 10nm Cr interlayer anode sample cycled with C/5 rate	68
Figure 5.3 Morphology of the np-Si (10nm Cr interlayer) electrode after 30 cycles under different magnification	69
Figure 5.4 Cycling performance of RS-Au anode sample cycled with C/5 and C/10	

rate.....	70
Figure 5.5 Plane view of the np-Si (10nm Au interlayer) electrode (a) 200nm precursor film after dealloying before cycling (b) 100nm precursor film after dealloying before cycling, (c) the morphology of as-dealloyed 100nm precursor film anode after 30 cycles	71
Figure 5.6 The coulumbic efficiency of Cr and Au (100 and 200nm) interlayer coin cell cycled with different cycled rate	72
Figure 5.7 Plane view of the Kapton substrate np-Si electrode (a) and (b) are the morphology before cycling under different magnification (c) is the morphology after cycling	73
Figure 5.8 Cycling performance of np-Si with Kapton substrate anode sample cycled with C/5 and C/10 rate	73
Figure 6.1 Load displacement curve with strain range <10%	80
Figure 6.2 TEM images captured from in-situ indentation video upon above load displacement curve with strain range <10%, (a) before indentation (b) at the max deformation point (c) after indentation	80
Figure 6.3 (a) Load displacement curve with strain range 20%-30%, (b) Load displace curve of indentation 1 and 3.....	82
Figure 6.4 Series of video frames from in-situ indentation of np-Si thin film (a) immediately prior to loading (f) upon removal of load.....	85
Figure 6.5 Film thickness did not show noticeable change before and after indentation (a) before indentation (k) after indentation	86

Figure 6.6 Load displacement curve of 100nm film in-situ indentation.....	86
Figure 6.7 Load and displacement evolution during the above indentation	87
Figure 6.8 Load displacement curve with strain range 60%-70%	88
Figure 6.9 TEM images captured from in-situ indentation of large displacement (a)-(e) are from indentation curve 1 (f)-(j) are from indentation curve 2 ...	89
Figure 7.1 (a) and (b) are plan view of 100 nm precursor film dealloyed for 5 hours under different magnification; (c) the cross section view of the same film	94
Figure 7.2 (a) , (b) and (c) TEM images of the np-Pd thin film; (d) diffraction pattern of the film.....	95
Figure 7.3 (a) and (b) are stress map of 300nm film before and after dealloying, respectively	97
Figure 7.4 (a) Stress curve of 100 nm dense Pd film during H ₂ cycling measurement (b) Stress curve of 240nm np-Pd film during H ₂ cycling measurement	99
Figure 7.5 (a) Plot of stress change and partial pressure of H ₂ (b) Plot of log (stress change) and log (partial pressure of H ₂)	101
Figure 8.1 Morphology of ML2, pores are approximately 5.1 nm and ligaments are about 7.0 nm.....	108
Figure 8.2 Morphology of ML3 (a) plan view (b) cross section view.....	109
Figure 8.3 Morphology of M-4 (a) plan view, (b) and (c) are the cross section view under different magnification, (d) enlarge of the square marked region in (c) with its original scale bar.....	110

Figure 8.4 Cross section as dealloyed single layer 100nm precursor PdNi film	111
Figure 9.1 (a) dealloying in 25 °C H ₂ SO ₄ for 5 days (b) dealloying in concentrated H ₂ SO ₄ without surfactant at room temperature for 5 days (c) after 1st step dealloy in 25% H ₂ SO ₄ at 50 °C for 1 day, pores along the grain boundary. (d) after 2nd step dealloying, the sample in (c) keep dealloying in 25% H ₂ SO ₄ at room temperature for another 6 days	119
Figure 9.2 Linear sweep of Pd ₁₄ Ni ₈₆	120
Figure 9.3 Morphology of bulk Pd ₁₄ Ni ₈₆ after electrochemical dealloying (a) as dealloyed bulk Pd ₁₄ Ni ₈₆ surface morphology, (b) the morphology inside the sample as indicated in the white in (a), (c) surface cracks, (d) zoom in one spot of (b) shows np-Pd structure.....	121
Figure 9.4 (a) Linear sweep of Pd ₁₈ Ni ₈₂ and Ir wire holder (b) Dealloying current density evolution curve of Pd ₁₈ Ni ₈₂	122
Figure 9.5 Morphology of the Pd ₁₈ Ni ₈₂ after electrochemical dealloying for 14 hours (a) plan view (b) cracks on the surface and inside the sample (c) cross section view (d) dense top layer and np structure at the broken region (e) cross section view with dense top layer (f) ultrafine np-Pd structure with pore size 3-5 nm	124
Figure 9.6 Size statistics of ligaments and pore.....	125
Figure 9.7 BSE image of as dealloyed np-Pd (a) surface morphology (b) inside grain structure imaged by cutting a slot on the sample by FIB.....	126
Figure 9.8 XRD scan result of as arc melted Pd ₁₈ Ni ₈₂ alloy.....	127

Figure 9.9 The optical microstructure of the Pd ₁₈ Ni ₈₂ sample before and after annealing are showing in (a) before annealing (b) after annealing	128
Figure 9.10 (a) and (b) optical microstructure of the as annealed Pd ₁₈ Ni ₈₂ before dealloying, (c) and (d) are after dealloying	129
Figure 9.11 Morphology of the as annealed Pd ₁₈ Ni ₈₂ after electrochemical dealloying under different magnification.....	130
Figure 9.12 Morphology of as dealloyed Pd ₂₀ Co ₈₀ alloy under different magnification.....	131
Figure 9.13 Np-Pd pillar (a) a single pillar, and (b) cross section image after FIB...	131
Figure 9.14 Plots of (a) load vs. displacement and (b) load/displacement versus time. The increase in load near the end of the test (above 70 μ N load) is due to contact of the indenter tip with material surrounding the micro-pillar, and is therefore not indicative of sample behavior.	133
Figure 9.15 In-situ indentation test of np-Pd pillar (a) before indentation (b) indenter contact with the pillar (c) the max deformation point (d) after indentation.....	134
Figure 9.16 (a) Stress-Strain curve of np-Pd micro-pillar, (b) and (c) with a detailed showing the loading section from which elastic modulus was measured.	135

Chapter 1. Introduction

1.1 Introduction of nanoporous Si and nanoporous Pd

Nanoporous (np) materials have attracted significant research interest in recent decades as they have played an essential role in the design of new materials and applications [1, 2]. The recent rapid development of nanotechnology enables to study nanoscale materials with new characterization and observation techniques at the molecular and atomic level. This doctor work focuses on the synthesis and properties of two nanoporous materials: nanoporous silicon (np-Si) and nanoporous palladium (np-Pd).

As the second most abundant element on earth, Si has been considered as a promising negative electrode for lithium ion battery (LIB) as its extremely high theoretical capacity (up to 4212 mAh/g) [3]. However, a pure Si thin film electrode undergoes expansion/contraction during cycling lithiation and delithiation [4], during which the stress induced by these volume changes causes mechanical cracking and pulverization and thus results in the failure of the cells. Some degree of capacity fading over many cycles and increased polarization at higher current rates could possibly be due to the limited surface area accessible to the electrolyte and the continuous growth of solid electrolyte interphase (SEI) at the interface between the Si and electrolyte [5]. Np-Si has drawn great attention as the np structure providing sufficient room for the anode to swelling during the charge/discharge cycle. Some researchers has achieved 1000–2000 mAh/g capacities in nanostructured Si for hundred cycles, however, it is still far away

from their theoretical capacity [6]. Therefore, efforts are underway to improve existing battery technologies and develop new electrode for the next generation electrochemical devices. In this dissertation, a new method to fabricate np-Si thin film which could be used as negative electrode in LIB in the future will be demonstrated. Also, the mechanical properties of np-Si when its ligaments decrease to nanometers still lack of understanding. More research is needed to investigate the mechanisms of deformation and fracture of np-Si.

At room temperature and atmospheric pressure, Pd can absorb 900 times of its own volume of H_2 . Due to the excellent reactivity, fast response and selectivity for hydrogen gas, Pd has been considered an ideal and reliable material for hydrogen sensor and storage material [7]. Palladium hydride is metallic palladium that contains a substantial quantity of hydrogen within its crystal lattice. It is not an ionic hydride but rather an alloy of palladium with metallic hydrogen. At room temperature, palladium hydrides may contain two crystalline phases, α and β (sometimes called α') depending on different H/Pd stoichiometric ratio [8]. Pure α phase exists at H content less than $X < 0.017$ in PdH_x whereas pure β phase is realized for $X > 0.58$ in PdH_x while intermediate H content correspond to α - β mixtures. However, the pure Pd can not accommodate the large strain generated by the H insertion and extraction from the Pd lattice, which leads to the failure of the Pd sensor and storage applications [9]. Increasing the surface to volume ratio has been considered a key factor to improve the sensitivity and stability of the Pd-H applications, thus nano structured Pd with high

surface to volume ratio was developed to improve the H/Pd interaction. This research not only demonstrates a method to fabricate nanoporous palladium (np-Pd) thin films by dealloying precursor Pd alloys deposited by magnetron co-sputtering, but also demonstrates a method to fabricate bulk np-Pd by electrochemical dealloying.

1.2 Motivation and hypotheses

Motivated by the background as described in the introduction, a new type of structured Si anode which could overcome the disadvantages and present long cycle life without fading and cracking issues is needed in the future portable device development. The understanding of mechanical behavior of the as fabricated film is desired for the further LIB development.

Although the Pd based H₂ sensor has been commercially used, there are still drawbacks that hold up the development of these applications. For example, the response of Pd film sensor only function at high H₂ concentration and the film cracks due to the strain generated by the hydrogen cycling. Therefore, a reliable hydrogen sensing and storing material that has high response speed and storage ability needs to be developed.

For the np-Si part, this research will focus on the fabrication of np-Si thin film which will be used as the anode of LIB that is expected to provide high and stable specific capacity and long cycling life than existing Si anode LIB, as well as the mechanical behavior of the np-Si thin film. For the np-Pd part, this dissertation will focus on the hydrogen sensing performance of np-Pd thin film. The fabrication of bulk np-Pd and

its mechanical behavior will also be studied later in the thesis.

The hypotheses of this study include:

1. The hypotheses of the fabrication of np-Si and its lithiation/ delithiation cycling performance is shown in Figure 1.1. Novel np-Si that may provide alternatives to graphitic carbon could be developed by dealloying precursor Si alloy thin film. The np structure of the electrode would provide sufficient room for the lithiation and delithiation process and show well stability after a large number of electrochemical cycles. The np-Si anode materials will present better battery cycling performance than existing graphite anode LIB, Si thin film LIB and other structured Si anode LIB.

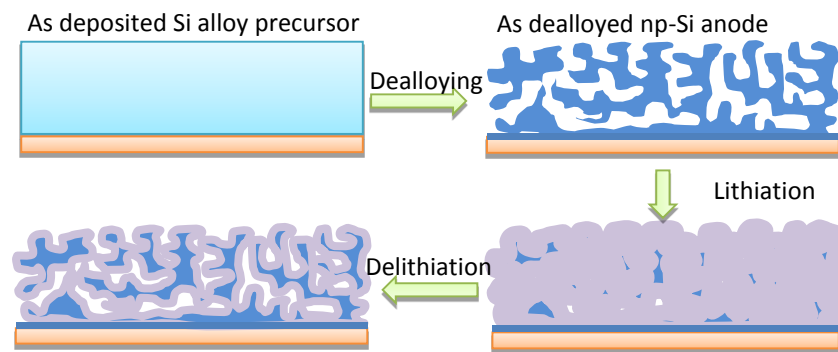


Figure 1.1 Hypotheses schematic of the fabrication of np-Si and LIB cycling

2. Brittle-ductile transition will be observed when the ligament size of np-Si varies. Nanostructured porous Si may present special deformation behavior due to the effect of nanoscale ligaments. The microstructure and ligament size will affect the deformation behavior of the np-Si thin films. Nanocrystalline np-Si (nc-np-Si)

could be made from the amorphous np-Si (a-np-Si) by suitable heat treatment. The nc-np-Si and a-np-Si would present different mechanical properties.

3. The sensing property of as fabricated np-Pd thin film will be tested under low H₂ concentration. The large surface area of the np structure would improve the sensitivity and the swelling ability of Pd during the hydrogen cycling.
4. Bulk np-Pd will be fabricated by dealloying bulk Pd alloys. The mechanical behavior of nano size ligament would be studied.

1.3 Outline of dissertation

The following is a brief outline of this dissertation.

Chapter 1 gives a brief introduction of this research, presents the hypotheses and motivation.

Chapter 2 introduces the background information that is necessary to understand this doctoral work. It includes the np-Si, np-Pd and their applications as well as the mechanical behavior and stress in thin films.

Chapter 3 describes the experimental details that involves in this research. The detailed fabrication process, specific equipment and characterization methods.

Chapter 4-9 contains the major studies related to this doctoral work. Chapter 4 discusses a novel fabrication method of np-Si thin film and its properties. Chapter 5 investigates the capacity of the np-Si thin film working as anode in LIB. Chapter 6 studies the mechanical behavior of the np-Si thin film under in-situ TEM indentation.

Chapter 7 describes the response capability of the np-Pd thin film to H₂ gas.

Chapter 8 presents the transition of single-layer np-Pd to multi-layer np-Pd.

Chapter 9 discusses the fabrication of bulk np-Pd and its in-situ indentation performance.

Chapter 10 is a summary of this thesis which includes remarkable conclusions and recommendations for future work.

Chapter 2. Background

2.1 Nanoporous Si (np-Si) and lithium ion batteries (LIB)

2.1.1 Battery, LIB and Si anode LIB

A battery is a device that converts the chemical energy contained in its active materials directly into electric energy by means of an electrochemical oxidation-reduction (redox) reaction [10]. This research will focus on the rechargeable batteries. The term of battery in the following context of this thesis refers to “rechargeable battery” for convenience. A battery consists of a number of voltaic cells either parallel or series. An individual cell is composed of three major components [10]:

- Anode (negative electrode): the reducing electrode - which gives up electrons to the external circuit and is oxidized during the electrochemical reaction.
- Cathode (positive electrode): the oxidizing electrode - which accepts electrons from the external circuit and is reduced during the electrochemical reaction.
- Electrolyte (the ionic conductor): provides the medium for transfer of charge, as ions, inside the cell between the anode and cathode which is typically a liquid.

During the discharge, the electrons flow from the anode, which is oxidized, through the external load to the cathode, where the electrons are accepted and the cathode material is reduced. The electric circuit is completed in the electrolyte by the flow of anions (negative ions) and cations (positive ions) to the anode and cathode, respectively. During the charge, which is a reversal process of the discharge, the current flow is reversed and oxidation takes place at the positive electrode while reduction happened

at the negative electrode. As the anode is, by definition, the electrode at which oxidation occurs and the cathode the one where reduction takes place, the positive electrode is now the anode and the negative the cathode.

Nowadays, the demand for portable power is growing due to the miniaturization of electronic devices like cell phones and vehicles [11, 12]. Reliable secondary rechargeable batteries of high energy and power density are needed for this rapidly growing demand. Among the various existing batteries, LIB is the most attractive one because Li is the most electropositive (-3.04V versus standard hydrogen electrode) as well as the lightest metal (standard atomic weight 6.941amu , and density 0.534 g/cm^{-3}) [13].

Group IV elements such as Si and Sn have been the main focus as LIB negative electrode metals owing to their high capacity. Si, as the second most abundant element on earth, has been considered as a promising negative electrode because of its extremely high theoretical capacity for Li ions compared with currently used carbon or graphite, as shown in Figure 2.1 [14]. The Si itself can alloy with Li up to $\text{Li}_{4.4}\text{Si}$, corresponding to 4212 mAh/g [15], which is more than ten times that of existing graphite anodes and various other oxide and nitride materials. Because of these attributes, a great deal of attention has been given to using Si as LIB anode material.

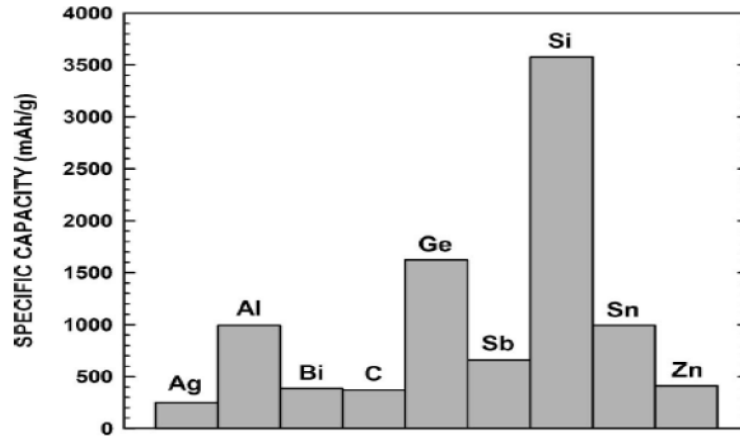


Figure 2.1 The specific capacity of various electrochemically active metal elements

Thin Si films have demonstrated the highest capacities and longest cycle lives due to the small amount of active material limiting total volumetric expansion. As reported by other researchers, Si films with thicknesses 50 nm or less exhibit the best reversibility and highest capacities. This amorphous Si thin film fabricated by vacuum deposition with nickel substrate exhibited an initial capacity of approximately 3750 mAh/g and a reversible capacity near 3800 mAh/g after 200 cycles at 1C cycle rate [16]. The performance of LIB with Si thin film electrode improves as film thickness decreases, consistent with the Griffith-Irwin relation, which states that the critical fracture stress increases as film thickness decreases [16, 17]:

$$\sigma_{fracture} = \frac{K}{\sqrt{\pi d}} \quad \text{Equation 2.1}$$

Where:

$\sigma_{fracture}$ is the critical fracture stress, K is the fracture toughness of the material, and d is the film thickness.

However, a pure Si electrode suffers from poor cycle ability due to mechanical cracking

caused by the volume change during the cycling expansion/contraction. The Si electrode undergoes cycles of compressive and tensile stresses, respectively upon lithiation and delithiation. The stress induced by these volume changes causes cracking and pulverization of the Si anode, leading to loss of electrical contact and eventual fading of capacity, which typically results in extremely limited cycle life [18]. Unlike intercalation electrodes such as graphite which presents the high reversibility and stable capacity over repeated cycling with only over 10% volumetric expansion during Li intercalation between the planar graphite layers, intermetallic alloy electrodes like Si suffer large volume changes and may go through multiple crystallographic phase transition during lithiation and delithiation [16]. The volume of Si anodes may change by about 200%–300% during cycling. Evidence has shown that there are four crystalline Li-Si phase exist according to the Li-Si phase diagram [19] [20] (Figure 2.2): $\text{Li}_{12}\text{Si}_7$, Li_7Si_3 , $\text{Li}_{13}\text{Si}_4$, $\text{Li}_{22}\text{Si}_5$, and each phase has a different open circuit voltage vs. Li. The formation of various Li_xSi_y phases generates enormous mechanical stress within the ionic character material, results in poor transport of electrons and rapid loss of the reversible capacity upon prolonged cycling (fading) [21-23]. As a result, Si films and particles tend to pulverize during cycling, much of the material loses contact with the current collector. Regarding these issues the degradation of the mechanical integrity of Si electrodes which leads to loss of electrical contact and eventual capacity fading is critical challenges associated with silicon-based anode materials [24].

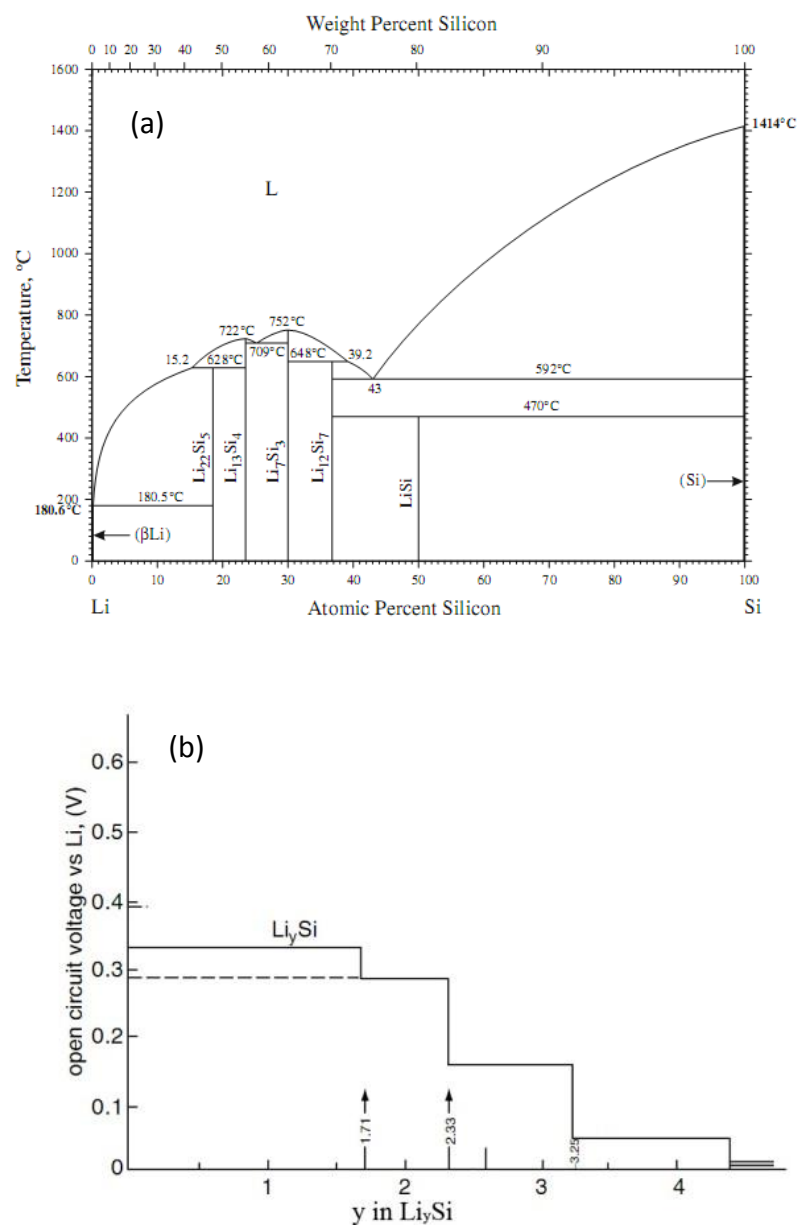


Figure 2.2 (a) Li-Si phase diagram (b) composition dependence of the potential in the Li-Si system

Previous studies about pure Si films electrodes in LIB have shown the capacity fading and short battery lifetime due to pulverization and loss of electrical contact between the active material and the current collector. J. P. Maranchi, et al. [25] examined the interfacial properties of a model active/inactive system comprised of an amorphous Si

thin film deposited on a polycrystalline Cu foil substrate. The crack pattern on 250 nm Si thin film presented after the first cycle. After 30 cycles, final decohesion of the Si island was formed. Juchuan Li, et al. [26] studied the fracture behavior and cracking patterns in amorphous Si thin film electrodes as a result of electrochemical cycling. The result shows that cracks are straight in thick films, but show more wiggles in thin films. As the thickness of film decreases, the average size of islands separated by cracks decreases. They claim that there might be a critical thickness below which material would not crack for amorphous Si films.

The volume change during discharge (lithiation) and charge (delithiation) would be compromised to some extent if the microstructure of the electrode materials could be designed properly. In order to alleviate the mechanical strain generated due to the volume change as the Li ions are inserted to and extracted from the host electrode materials, not only composite materials, but also nano sized particles and nanostructured materials have been studied in the past decades [27].

2.1.2 Nanostructured Si anode LIB

Properly structured materials could avoid the problems caused by Si swelling. Indeed, novel nanostructured materials have been explored for this purpose. Recently, the nano-scaled materials has been suggested as a possibility for next generation LIB since their physical, electrical and chemical properties are very different from those of their bulk materials [28]. Nanostructured Si like Si nanocomposites, nanowires, nanotubes and np-Si have received wide interest because of their good cycling performance as negative electrode material since the nanostructure provides sufficient room to

accommodate Si volume change and allows for facile strain relaxation without mechanical fracture during charge/discharge cycle.

Many researchers have studied the nanosized materials used for battery negative electrode. For example, Hyo-Jin Ahn, et al. [28] used Sn nanodots embedded Si electrode synthesized by co-sputtering as negative electrode for Li batteries. It showed very good (up to $600\mu\text{Ah}/\text{cm}^2\mu\text{m}$) reversible capacity during the Li insertion and extraction process for the first 15 cycles. Michael Holzapfel, et al. [23] developed a new type of nano-sized Si/carbon composite electrode. The $\sim 100\text{-}200\text{nm}$ composited electrode showed up to 1000 mAhg^{-1} specific capacity for the first 100 cycles with low fading.

Porous Si nanowires and nanotubes have been demonstrated to exhibit good cycling performance as anode materials since those structures provide empty space to accommodate Si volume changes and allow for strain relaxation without mechanical fracture upon during lithiation. Si nanowires and nanotubes have shown reversible capacities as high as approximately 3400 mAh/g [16]. Mi-Hee Park, et al. [29] demonstrated a method of prepared around hundreds Si nanotubes which showed about 3247 mAh/g reversible charge capacity by reductive decomposition of a Si precursor in an alumina template. Hui Wu, et al. [24] recently reported a double-walled Si nanotube (DWSiNT) electrode that retained more than 85% of its initial capacity after 6000 cycles. Due to this double wall design, the Li ions can penetrate through the outer wall and react with the inner Si wall during the lithiation and delithiation. The inner Si wall

expanded into the hollow space during lithiation and shrinks back during delithiation.

In this regard, when porous particles contain ordered pores, these pores act as a buffer layer for volume changes, demonstrating another means of controlling the volume expansion/contraction [15]. Chunyu Du, et al. [30] reported a simple, green, low cost and easy fabrication method of a novel Si electrode with a large amount of np by an in-situ thermal generating approach using triethanolamine as a sacrificing template. The np-Si electrode had ~200nm pore size void volume which largely accommodated the volume expansion during Li-insertion, gave the np-Si electrode up to 2200mAhg⁻¹ capacity for 100 cycles. However, the np structure collapsed after 50 cycles. Wei Chen, et al. [31] studied the porous Si anode LIB, which was prepared by the magnesiothermic reaction. Although the electrode showed very small pore size, the specific capacity experienced a rapid decreasing during 50 cycles.

In sum, although silicon anodes have great advantages over conventional graphite anodes in LIBs, there are still significant challenges need to be overcome before silicon anodes can be utilized in practical Li batteries. As discussed above, over the last decade, tremendous progress has been made in addressing these challenges by using nanostructured silicon anodes. Despite the variations of reported performance, a consistent trend has been emerging that storage capacities as high as 2000–2500 mAh/g for thin film silicon anodes and 1000–2000 mAh/g in other silicon nanostructure morphologies with rather impressive cycling lifetimes up to a couple hundred cycles at practical charge/discharge rate can be reproducibly achieved [16]. However, the

previously structured Si anode either had nonuniform macro/micro structure or large pore size ($\sim\mu\text{m}$). These materials exhibited increased polarization at higher current rates and some degree of capacity fading over many charging/discharging cycles, which could possibly be due to the limited surface area accessible to the electrolyte and the continuous growth of SEI at the interface between the Si and electrolyte [15]. Also, the fabrication of np-Si is non-environmental friendly as it always involve the dangerous acid HF. Therefore, efforts are still underway to improve existing battery technologies and develop new electrode reactions for the next generation of electrochemical devices. In this chapter, a new method to fabricate np-Si thin film which could be used as negative electrode in LIB in the future will be demonstrated.

2.2 Nanoporous-Pd based H₂ sensor

2.2.1 H₂ sensor and H-Pd system

Hydrogen has been drawing a lot of attention as a renewable clean energy source [32]. However, as a highly explosive and flammable but colorless, odorless and high diffusivity gas, the reliable, fast, accurate and economical hydrogen detector and safe storage method is needed for the safe use of hydrogen gas [33, 34]. There are various types of hydrogen micro-sensors, which use different mechanisms to detect the gas. Around all the alternative hydrogen detection materials, Pd has been considered as a promising candidate for hydrogen sensors, suitable hydride batteries, hydrogen storage materials and hydrogen separation membranes because of its excellent selectivity to hydrogen and high solubility of H in Pd [35].

Pd is used in many of the hydrogen sensors and storage applications because it

selectively absorbs hydrogen gas and forms the compound palladium hydride. The H-Pd system has been studied since first reported by T. Graham in 1866 [36]. Palladium hydride is metallic palladium that contains a substantial quantity of hydrogen within its crystal lattice. It is not an ionic hydride but rather an alloy of palladium with metallic hydrogen. When the H₂ molecules contact with Pd, the H₂ molecules first physisorb on the Pd surface by van der Waals forces and/or electrostatic attraction which closely depend on pressure and temperature. The physisorbed H₂ can dissociate into two H atoms then chemisorb with the surface Pd atoms. The H₂ readily dissociates on Pd surface and diffuse into the subsurface layer of the Pd, which makes the reaction between H and Pd spontaneous and reversible at room temperature. In the reaction of H with Pd, the H atoms occupy the octahedral sites in the face-centered cubic structure of Pd lattices. The Pd lattices near the surface deformed by the surface tension which causes a higher difficulty in H occupation at the octahedral sites. Instead, H atoms prefer tetrahedral sites near the Pd surface. H atoms can also reside at/near defects, including dislocation cores, grain boundaries and vacancies [37].

At low hydrogen pressure, Pd absorbs hydrogen in a solid solution (α -phase) with a low hydrogen concentration. When the hydrogen pressure increases, phase transition occurs at a certain hydrogen pressure (plateau pressure) to form a hydride in β -phase, which can contain hydrogen at a much higher concentration than the α -phase [38]. The miscibility gap between the hydrogen solubility of the α and β -phases indicates the hydrogen storage capacity of Pd.

Although Pd has the greater capacity to absorb hydrogen, the repeated volume change of the bulk Pd or thin film Pd material during the hydrogen absorption and desorption results in cracking, blistering and delamination. Also, most of the commercial Pd thin film sensors only have quick response at a relatively high H₂ concentration. The reliable and rapid detection sensor of low concentration H₂ is still desired to enhance the safe use of H₂.

2.2.2 Hydridation and dehydridation of np-Pd

Nanostructured Pd, with much larger contact area per volume has different hydrogen absorption/ desorption behavior from those of their bulk counterparts [39]. Nanoparticles [40], nanowires [41], and nano fibers [42], with higher surface area and shorter hydrogen diffuse distance, was studied to improve the sensing performance including the response time and accurate quantification of H₂ [43].

Narrowing of the palladium-hydrogen miscibility gap in nanocrystalline palladium has been studied by J. A. Eastman et al. [44]. The results claimed that the increasing of grain boundaries and/or strains in nanocrystalline Pd caused the entropy of mixing large than that in coarse grained Pd. The higher degree of atomic disorder in the lattices at/near Pd surfaces narrowed the miscibility gaps of the np structured Pd. In these nanostructured Pd materials, due to the effects of the large amount of surface and grain boundary, the distinction between the phases and phase becomes unclear. The effects of these nanostructure are expected to be different and understanding of them may be used to improve the H₂ sensing techniques [45, 46].

Over the past four decades, due to the high surface to volume ratio, the low dimensional Pd nanostructures such as Pd nanowires, Pd nanoparticles, np-Pd thin films have been develop for fast, sensitive and reliable H₂ sensor. Dongyan Ding et al. [47] reported a np-Pd film sensor supported by anodic aluminum oxides which had a relatively quicker response under hydrogen concentration as low as 250ppm. M Krishna Kumar et al. [48] studied a polycrystalline fcc nanostructured Pd thin film hydrogen sensor with a sensing time 10-20s. WenChun Li et al. reported the np-Pd thin film hydrogen absorption/desorption behavior. The as fabricated fine pore structure Pd presented high sensitivity upon Hydrogen exposure. Despite the various np-Pd have been developed, they are generally difficult to precisely measure H₂ with low concentration under 500 ppm with rapid response time [49]. Due to the demands of fast response, economic H₂ sensor and efficient H₂ storage material, reliable np structured Pd and its reaction mechanism with H₂ is still under development.

2.3 Mechanical behavior of np structured materials

Nanoporous structured materials with the internal pores and ligaments in nanometer scale usually have different mechanical properties from their bulk materials [50]. Because of the large surface to volume ratio in the np structured materials, the materials' property are more affected by the free surface while the elastic and plasticity response become more influenced by the length scale [51]. Due to the porous structure the deformation volume in the ligaments had been limited, which results in unique mechanical behavior. A basic conclusion for np materials was drawn as that the

nanophase materials may deform in a different way from its bulk materials when the materials grain size approaches 5-10 nm [52].

The Gibson and Ashby scaling law has been used to describe the mechanical properties of porous materials [53]. From these equations, the relative density of the foam materials as the dominating parameter of mechanical properties. According to Gibson-Ashby scaling law, the yield strength of an open cell foam is given by:

$$\sigma_y = C_1 \sigma_s (\rho_{np} / \rho_s)^n \quad \text{Equation 2.2}$$

Where:

σ_s and ρ_s are the yield strength and density of the solid materials, and ρ_{np} is the density of the porous counterpart. ρ_{np} / ρ_s is the relative density of porous materials. C_1 and n are empirical constants, with $C_1 = 0.3$ and $n = 3/2$ for many materials.

The yield strength of ligaments could also calculated by rewriting the above equation as:

$$\sigma_s = C_1^{-1} \sigma_y (\rho_{np} / \rho_s)^{-n} \quad \text{Equation 2.3}$$

However, some researchers also reported that the yield strength of np-Au is higher than it as predicted by this model. And the yield strength dramatic increased with decreasing of the submicron columns and wires size [54, 55].

Many researchers have been working on understanding the np materials' mechanical behavior in the past decade by the desire to create np structured material with unique functional performance. For example, the strength of nanoscale gold ligaments had

been measured by nanoindentation and reported to approach or even exceed the theoretical yield strength of bulk gold [56]. Many of the studies have been conducted with the aid of nanoindentation technique. Juergen Biener et al. [55] reported the dominant deformation mechanism during nanoindentation in np-Au was ductile plastic densification. The plastic deformation is confined to the area under the indenter, and adjacent areas are virtually undisturbed. Brittle fracture or crack emission was not observed, which clearly evidences the intrinsic ductile behavior of Au ligaments in np-Au. T. John Balk, et al. [57] studied the tension and compression properties of the np-Au by combining a fabrication approach and a microspecimen test technique. They claimed that although the macroscopic tensile behavior of np-Au micro-specimen was brittle, the failure of individual ligament appeared ductile. The cracked surface of individual ligament underwent extensive plastic deformation prior to rupture.

A variety of mechanical test techniques could be applied to investigate the mechanical properties of np materials such as tensile test, micro-pillar compression test, indentation test etc. [58]. Nanoindentation is one of the most applied method to measure the compressive strength, yield strength and Young's modulus. However, normal indentation test will not work when the sample is 2D dimension thin films with several nanometer ligaments size as the indenter is larger than the ligaments size and film thickness. Instead, in-situ TEM indentation is more effective and accurate for materials with nano scale. In-situ TEM nanoindentation technique is a recently developed technique that provides a unique possibility to study the deformation of the materials

when they are indented [56]. With this technique, the nucleation and motion of dislocations can be observed while a load-displacement curve is simultaneously recorded. It allows direct correlation of mechanical behavior measurement with microstructural changes. Ye Sun, et al. [56] studied the as-dealloyed crack free np-Au thin film by in-situ TEM indentation. The np structure of Au film compacted during indentation and became significantly denser with a corresponding decrease in electron transparency.

The research about the mechanical behavior, such as the tensile and compression behavior of the macro brittle material (like Si) is still unclear when its ligament size getting into nano-size. Also, the property difference between bulk Pd and np-Pd is still unclear in the past studies. The research of mechanical properties of np-Pd will contribute to understand the hydridation process of np-Pd.

2.4 Deposition and Dealloying

Sputtering deposition is a technique used to deposit thin films of a material onto a surface (substrate) by first creating gaseous plasma and then accelerating the ions from this plasma into some source material (target). Sputtering usually uses Argon plasma. Sputtered atoms ejected into the gas phase are not in their thermodynamic equilibrium state, and tend to deposit on all surfaces in the vacuum chamber. A substrate (such as a Si wafer) placed in the chamber will be coated with a thin film, as shown in Figure 2.3. Magnetron sputtering deposition which has high rate and ease of scaling is used in this research because of it could produce high quality as deposited thin films and hard

coatings. The magnetron sputtering uses magnets behind the cathode to trap the free electrons in a magnetic field directly above the target surface, thus there is no free electrons to bombard the substrate. The increase in available ions significantly increase the rate at which target material is eroded and subsequently deposited onto the substrate.

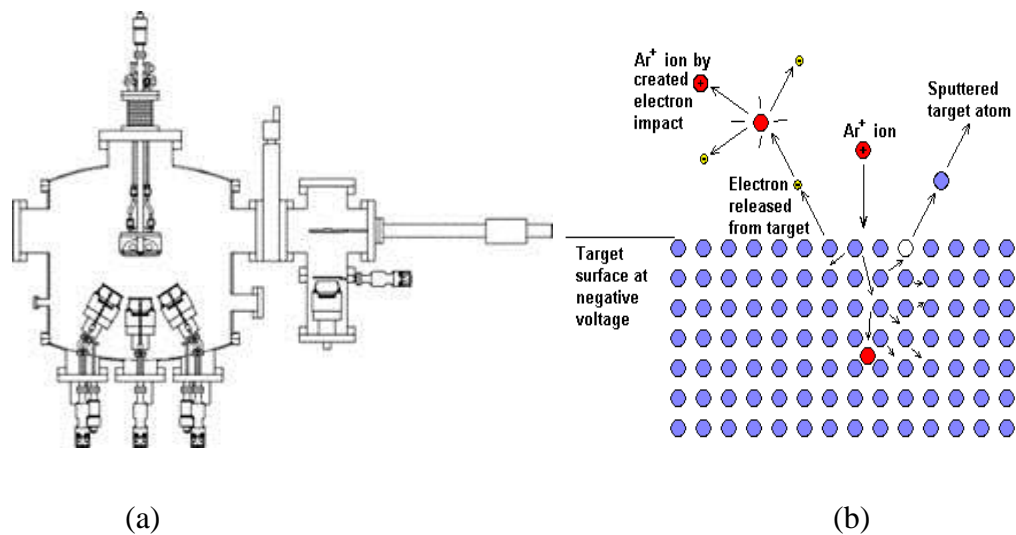


Figure 2.3 (a) Schematic of the multi-source magnetron sputtering system (b) The sputtering process

Dealloying, also called selective leaching, is a common corrosion process during which an alloy is ‘parted’ by the selective dissolution of the most electrochemically active of its elements. The less noble metal is removed from the alloy by microscopic-scale galvanic corrosion mechanism and results in the formation of a nanoporous sponge composed almost entirely of the more noble alloy constituents [59]. For dealloying to occur, the etchant must be able to selectively remove the sacrificial element(s) from the alloy, and thus a suitable element typically is less noble than the elements that are wished to retain. Under appropriate dealloying condition the as

fabricated np structure could exhibit a ligaments size for several nm. There are two types of dealloying, i.e. free corrosion and electrochemical dealloying, depending on if voltage is applied. The alloying elements and composition of the precursor alloy, concentration and temperature of dealloying etchant, dealloying time and applied voltage all have effects on the final dealloyed structure.

Dealloying of binary alloys in acidic solutions have been extensively applied to synthesize np films of various pure metals. Biener et al. [55] investigated the mechanical behavior of np-Au fabricated by dealloying Au-Ag precursor alloys. Pugh et al. [60] obtained np-Pt by electrochemically dealloying $\text{Cu}_{0.75}\text{Pt}_{0.25}$ precursor alloys. Wang et al. [61] fabricated several nanoporous metals by dealloying precursors that contained Mg as the sacrificial element. However, this approach has never been applied to semiconductor material systems. In this research, dealloying was conducted to SiMg alloy system to create Si thin film with nanoscale porosity. The fabrication and properties of both thin film np-Pd and bulk np-Pd were also investigated by dealloying thin film and bulk Pd alloys.

Chapter 3. Experimental

3.1 Preparation of np-Si thin film

3.1.1 Deposition of SiMg precursor alloy thin film

The SiMg precursor film was deposited by magnetron co-sputtering from Si and Mg targets (both 99.99% purity) in a high-vacuum chamber (AJA ORION system) at room temperature. The sputtering system had a base pressure $\sim 10^{-8}$ torr and a working pressure of 2.5×10^{-3} torr (Ar gas), with a substrate height being 55 mm above the confocal sputter guns and substrate pre-cleaning being performed by biasing with RF power (35 W) for 1.5 minutes at an Ar pressure of 2.5×10^{-2} torr. The same deposition conditions were applied for preparation of all samples. Various substrates, including (100)-oriented Si wafers with thickness of 180 μm , 230 μm , as well as 50 μm Cu foil and Kapton, were used in this study. Different interlayers, including Ta, Cr, Au and Si, were deposited before the SiMg precursor film in order to improve the adhesion and stability of Si films. More detailed deposition conditions will be discussed in Chapter 4.

3.1.2 Np-Si thin film preparation via dealloying

Si-Mg system was chosen in this research to fabricate the np Si where Mg offers several attractive features as a sacrificial element. Phase diagram of Si-Mg are shown in Figure 3.1 [62]. SiMg_2 (CaF_2 structure, eight Mg atoms are inside the face-centered cubic unit cell at $\pm 1/4, 1/4, 1/4$) is the only equilibrium intermediate alloy between the pure

elements. As shown in Figure 3.2, Si and Mg were deposited on substrates by magnetic sputtering followed by the as-deposited Si-Mg film being immersed in etchant to form porous structure through dealloying. To find the best dealloying etchant and synthesis approach, different dealloying procedures were evaluated and are discussed later in this paper.

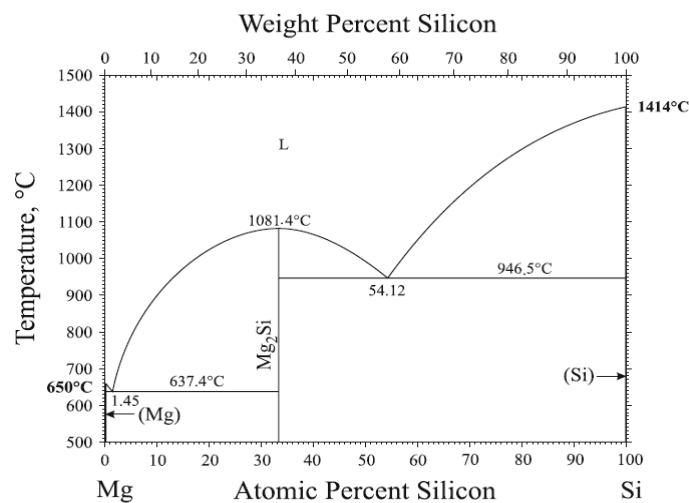


Figure 3.1 Si-Mg phase diagram

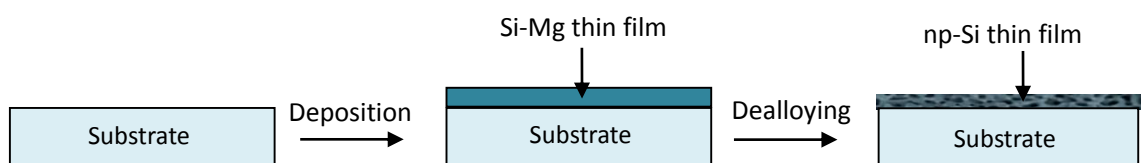


Figure 3.2 Flow chart of fabrication of np-Si thin film, the substrate is co-deposited with Si and Mg followed by dealloying with suitable etchant

3.2 Preparation of np-Pd thin film

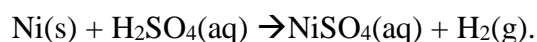
3.2.1 Deposition of PdNi alloy thin film

In this research work, an AJA (ORION system, AJA International Inc., North Scituate,

MA, USA) magnetron sputtering system was used to prepare the PdNi thin films in which the base and working pressure were $\sim 10^{-8}$ Torr and 2.5×10^{-3} Torr, respectively. Co-sputtering was carried out under an inert Ar gas atmosphere at 19.9 sccm at room temperature. The Sub-height was optimized to be 55 mm. The 180 μm -thick single crystalline Si wafers, oriented in (100) with 50 nm silicon nitride outer layers, were used as the substrate. Sub-clean was conducted on substrates with RF 35 W for 1.5 minutes at pressure 2.5×10^{-2} Torr before film deposition. To increase the adhesion of the PdNi films and balance the initial wafer stress, 2 nm Ta and 2 nm Pd interlayers were sputtered subsequently on both sides of the wafer substrate prior to the Pd-Ni alloy thin film deposition. These basic deposition parameters were kept same for all the following PdNi samples preparations in this research.

3.2.2 Np-Pd thin film preparation via dealloying

The np-Pd thin films were fabricated by free corrosion. The as-deposited Pd-Ni films were immersed in 25% (vol. %) sulfuric acid for several hours to process the dealloying, in which the sulfuric acid reacted with Ni as following:



To achieve the fine porous structure, Oleic acid and Oleylamine acid dissolved in the ethanol was used as the surfactant [63].

3.3 Preparation of bulk np-Pd

3.3.1 Vacuum arc-melting

Vacuum arc melting (VAR) is a secondary melting process for production of metal ingots with elevated chemical and mechanical homogeneity for highly demanding applications. Ni and Co were select as the sacrificial elements to fabricate the np-Pd via arc-melting followed with electrochemical dealloying. The bulk PdNi and PdCo samples were fabricated using compact Edmund Buhler GmbH MAM-1 vacuum arc melter. To achieve the optimized composition PdNi alloy that would yields the best np-Pd structure after dealloying, various proportion of pure Pd (99.9%) sheet, Co sheet (99.9%) and pure Ni (99.9%) pellet and were weighted and arc melted. Before each melting, the chamber was purged with 2.5 atm Ar gas for 4-5 times for 3 minutes each time. The samples were melted with Ar gas flow under 0.5 mbar absolute pressure and each sample was flipped 4-5 times to unify the Pd and Ni/Co distribution in the sample.

3.3.2 Bulk np-Pd preparation via electrochemical dealloying

Electrochemical dealloying was applied on as arc-melted Pd alloys to form the nanoporous structure with a potentiostat (eDAQ). The anodic polarization measurement was first conducted in 0.1mol/L H₂SO₄ to find the critical potential of the samples. In this three electrode electrochemical systems, Pt wire was used as a counter electrode, Ag/AgCl was the reference electrode while the polished samples with various dimension holding with an Ir wire holder was used as the working electrode. The exposed area to the electrolyte of each sample was measured each time (scan rate was

20mV/s) for the current density calculation. .

The same three sets of electrode system and electrolyte were used for dealloying. Different dealloying potentials were selected with an attempt to approach the best np structure. Samples were weighted before and after dealloying to tracking the weight loss due to dealloying. The dealloying current approached to zero when the dealloying finished. Dealloying time varied due to the size of the sample. The samples were then rinsed and immersed with distilled water and ethanol to remove the residual H_2SO_4 .

3.4 Characterization

3.4.1 SEM and EDS

The microstructure of the thin film and bulk np sample was examined by using high resolution scanning electron microscopy (SEM). Three SEMs were used in this study: Hitachi S900 (Cold-cathode field emission filament), Hitachi S3200 (tungsten hairpin filament) and Hitachi S4300 (Cold-cathode field emission filament). SEMs were primarily worked under secondary electrons (SE) mode to observe the microstructure of the specimens. The Hitachi S900 has the highest resolution (up to 1nm) among the three SEMS. 3KV and 6KV acceleration voltages were used for S900. The samples for S900 were cut into small pieces and mounted on Cu holders with conductive carbon tape followed with carbon paint painted along the sample edges. SEM S3200 with Evex EDS system was used to analyze the composition of both Si and Pd samples under 20KV acceleration voltage. Usually, 90 seconds of collection time and three data points were used for each sample. SEM S4300 was also used to study the morphology of bulk

Pd sample under both SE mode and backscattering electrons (BSE) mode respectively. The samples for S3200 and S4300 were mounted on Al stubs with carbon tape and painted with carbon paint. To avoid the effects of coating layer on the fine np structure, Au nor other conductive layer were coated on all SEM samples in this research.

3.4.2 TEM and in-situ TEM

Transmission electron microscopy (TEM), one of the most powerful tools to directly observe microstructures of thin films materials, is a microscopy technique in which a beam of electrons transmits through an ultra-thin specimen, interacting with the specimen as it passes through. The TEM, scanning transmission electron microscopy (STEM) imaging and energy dispersive spectroscopy (EDS) were performed on a JEOL 2000FX. To make the TEM samples, the as deposited film with Si substrate (The Si wafer used for TEM specimen has a-SiO_x and a-SiN_x surface layer.) was cut into 3mm diameter plates by using an ultrasonic cutter. Then the cut piece was mounted to a quartz plug of a Gatan dimpler using crystal bond with film side down. Thickness of the sample was grounded down to ~75 nm thick by grounding Si wafer side with grinding paper. As ground TEM specimens were dimpled (Gatan Dimpler) the back side of the Si wafer substrate. After dimpling, the remaining Si and a-SiO_x was chemically etched with a solution of HNO₃: HF: acetic acid (2:1:1). The a-SiN_x layer acted as an etching stopper in the following etching step and allowed the deposited SiMg film to remain intact. Subsequently, dealloying was performed on etched TEM samples [64].

The in-situ nanoindentation of as-dealloyed np-Si on Si wedges was performed with a

Hysitron PicoindenterTM inside a JEOL 3010 TEM (operated at 300 kV) as shown in figure 3.3 (a). A cube corner diamond indenter with radius of curvature 100 nm was used. All indentations were performed under displacement control. The np-Si film for in-situ indentation was made by depositing SiMg film on 1000 μm thick H type Si wedge wafer (Figure 3.3(b)) followed by dealloying. In this research the deformation behavior of the as-dealloyed np thin films was observed in-situ.

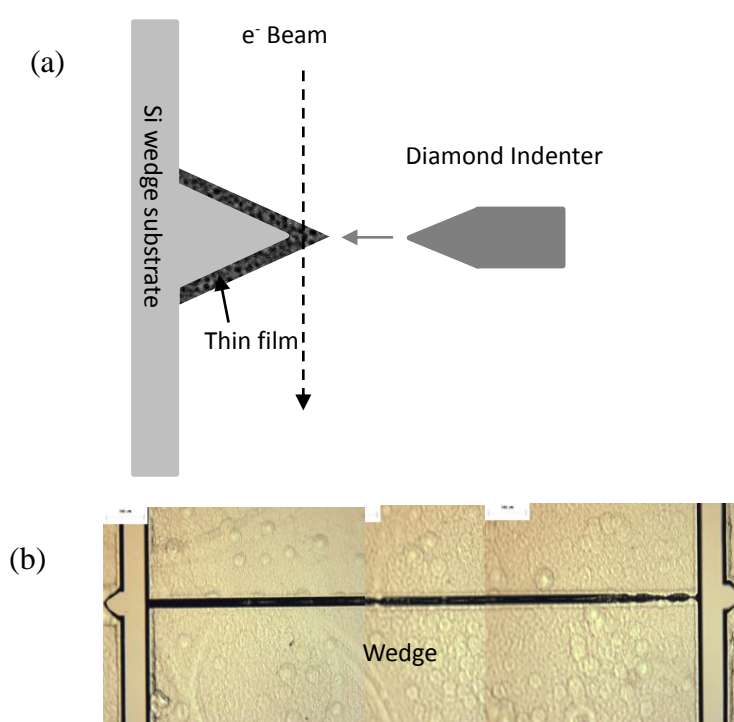


Figure 3.3 (a) Schematic of in-situ TEM indentation (b) Wedge Si wafer

The thin film stress evolution during dealloying and in-situ stress development during the absorption/desorption was measured with a wafer curvature system (FLX-2320-S, Toho Technology Co.). The laser source with 785nm wavelength was used to scan the film every 15° or 45° to distribute a 3D stress map that could indicate the stress situation

of the entire film. The film stress was calculated by the Stoney's equation:

$$\sigma_f = \frac{E_s}{(1-\nu_s)} \left(\frac{h_s^2}{6Rh_f} \right) \quad \text{Equation 3.1}$$

Where:

E_s is Young's modulus of the substrate, ν_s is Poisson's ratio of the substrate, h_s is substrate thickness, h_f is film thickness and R is radius of the curved substrate (thin film).

The thermal cycling was performed on the np-Si film with the wafer curvature system. Due to the difference of thermal expansion coefficients between the film and the substrate, when the thin film subjected to heating or cooling the film and substrate will be subjected to different degrees of expansion or contraction, as shown in Equation 3.2.

$$\frac{\Delta\sigma(T)}{\Delta T} = (\alpha_s - \alpha_f) \times M_f \quad \text{Equation 3.2}$$

Where:

α_s and α_f are thermal expansion coefficients for substrate and film respectively.

$\Delta\sigma_f(T)/\Delta T$ is the slope of the thermal elastic curve, M_f is film's biaxial modulus.

For the H_2 absorption/desorption experiments, ultra-pure nitrogen (99.999% purity) was used to purge the chamber for ~20 minutes before test. The absorption/desorption experiments with zero grade hydrogen (99.9% purity) and nitrogen were controlled by separate flow meters to make the H_2 - N_2 mixture at the desired H_2 concentration.

All the samples for the wafer curvature test were deposited on 3-inch diameter X180 μm

thickness Si wafer. For the samples with interlayer, the interlayer was also deposited on the back side of the wafer to balance the stress caused by interlayer.

3.4.3 XPS

X-ray photoelectron spectroscopy (XPS), a surface-sensitive quantitative spectroscopic technique, was used to measure the elemental composition at the parts per thousand range, empirical formula, chemical state and electronic state of the elements that exist within a material. With the ion beam etching technique of K-Alpha XPS (Thermo Scientific), depth-profiling composition of the SiMg and np-Si thin film has been studied. The XPS samples were deposited on Cu foil substrate with interlayers.

Chapter 4. Novel method for fabrication of nanoporous Silicon via dealloying in H₂O

4.1 Introduction

Porous silicon continues to attract scientific and technological attention for a number of potential applications [65]. It has been studied for possible use in sensing [66] and photonic devices [67], as a biomaterial for drug delivery [68], in new roles for the electronics industry, and in other diverse areas [69]. Porous Si is also a promising anode material for lithium ion batteries (LIBs), since this material would enable smaller electronic device sizes, higher specific capacity and lower irreversible capacities, features that have been actively pursued in recent years [70-73]. Over the last few decades, several methods have been developed to fabricate porous Si. In most cases, the porous silicon structure is formed by electrochemical anodization, typically with Si wafers etched in an electrolyte such as hydrofluoric acid (HF) [74]. There are also newer methods, e.g. ultrasonically enhanced anodic electrochemical etching and pulse current electrochemical etching [75, 76]. However, these methods involve the use of HF, yield a large pore size, or result in a rough material surface. The use of HF not only makes processing extremely dangerous, but is also environmentally unfriendly. Recently, Dai et al. [77] introduced a bottom-up synthesis method to fabricate porous Si with nanoscale crystallize size.

This paper describes a novel method for synthesizing high-purity (100% Si content)

nanoporous Si (np-Si) thin films, by dealloying Si-Mg precursor alloy thin films. The dealloying etchant used in this research study is pure water, which makes the process simple, non-hazardous and environmentally friendly. The waste product contains Mg ions in solution and is therefore also benign. Details of the synthesis, structural characterization and chemical analysis of dealloyed np-Si materials are presented here. This fabrication method holds promise for the production of substrate-supported np-Si that can be used as a LIB anode or in photovoltaic applications.

Dealloying is a common corrosion process during which an alloy is ‘parted’ by the selective dissolution of the most electrochemically active of its elements. This process results in the formation of a nanoporous sponge composed almost entirely of the more noble alloy constituents [59]. Dealloying of binary alloys in acidic solutions has been extensively applied to synthesize np films of various pure metals. Biener et al. [55] investigated the mechanical behavior of np-Au fabricated by dealloying Au-Ag precursor alloys with 75% HNO₃. Pugh et al. [60] obtained np-Pt by electrochemically dealloying Cu_{0.75}Pt_{0.25} precursor alloys with 1 M H₂SO₄. Wang et al. [61] fabricated several nanoporous metals such as Ni by dealloying precursors that contained Mg as the sacrificial element in various combination of distilled water and acetic acid. However, most dealloying etchants involve strong mineral acids and previous studies of np film synthesis via dealloying have primarily focused on alloys of noble and/or transition metals, such as the Au-Ag and Pd-Ni systems. This approach has not been applied to semiconductor material systems, e.g. to create Si with nanoscale porosity. In

order to utilize dealloying for this purpose, a suitable precursor with an optimized content of the sacrificial element, as well as a suitable dealloying etchant and procedure must be established.

To fabricate np-Si, the Si-Mg system was chosen in this study, since Mg offers several advantages as a sacrificial element. The phase diagram for the Si-Mg system indicates that SiMg_2 (CaF_2 structure, with Si atoms at the regular lattice positions of a face-centered cubic unit cell and Mg atoms occupying the tetrahedral sites) is the only equilibrium intermediate alloy expected to exist between the pure elements [62]. Mg was selected as the sacrificial element because (1) the SiMg_2 composition is close to the optimized composition for precursor systems such as Au-Ag for fabricating np-Au [78], and (2) Mg is an electrochemically active element that should be easily etched.

4.2 Experimental

The Si-Mg precursor film was deposited by magnetron co-sputtering from Si and Mg targets (both 99.99% purity) in a high-vacuum chamber (AJA ORION system) at room temperature. The sputtering system had a base pressure $\sim 10^{-8}$ torr and a working pressure of 2.5×10^{-3} torr (Ar gas). The substrate height was 55 mm above the confocal sputter guns, and substrate pre-cleaning was performed by biasing with RF power (35 W) for 1.5 minutes at an Ar pressure of 2.5×10^{-2} torr. The same deposition conditions were used for preparation of all samples. Various substrates, including (100)-oriented Si wafers with thickness 230 μm , as well as 50 μm Cu foil, were used in this study.

Different interlayers, including Ta, Cr, Au and Si, were deposited before the Si-Mg precursor film in order to improve the adhesion and stability of dealloyed np-Si films. To find the best dealloying etchant and synthesis approach, different dealloying procedures were evaluated and are discussed later in this chapter.

The microstructures of as-dealloyed np-Si thin films were characterized by high resolution scanning electron microscopy (SEM; Hitachi S-900), while the film composition was analyzed with x-ray energy-dispersive spectroscopy (EDS; Evex detector attached to Hitachi S-3200 SEM). Film thickness was measured with a Dektak 6M surface profilometer (Veeco, Inc). The evolution of film stress during dealloying was tracked by measurements in a wafer curvature system (FLX-2320-S, Toho Technology Co.). The crystal structure of the as-dealloyed samples was analyzed using a JEOL 2010F transmission electron microscope (TEM). Disks for making TEM samples were produced by ultrasonic coring, followed by dimpling the Si wafer side of the substrate/film disk. For TEM samples only, a Si wafer with amorphous SiO_x and SiN_x layers was used, with the SiN_x layer acting as an etch stop and also as a supporting membrane for the np-Si film. After dimpling, the remaining Si and a- SiO_x were removed by chemical etching with a solution of HNO_3 :HF:acetic acid (2:1:1).

4.3 Results and Discussion

4.3.1 Optimization of the SiMg precursor composition

To optimize the composition, the deposition rate of the Si and Mg was first determined.

For determining the deposition rate of Si, a glass substrate was marked with two straight lines with Sanford permanent Sharpie® before Si was directly deposited onto the glass substrate. The sputtering parameters for Si deposition rate measurement were as following: base pressure= 1.2×10^{-7} Torr; Sub height=55mm. Before the deposition, the substrate was cleaned with RF power 35 W for 1.5 minutes at pressure of 2.5×10^{-2} Torr. The deposition was held at pressure of 2.5×10^{-3} Torr for 20 minutes with RF power 100W. After deposition the glass substrate was immersed in Acetone for hours until the film on the marked lines removed completely. Then the thickness of the film was measured with Dektak 6 M surface profilometer (Veeco, Inc) by using standard scan. The parameters were selected as following: stylus radius $r=12.5\mu\text{m}$, scan length= $800\mu\text{m}$, duration=13 seconds and force=3 mg. These parameters were kept consistent in all thickness measurements in this study. 15 points were measured along the Sharpie® marked line to get thickness. By this way, the deposition rate of Mg was obtained. The deposition rate of Mg with DC power 100W was ~ 28.4 nm/min (~ 4.7 Å/s). The measured average Si thin film thickness was ~ 49 nm, giving rise to the deposition rate of Si with RF power 100W being ~ 2.5 nm/min (~ 0.4 Å/s). As the deposition rate is proportional to the power that applied on the target, the composition of the sample could be controlled by varying the deposition power.

Gradient samples with linearly varying Si-Mg content were prepared, to find the optimal Si-Mg film composition that would yield the np structure with smallest ligament size and stable ligament network after dealloying. To create the gradient

sample, Si and Mg sputtering targets were oriented in a confocal but diametrically opposed configuration, with a rectangular Cu foil substrate (size 7.5 cm \times 0.5 cm, coated with a 10 nm Cr interlayer) below and parallel to a line connecting the sputtering sources. One side was closer to the Si target and the opposite side was closer to the Mg target, and this arrangement was held stationary during film deposition. In this way, a 100 nm thick Si-Mg precursor film with composition gradient was created.

The rectangular gradient sample was cut into 15 pieces, each 5 mm long. All EDS composition measurements were conducted on the midline of the long axis of the initial gradient strip, in the middle of each 5 mm piece. As shown in Figure 4.1, the Si content along the gradient sample decreased linearly, from ~80 at.% on the Si-rich side to ~33 at.% on the Mg-rich side. The gradient sample was dealloyed with distilled water at elevated temperature for 24 hours. The two samples at the extreme ends of the gradient did not yield any porous structure after dealloying. The as-dealloyed microstructures of the five samples in the middle of the gradient, where Si content varied from ~63 at.% to ~50 at.%, are shown in Figure 4.2. The sample from this region with the highest Si content (~63 at.%) did not exhibit an open-cell np structure after dealloying (Figure 4.2a). Although it exhibited nanoscale pores at the surface, the limited amount of total porosity indicates there might be too much Si in the precursor, such that it could not be fully dealloyed. As the Si content gradually decreased, an increasing number of pores were created throughout the dealloyed films. However, as the Si content decreased to ~50 at.% (Figure 4.2e), the Si ligaments were unconnected, forming islands on the

substrate surface. The desired microstructure, consisting of a three-dimensional interconnected network of Si ligaments and open pores throughout a crack-free thin film, was observed in sample c (Figure 4.2c), which had an initial Si content ~57 at.%. This Si-Mg alloy composition was therefore considered to be the precursor film optimized for producing the best np-Si structure via dealloying.

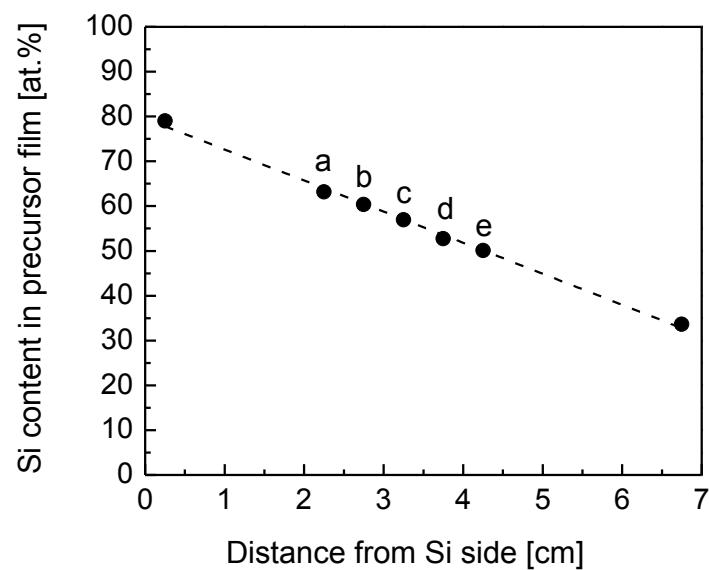


Figure 4.1 Variation of Si content along a Si-Mg compositional gradient sample. The locations marked (a)-(e) yielded porous structures during dealloying and were evaluated to identify the optimal precursor alloy for fabricating np-Si

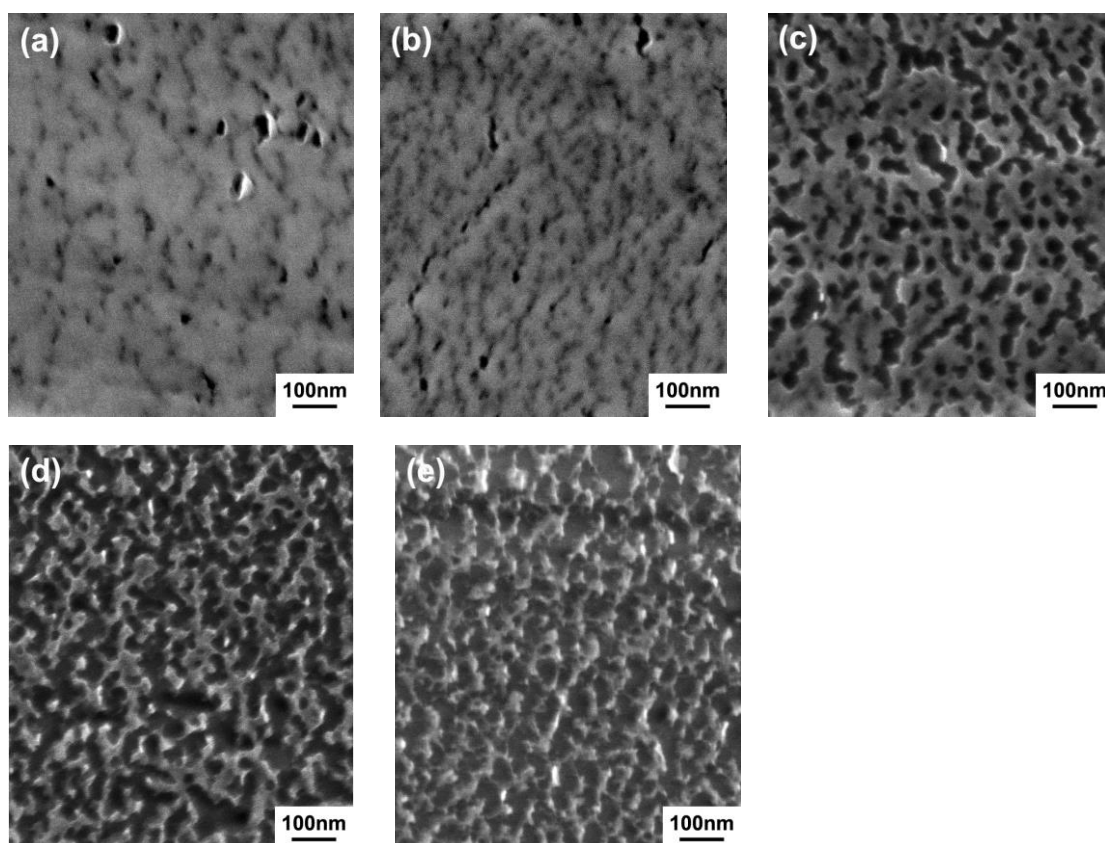


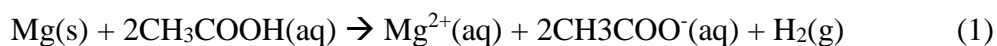
Figure 4.2 Microstructures of np-Si created from precursor films with different Si content. Micrographs (a)-(e) correspond to the compositions indicated in Figure 4.1.

The film in (c) exhibited the best microstructure in terms of open-cell porosity and interconnected ligaments

4.3.2 Optimization of the dealloying procedure, morphology and film stress evolution during dealloying

Different dealloying etchants, times and temperatures were evaluated in this study, to fabricate np-Si on various substrates. Ideally, the dealloying etchant should selectively and completely remove the sacrificial element (Mg) from the alloy and leave the more noble element (Si) in the np structure. Acetic acid (CH_3COOH) in different concentrations, such as 0.05%, 0.15%, 2% and 5% (on a volume basis, diluted

with distilled water), was initially used to fabricate np-Si film samples. This etchant had been found to remove Mg effectively in a previous study [79]. The reaction between Mg and acetic acid is:



This etchant yielded a porous Si film on Si wafer samples that had not been pre-coated with an interlayer, although the structure was not uniformly porous (some areas appear not to have been dealloyed) and the ligaments were coarse. The same dealloying method did not yield any porous Si on Cu foil samples, even Cu coated with an interlayer. In these cases, dealloying resulted in complete removal of the film. Similar results were obtained for Si wafer substrates that had been coated with various interlayers and dealloyed with acetic acid. These dealloying attempts yielded only bare substrates.

Subsequently, distilled water was found to be an effective dealloying etchant for Si-Mg precursor thin films. Surprisingly, this environmentally friendly etchant worked very well for a variety of substrate samples with different interlayers. Si-Mg films (with no interlayer) were dealloyed at different temperatures and over a range of times. The optimized dealloying procedure for producing np-Si from Si-Mg films involved distilled water at elevated temperature for 24 hours and yielded the desired np-Si structure, with a final composition of 100 at.% Si on all substrates which will be discussed later in this chapter.

The probable reaction between Mg and distilled water during dealloying is:



As the PH of the distilled water is around 6.5~7 the Mg is more likely to dissolved into Mg ions. Even if Mg were simply to be oxidized, the final reaction product of oxidized Mg should be Mg(OH)_2 , which has low solubility in water. Note that EDS measurements of film composition after dealloying in distilled water indicated that no Mg was present. Therefore, even though solid Mg(OH)_2 should form as a waste product during dealloying, it is removed from the np-Si structure.

A 100 nm Si-Mg sample with 10 nm Cr interlayer on Cu foil substrate was dealloyed in distilled water, to study the microstructural evolution of np-Si during dealloying. Figure 4.3 presents SEM micrographs after various times, where each micrograph corresponds to a different sample that was dealloyed in one step, for the time indicated. The microstructures in Figures 4.3f and 4.3g are similar, and further dealloying does not noticeably change the np-Si morphology. This is reasonable, given that all Mg has been removed after 24 hours. It is noted that the np-Si structure on the sample store in air for one year remained the same as the fresh dealloyed sample.

In addition to microstructural evolution, film stress and composition were tracked during dealloying. Figure 4.4 presents the biaxial film stress, as measured by wafer curvature, and the Si content, as measured by EDS, during the initial stages of dealloying when microstructural changes are most significant. After one minute of immersion in distilled water, the Si-Mg precursor film experienced an increase in Si content of almost 5%, and a limited number of incipient pores were observed with SEM

(see Figure 4.3a). Additionally, the initial compressive film stress (-113 MPa) changed to a tensile stress of 34 MPa. This large change in film stress (nearly 150 MPa) during the first minute of dealloying, despite the lack of obvious pore formation, indicates that the dealloying process starts immediately upon contact with distilled water and that the sample undergoes significant changes. After eight minutes of dealloying, Si content increased further to 65 at.%, and numerous small pores were seen at the film surface (see Figure 4.3b). After dealloying for a total of 12 minutes, the stress in the film peaked at nearly 300 MPa, approximately 400 MPa higher than the initial precursor film stress. Si content at this point had increased to 69 at.%, and the film exhibited numerous small pores.

Changes in stress during this initial dealloying stage are due to two factors: (1) removal of Mg atoms, which causes volume contraction and introduces a tensile stress, and (2) rearrangement of Si atoms during ligament formation and coarsening, which should reduce the film stress toward zero. These factors dominate the initial and latter stages of dealloying, respectively, as reflected in the stress-time plot in Figure 4.4. Dealloying begins with rapid loss of sacrificial Mg and causes film stress to move into the tensile regime. As Mg loss slows, film stress peaks (in this case, at 12 minutes). Further dealloying removes additional Mg, albeit at a much slower rate, and ligament coarsening reduces the film stress toward zero. In the case of dealloying np-Si, stress becomes compressive again, perhaps due to absorption of hydrogen produced during the dealloying reactions (reaction equation 2 and 3). This absorption-induced

compressive stress is believed to occur in np-Pd as well [80]. After 20 minutes of dealloying, the rate of Mg loss tapered and Si content appeared to stabilize, although complete removal of Mg would continue over a timespan of hours. Pores at the film surface were more prominent at 20 minutes, after most of the Mg removal had occurred (see Figure 4.3d), as compared to earlier dealloying times. As dealloying continued from 20 minutes to 160 minutes, Si content increased slightly from ~83 to ~87 at.% and film stress plateaued at -130 MPa, while the pores and ligaments coarsened (microstructure similar to that shown in Figure 4.3e). After dealloying for a total of 24 hours, the np-Si film exhibited interconnected ligaments with an average size of 25 nm (Figures 4.3g and 4.3h) and the Si content was 100 at.%. The film stress measured at 24 hours was -130 MPa, consistent with the plot in Figure 4.4.

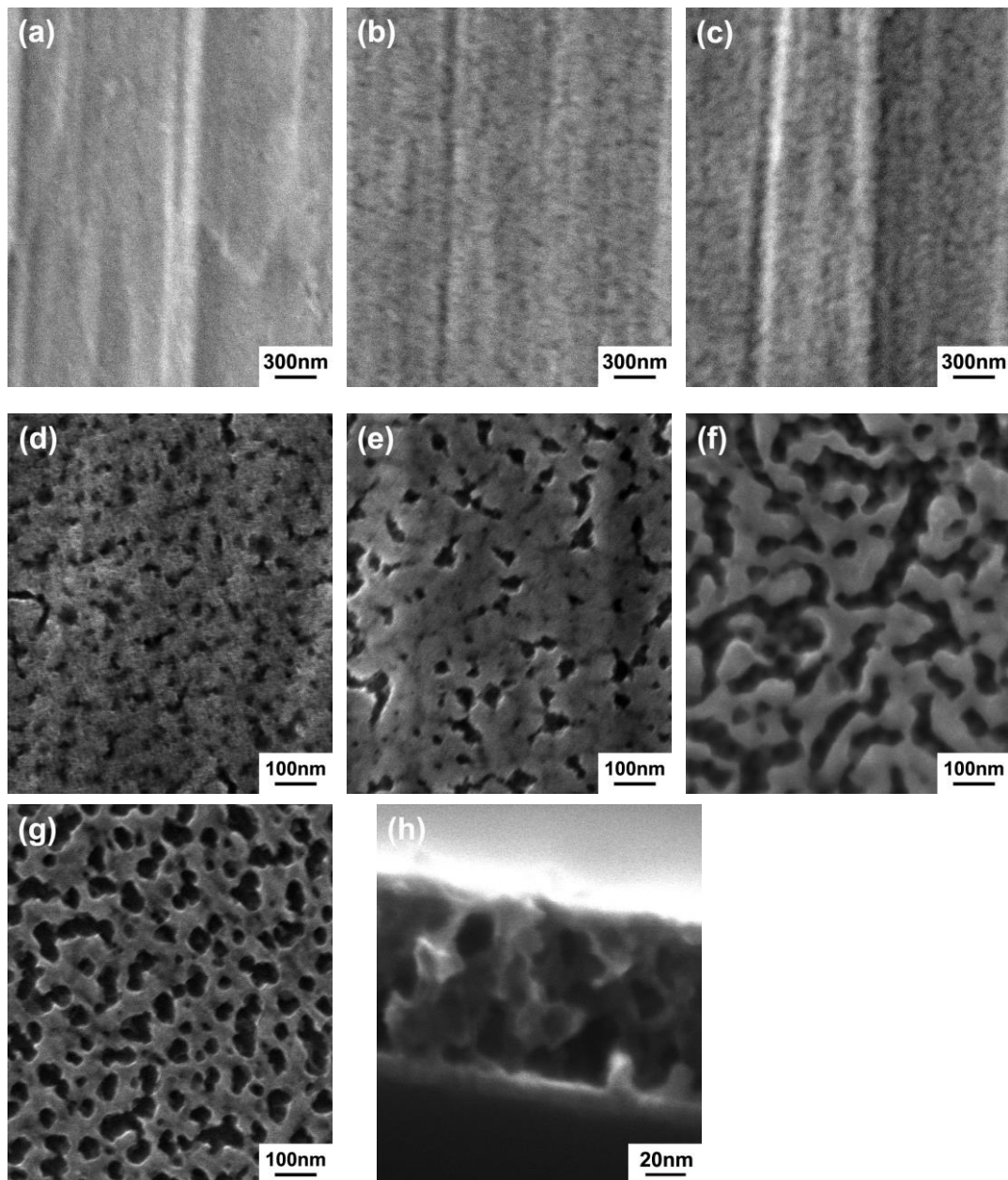


Figure 4.3 Microstructural evolution during dealloying, after (a) 1min, (b) 8 min, (c) 12 min, (d) 20 min, (e) 4 hours, (f) 18 hours, and (g),(h) 24 hours. Pores appeared quickly during dealloying, although it took much longer to establish a fully porous structure

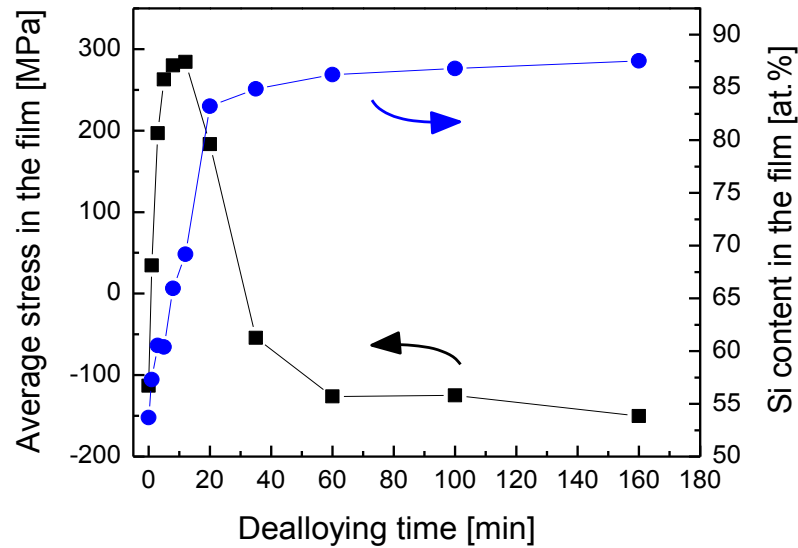


Figure 4.4 Film stress and Si content measured at different stages of dealloying. The sample was removed from solution, rinsed and dried in order to track the film stress. Composition was measured using witness samples that were dealloyed along with the larger wafer used for measuring stress

Different interlayers have been tried to optimize the np-Si structure and increase the adhesive of the film and the substrate. 100nm precursor Si-Mg film with different interlayers, such as 10nm Ta, Si, Au, Cr, Ni and 5nm Ta+5nm Si, have been tried. All these interlayer precursor films have the composition $\text{Si}_{53}\text{Mg}_{47}$ which is the optimized composition and with Cu foil substrate. All the deposition parameters were kept the same and all of the samples were dealloyed with distilled water for 24 hours. Figure 4.5 shows the morphology of the np-Si samples with different interlayers. All these samples distributed homogeneous porous structure with the ligament size around 25 nm. There are no macro and micro cracks. However, the np structure with different interlayers are

slightly different from each other in details. The np-Si film with Ta interlayer (Figure 4.5a) presents interconnecting cracking free structure. The open and uniform np-Si was observed all over the sample. The sample with 5 nm Ta and 5 nm Si interlayer also present nice np-Si structure. The 10nm Si interlayer sample display more open, continuously, network liked np-Si among these different interlayer samples. The 10nm Cr interlayer sample is one of the best np-Si structures that had been obtained in this research. It displayed very small pore size (less than 20nm) and uniformly ligaments across the whole sample. The np-Si also presented on the Au interlayer sample. The pore size of Au interlayer as-dealloyed sample is around 20 nm. The EDS study had been applied the as-deposited and as-dealloyed samples. For the as deposited Au interlayer sample, Table 4.1 shows the composition is about $\text{Si}_{52}\text{Mg}_{48}$. Table 4.2 and Figure 4.6 shows the EDS result and spectrum of the as-dealloyed Au interlayer sample. After dealloying, there is no Mg left in the film, which indicate that the film is pure crack-free np Si thin film.

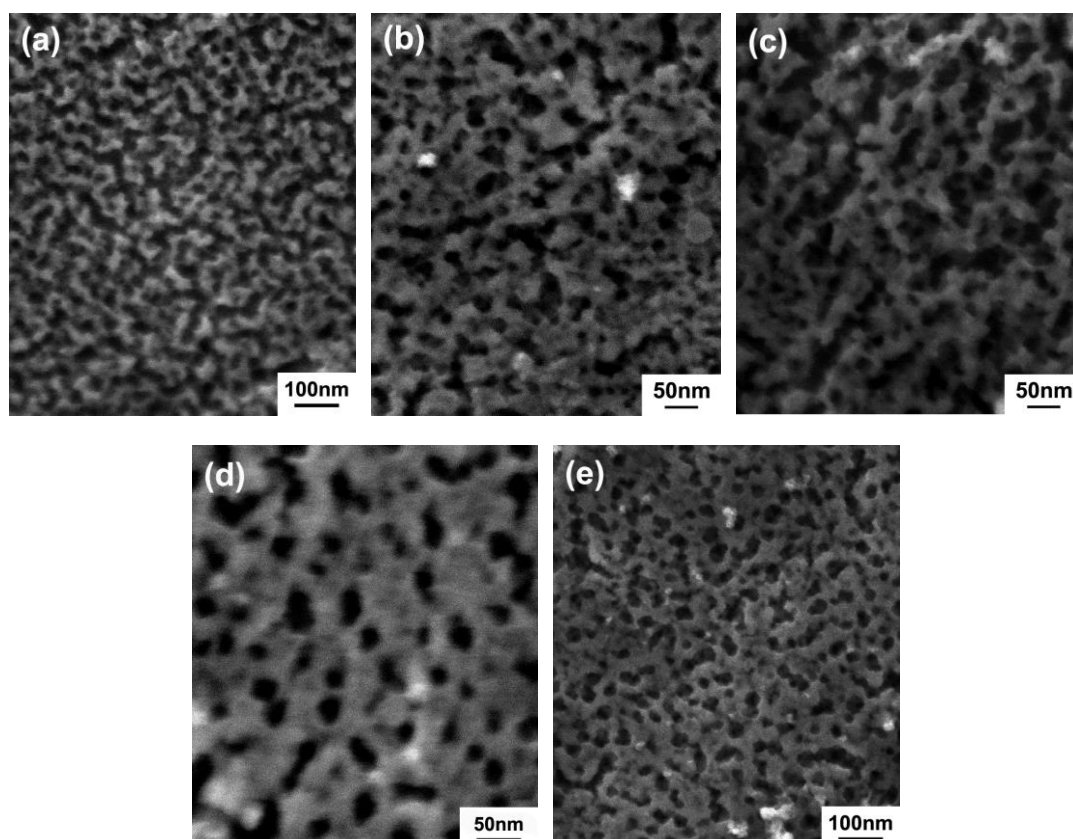


Figure 4.5 Morphologies of np-Si films with different interlayers. (a) Ta interlayer; (b) Ta and Si interlayers; (c) Si interlayer; (d) Cr interlayer; (e) Au interlayer. In all cases, a stable open-cell structure was achieved, although the average ligament size and structural details of the np network varied with interlayer material

Chemical composition ratio of as-deposited Au interlayer sample

Table 4.1 Chemical composition ratio of as-deposited Au interlayer sample

Elements	Point 1		Point 2		Point 3		Average	
	WT%	AT%	WT%	AT%	WT%	AT%	WT%	AT%
Mg	42.85	46.41	44.17	47.75	45.90	49.50	44.31	47.89
Si	57.15	53.59	55.83	52.25	54.10	50.50	55.69	52.11

Table 4.2 Chemical composition ratio of as-dealloyed Au interlayer sample

Elements:	WT%	AT%	K_A	K_F	K_Z	Intensity	P/bkg
MgK	0	0	0.858	1.044	1.001	0	0
SiK	100	100	1	1	1	7.925	1.1

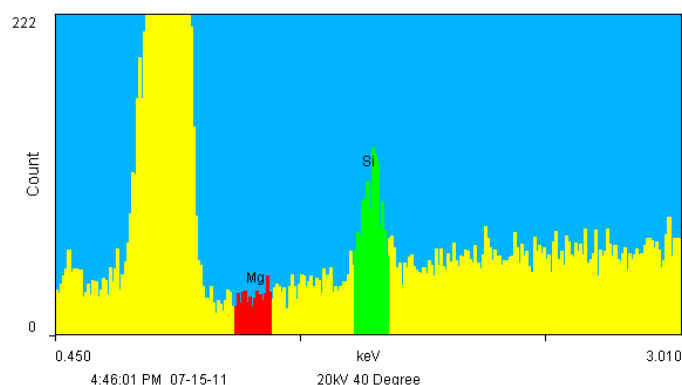


Figure 4.6 EDS spectrum of the as-dealloyed Au interlayer sample

4.3.3 Amorphous np-Si and crystallized np-Si

After obtaining the np-Si film, vacuum annealing at various temperatures had been carried out to control the crystal structure and the ligaments size of the as fabricated film which may change mechanical behavior and cycling performance of the np-Si to prepare for future study. Among trials, annealing the as-dealloyed np-Si samples at 400°C in vacuum for an hour resulted in the crystal structure change and ligaments coarsening of the as dealloyed film. As demonstrated in Figure 4.6, (a) is the morphology as-dealloyed in distilled water for 24 hours on Si wafer substrate, (b) is the morphology of the as-dealloyed sample after annealed at 400°C for 1 hour. It is evident that the np structure of the Si thin film remained after annealing and the ligaments of the np-Si grew bigger after annealing.

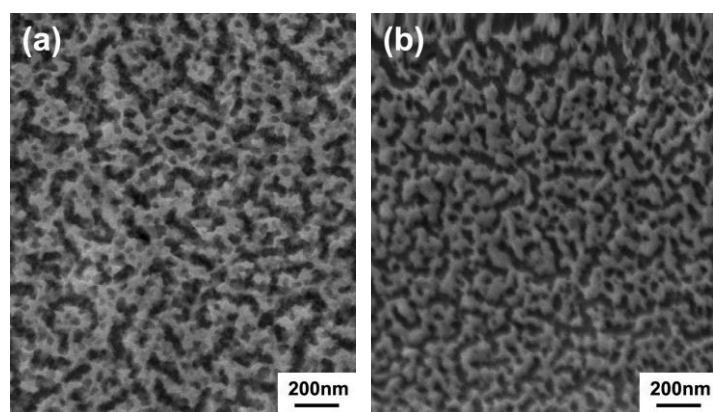


Figure 4.7 Morphology of 200 nm np-Si film with Au interlayer (a) in the as-dealloyed condition and (b) after vacuum annealing at 400 °C for 1 hour. The ligament structure is coarser after annealing, but is still nanoporous

TEM was used here to study the details and crystal structure of the np-Si thin film. TEM specimens were made by cutting, dimpling, etching and dealloying. As shown in Figure 4.8 is the TEM observation of the np-Si film before and after annealing. As shown in Figure 4.8a, the ligament size of the np-Si film is around 20-25 nm. The selected area electron diffraction (SAED) pattern (Figure 4.7b) shows diffuse scattering, suggesting that the as-dealloyed np-Si is amorphous which is also supported by the HRTEM results (Figure 4.78c). The porous structure of the as annealed sample was shown in Figure 4.8d, twinning was observed in the film as indicated by the red circle. The SAED pattern no longer shows diffuse scattering as appeared on the as-dealloyed sample before, but the polycrystalline diffraction rings. Together with the HRTEM pattern (Figure 4.8f), it is confirmed that the as-dealloyed amorphous np-Si transferred into crystalline np-Si film after annealing at 400 °C for 1 hour in the vacuum chamber. This result verified that it is possible to fabricate nc-np-Si by annealing at moderate

temperature. The TEM-EDS result showing no Mg peak in the as-dealloyed and annealed np-Si film which confirms that the obtained film is a 100% pure np-Si thin film.

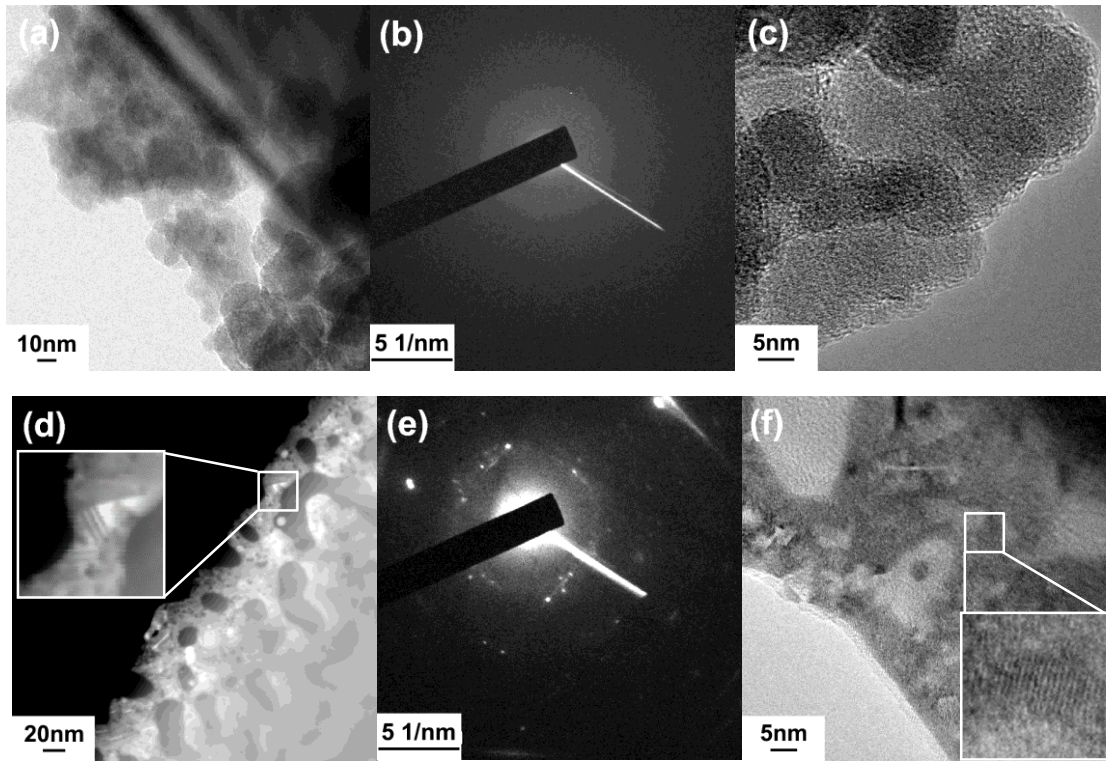


Figure 4.8 Micrographs (a)-(c) show TEM results for as-dealloyed np-Si: (a) BF image, (b) selected area diffraction pattern from the np-Si film, (c) high resolution image. The absence of diffraction spots in (b) and lack of lattice fringes in (c) indicate that as-dealloyed np-Si is amorphous. Micrographs (d)-(f) show TEM results for np-Si that was annealed at 400 °C in vacuum for 1 hour: (d) dark-field STEM image, (e) selected area diffraction pattern, (f) high resolution image. Images (d) and (f) indicate that the annealed np-Si is at least partially crystalline

It may be that amorphous np-Si contains hydrogen and is actually hydrogenated a:Si-H. This would agree with earlier statement that hydrogen incorporation into Si causes

compressive stress in the np-Si film. H would likely be incorporated during dealloying of the Si-Mg precursor and formation of np-Si ligaments, allowing the ligaments to be amorphous rather than H being incorporated after formation of pure Si ligaments. Finish by stating that this is a novel form of nanostructured Si that may exhibit good properties for applications.

4.3.4 XPS study of the np-Si film

TEM EDS line scan was conducted on the as dealloyed sample. As shown in Figure 4.9 The Si peaks shows when scan on Si ligaments. The Mg peak has very low counts during the whole scan, which indicates the film has low residual Mg after dealloying. Also, the low counts of O peak reveal the ligaments was pure Si instead of SiO₂.

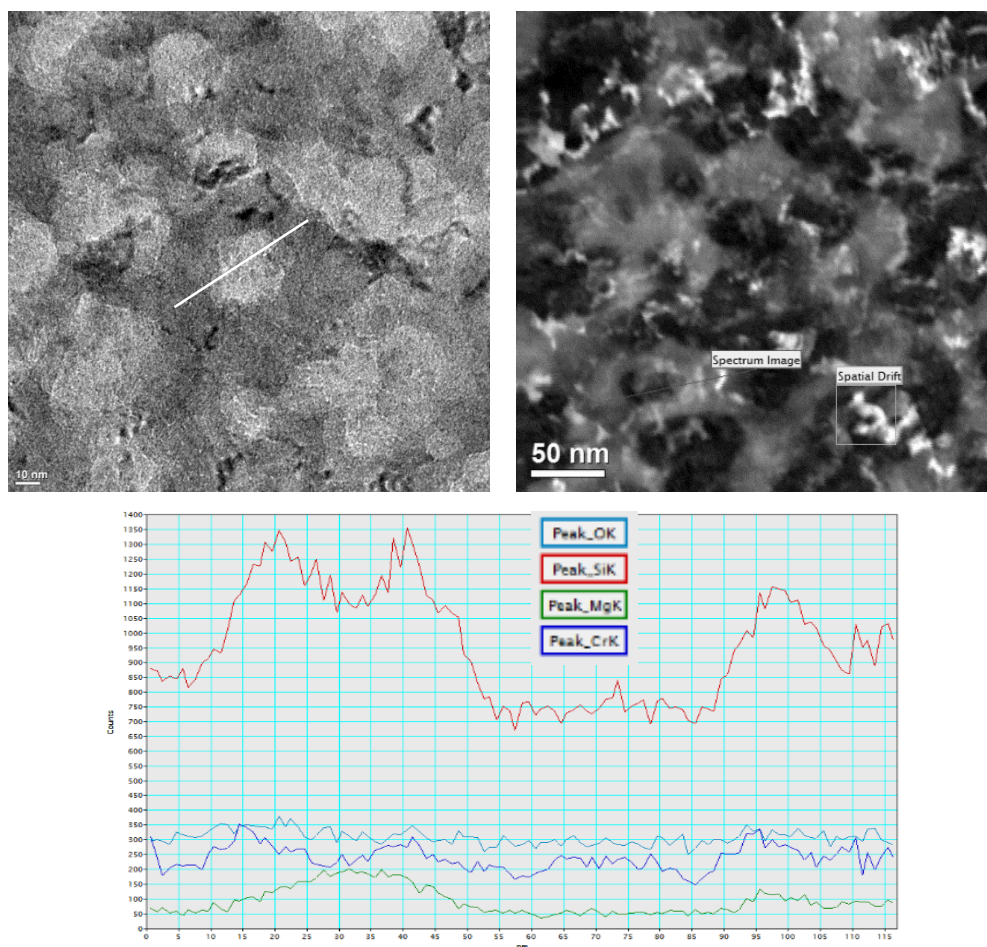


Figure 4.9 TEM EDS line scan result

XPS was used to study the film composition distribution along the film. With the ion beam etching technique of K-Alpha XPS (Thermo Scientific), depth-profiling composition of the as deposited SiMg film and as dealloyed np-Si thin film has been studied. The XPS was carried on the 100nm on fresh as-deposited (within 24hrs after deposition) SiMg film with 10nm Cr interlayer on Cu foil substrate sample as shown in Figure 4.10. The sample was etched for 35 depth levels with 30 seconds for each etching level. The XPS results (Figure 4.10 (a)) show the overall composition composes: 67.84 at.% Si and 32.16 at.% Mg from the XPS result. The same film chemical composition was also tested with EDS, showing 53.59 at.% Si and 46.41 at.% Mg (Table 4.3). It is

commonly known that EDS results are usually for qualitative analysis only, while XPS is more quantitatively accurate thus offers more credentials. From the depth profile, near surface area was observed to have more Mg content, which might be attribute to Mg shutter was the last one to be closed when finishing deposition. Also, the Si composition bumps near the substrate is due to the Si shutter was open previous to the Mg shutter during the deposition. After about 21 etching levels, the Cr signal appears which indicated the scan approached the interlayer level and the SiMg film has been penetrate. Figure 4.10 (b) indicates the low content oxygen is associate with the Mg content through the as deposited film. More Mg presents about 10nm deep below the surface and oxidation happened near the surface. Throughout the film, no trace of SiO₂ was observed. The Si2p scan on the as deposited film is shown in Figure 4.11. There is no silica peak appear in the as deposited film, however, in the as dealloyed film, the SiO₂ peak did present.

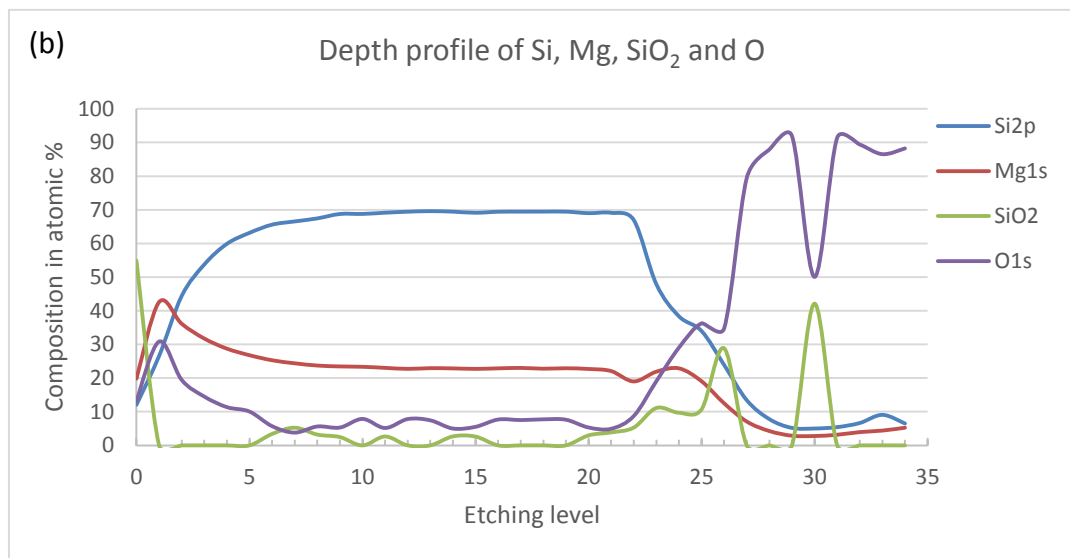
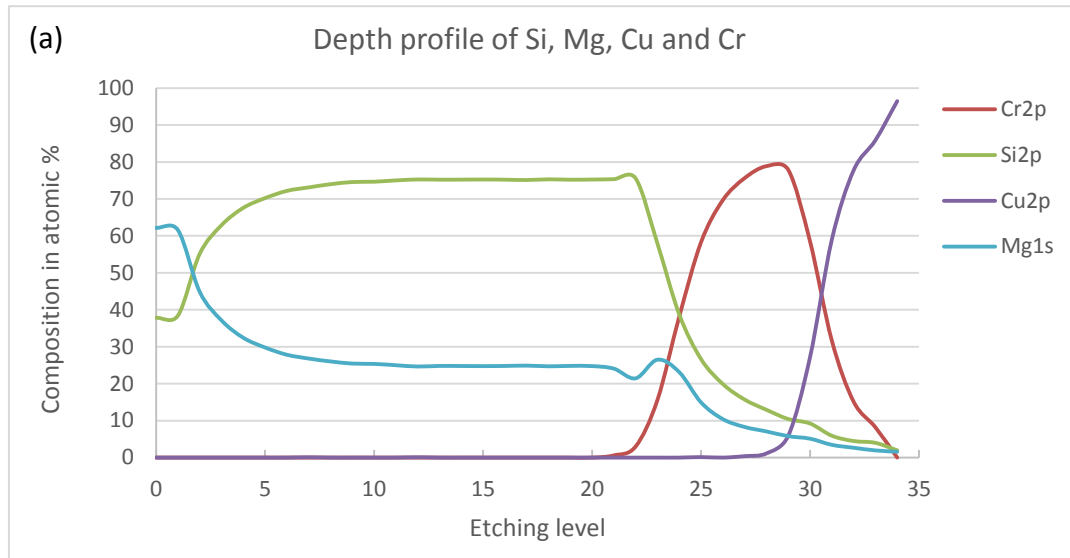


Figure 4.10 Depth profile scan of 100 nm as deposited SiMg film

Table 4.3 EDS result of the 100nm as deposited SiMg film

Elements:	WT%	AT%	K_A	K_F	K_Z	Intensity	P/bkg
MgK	42.84	46.41	0.914	1.011	1.001	13.566	5.3
SiK	57.16	53.59	0.622	1	1	13.977	2.6

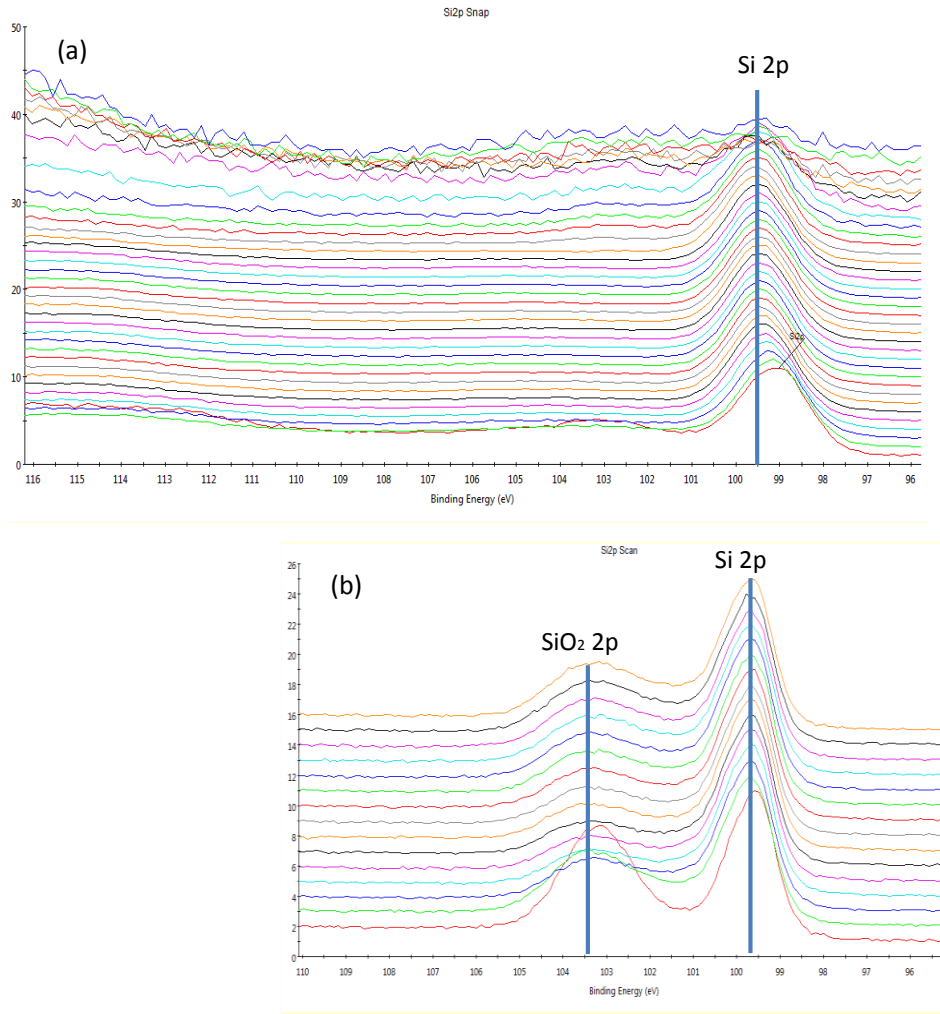


Figure 4.11 The Si2p peak in the (a) as deposited film and (b) as dealloyed film

4.3.5 Thermal cycle stress study of the np-Si film

Two thermal cycles were applied on the np-Si film dealloyed from 100nm precursor SiMg alloy thin film on 3 inch SiN_x coated Si wafer. The thermal cycling stress evolution is shown in Figure 4.12. During the first heating cycle which started at room temperature then heated up to 200 °C, the stress in the np-film increased ~170MPa and the stress stayed quite stable during the followed cooling process from 200 °C to room temperature. The stress increased by another ~180MPa during the second heating up cycle from room temperature to 300 °C, while stress did not appear notable change

during the followed cooling process from 300 °C to room temperature. The stress stay stable during the cooling cycles up to 300 °C indicating that the np-Si film is pure Si but not SiO₂, as the np-Si film has the same thermal expansion coefficient with the Si wafer and the SiO₂ has a significant difference thermal expansion coefficient ($0.55 \times 10^{-6} \text{ }^{\circ}\text{C}^{-1}$) from Si ($2.6 \times 10^{-6} \text{ }^{\circ}\text{C}^{-1}$).

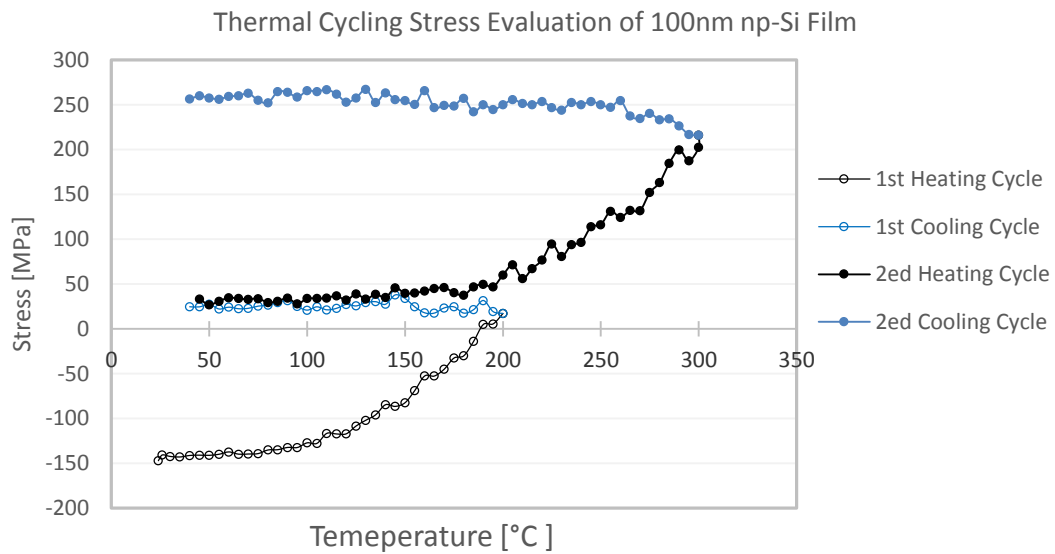


Figure 4.12 Thermal cycling stress evaluation of 100nm precursor np-Si thin film

4.3.6 Approaching micro-meter thick np-Si film

Thicker SiMg film was pursued in order to investigate the mechanical properties of np-Si, the 300nm precursor SiMg film has been achieved by tripling the deposition time of 100 nm film. The film was dealloyed in H₂O for 24 hours, the morphology of the as dealloyed film are shown in Figure 4.13. The plan view of the film still showing uniformly distributed Si ligaments with the size around 30~50 nm, which are similar to the np structure dealloyed from 100 nm precursor film. The cross section image (Figure

4.12 (c)) shows the as dealloyed film thickness is about 157nm which indicated the 300 nm precursor SiMg film has about 50% thickness contraction during dealloying.

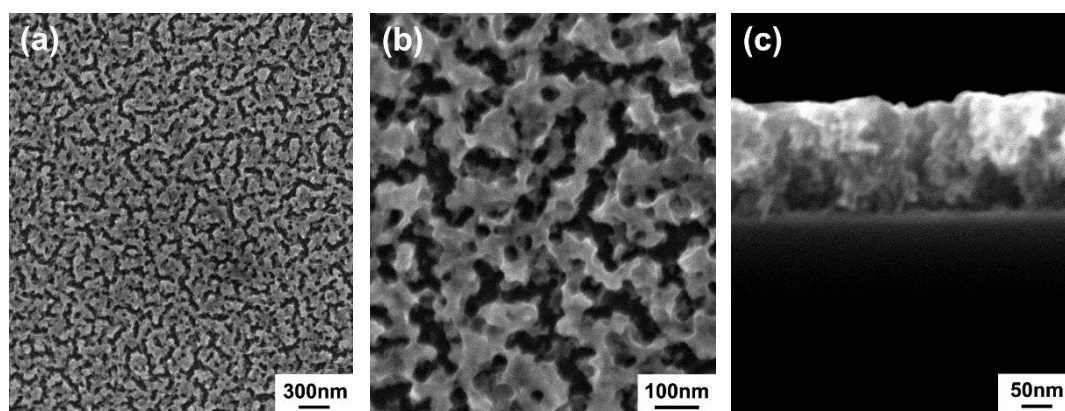


Figure 4.13 Morphology of as dealloyed 300nm precursor film (a) and (b) plane view morphology, (c) cross section view

SiMg alloy precursor film with 600 nm thickness has been deposited by extend the deposition time (Figure 4.14 (a)). However, after dealloying in H₂O for 24 hours the film peel off from the substrate as shown in Figure 4.14 (b). Various dealloying procedure has been applied to the 600nm film to pursue the np structure as shown in table 4.4. However, all the films result in delamination or none np structure. The 600nm film was then deposited onto 3 inch Si wafer to study the stress distribution in the film. 10nm Cr layer was deposited on both side to balance the stress caused by interlayer. The stress distribution inside the films was mapping by wafer curvature and shown in Figure 4.15. The average stress in 600 nm as deposited film was 373.09 MPa, compare that with 100 nm as deposited film, the average stress is 113.09 MPa. The initial stress in the film effect the dissolution of the Mg and diffusion of the Si during the dealloying process. The increasing stress in the thicker film is considered as the reason of the film

delamination during dealloying.

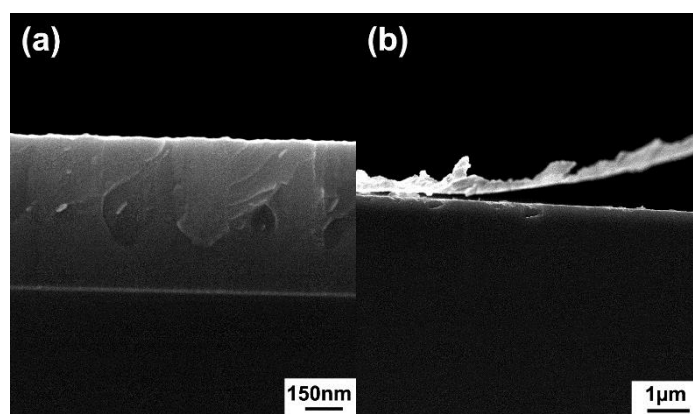


Figure 4.14 cross section images of (a) as deposited 600 nm film
(b) as dealloyed film

Table 4.4 Various dealloying precurdure that has been applied on to 600nm SiMg films

Sample No.	etchant	Concentration vol %	Dealloying temperature °C	Dealloying time
1	H ₂ O	-	-6	28 hours
2	H ₂ O	-	Room temperature	6 hours
3	H ₂ O	-	Room temperature	20 hours
4	H ₂ O	-	Room temperature	50 hours
5	HAC	0.5%	Room temperature	20 mins
6	HAC	2.5%	Room temperature	1 mins
7	HAC	2.5%	Room temperature	2 mins
8	HAC	2.5%	Room temperature	20 mins

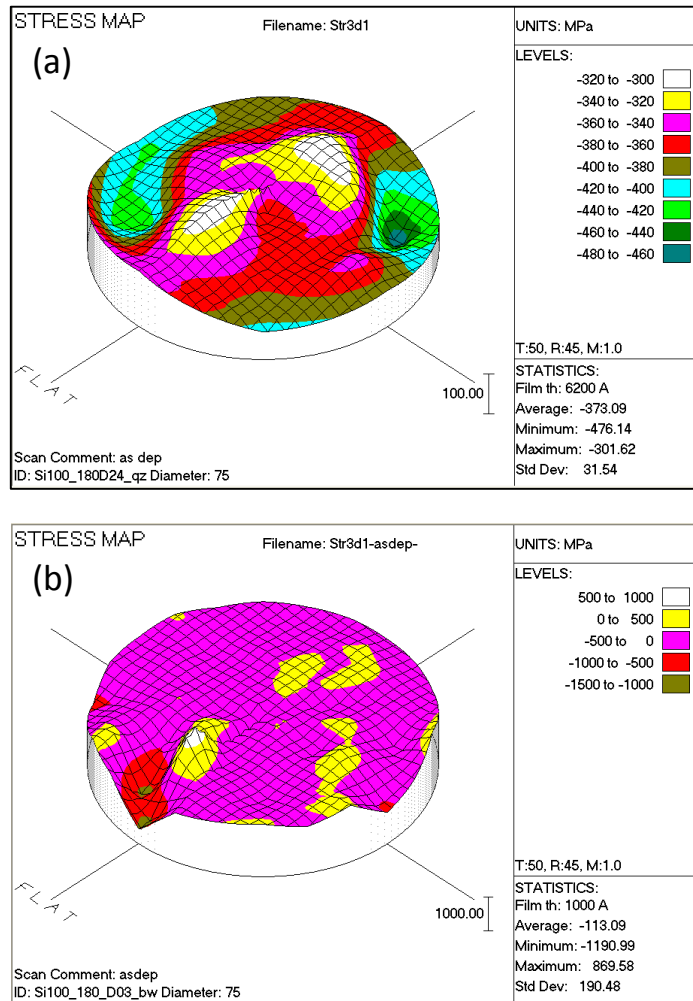


Figure 4.15 Stress mapping of the as-deposited SiMg films (a) 500 nm as-deposited film (b) 100nm as-deposited film

4.4 Summary

In summary, it is possible to fabricate np-Si by dealloying the deposited Si-Mg precursor thin film with the optimized composition as established in this research. The best composition of SiMg precursor alloy is not SiMg₂ as expected but around Si₅₃Mg₄₇. The composition is not extremely strict, the np structure presented with the Si at.% varies from 52%-57%. The appropriate dealloying method with pure water has been

found to yield the as-dealloyed film that presents an open np structure with the ligament size ~25 nm. TEM observation verified the microstructure of the as-dealloyed np-Si thin film is pure amorphous Si film and the amorphous film could be crystallized by annealing in vacuum at certain temperature. Further research work needs to be conducted in the future. The as fabricated np-Si thin film will be served as an anode in LIB and tested with electrochemical battery testing. The difference between the properties of amorphous and nanocrystalline np-Si, the mechanical behavior of the np-Si thin film will also be studied in the future.

Chapter 5. Nanoporous Si thin film negative electrode lithium ion battery

Silicon, because of its high capacity to store lithium, is increasingly becoming an attractive candidate as an anode material for lithium ion batteries (LIB). One significant problem with using Si for the anode is the large strain that accompanies charge-discharge cycling, due to swelling of the Si during Li insertion and deinsertion. Np-Si offers a large amount of free volume for Li absorption, which allows the anode material to swell without cracking. In this chapter we demonstrate the cycling performance of coin-cell battery samples with np-Si thin film that prepared via dealloying and also discuss the suitability of np-Si as a LIB anode material.

5.1. Introduction

Among the various Li alloy elements, group IV elements such as Si and Sn have been the main focus as LIB negative electrode materials owing to their high capacity. Si as the second most abundant element on earth has been considered as a promising negative electrode because of its extremely high theoretical capacity for Li ions compared with currently used carbon or graphite. The Si itself can alloy with Li up to $\text{Li}_{4.4}\text{Si}$, corresponding to 4212 mAh/g [15], which is more than ten times that of existing graphite anodes and various other oxide and nitride materials. However, an intermetallic alloy electrodes like Si suffers large volume changes and may go through

multiple crystallographic phase transition during lithiation and delithiation [16], which result in up to 200%–300% volume change during the cycling expansion/contraction insertion. The compressive and tensile stresses, respectively upon lithiation and delithiation, causes mechanical cracking and pulverization of the Si anode and leading to loss of electrical contact and eventual fading of capacity, which typically results in extremely limited cycle life [18].

Properly structured materials could avoid the problems caused by Si swelling. As the nano-scaled materials has been suggested to be a possibility for next generation LIB since their physical, electrical and chemical properties are very different from those of their bulk materials [28], novel nanostructured silicon have been explored for this purpose. Si nanostructures like Si nano-composites, nanowires, nanotubes and np-Si have received wide interest because of their good cycling performance as negative electrode materials since the nanostructures Si provides sufficient room to accommodate Si volume change and allows for facile strain relaxation without mechanical fracture during charge/discharge cycle. Many researchers have studied the nanosized materials used for battery negative electrode. For example, Zhenda Lu, et al. [81] designed a nonfilling carbon-coated porous silicon micro particle that presented $\sim 1500 \text{mAhg}^{-1}$ specific capacity for over 1000 cycles with C/4 cycle rate. Yan Yao et al. [82] reported a novel interconnected Si hollow nanosphere electrode that achieved the discharge capacity of 2725mAhg^{-1} for 700 cycles. Zhiyu Jiang et al. [83] developed a method to prepare porous Si powder by acid etching Al-Si alloy powder. The porous

silicon powder had a spongy structure with size about 15 μm , it contains silicon nanobars of with diameter about 50 nm which exhibited about 1497 mAhg^{-1} at 69th battery cycle.

Although silicon anodes have great advantages over conventional graphite anodes in LIBs, there are still significant challenges need to be overcome before silicon anodes can be utilized in practical Li batteries. Motivated by this, a new type of structured Si anode which could overcome the disadvantages and present long cycle life without fading and cracking issues is needed in the future portable device development. The previously structured Si anode either have none uniform macro/micro structure or large pore size ($\sim\mu\text{m}$). In this chapter we investigated the performance of the lithium ion battery (LIB) with the np-Si thin film that fabricated from dealloying SiMg alloy. The uniformly distributed ligaments and pores provided sufficient room for the anode to swelling during the battery cycling. This method is promising to produce the Si negative electrode in LIB in the future.

5.2. Experimental

The np-Si thin film was fabricated by deposition followed with dealloying [84]. Mg was selected as the sacrificial elements. The SiMg precursor film was deposited by magnetron co-sputtering from Si and Mg targets (both 99.99% purity) in a high-vacuum chamber (AJA ORION system) at room temperature. The sputtering system had a base pressure $\sim 10^{-8}$ torr and a working pressure of 2.5×10^{-3} torr (Ar gas). The substrate height was 55 mm above the confocal sputter guns, and substrate pre-cleaning was

performed by biasing with RF power (35 W) for 1.5 minutes at an Ar pressure of 2.5×10^{-2} torr. The same deposition conditions were used for preparation of all samples. 50 μm Cu foil and Kapton were used as substrate and as the current collector in the coil cell. 10 nm Cr or Au interlayer was introduced to improve the adhesion and stability between the films and the substrates. For Kapton substrate sample, 100 nm Cu layer was deposited on both side to provide the conductivity of Kapton for working as the current collector. 100 nm and 200 nm precursor SiMg alloy film has been deposited with the composition Mg ~47% (at. %) and Si~ 53% (at. %) which has been proved as the optimized alloy composition in previous work [84]. Dealloying was followed with deposition to conduct np-Si structure. The distilled water which is totally environmental friendly was used as etchant. The as-deposited samples were immersed in distilled water at elevated temperature for 24 hours for dealloying. The dealloying etchant and dealloying procedure has been optimized in previous study [84].

CR2025 coin-type half cells (Hohsen) with the as fabricated np-Si anode was assembled for battery test in this research. Pure Li metal (99.9%, Sigma Aldrich) foils was used as the counter electrodes. The electrolyte used in the research was 1 M LiPF_6 in ethylene carbonate/dimethyl carbonate (EC/DMC, 50/50 by volume, Novolyte). A computer controlled multi-channel potentiostat (VMP3, Bio-Logic) was used to conduct the electrochemistry measurements. These coin cells were cycled at room temperature with various C-rates by galvanostatically cycling to evaluate the electrochemical and cycling performance. The high and low potential cut-offs for cycling the Si thin film electrodes

were set to 2.0 and 0.01 V relative to pure Li, respectively. In this work, discharging refers to Li going into Si (lithiation of Si), and charging refers to Li coming out of Si (delithiation of Si) [26].

The microstructures of as-dealloyed np-Si thin films were characterized by high resolution scanning electron microscopy (SEM; Hitachi S-900), while the film composition was analyzed with x-ray energy-dispersive spectroscopy (EDS; Evex detector attached to Hitachi S-3200 SEM).

5.3. Results and discussion

100 nm Si-Mg film was deposited on the Cu foil substrate (10 nm Cr interlayer) with the composition $\text{Si}_{53}\text{Mg}_{47}$. Figure 5.1(a) and 5.1(b) show the SEM morphology of the sample dealloyed with distilled water for 24 hours. The as dealloyed sample distributed homogeneous porous structure with the uniformly ligament size around 20nm. The cross section image (Figure 5.1(c) and 5.1(d)) show that the thickness of the as-deposited sample is about 102 nm, and after dealloying, the thickness of the sample is about 65nm, which indicates the film thickness shrink about 30% during the dealloying due to the loss of the Mg and the re-distributed of the Si atoms.

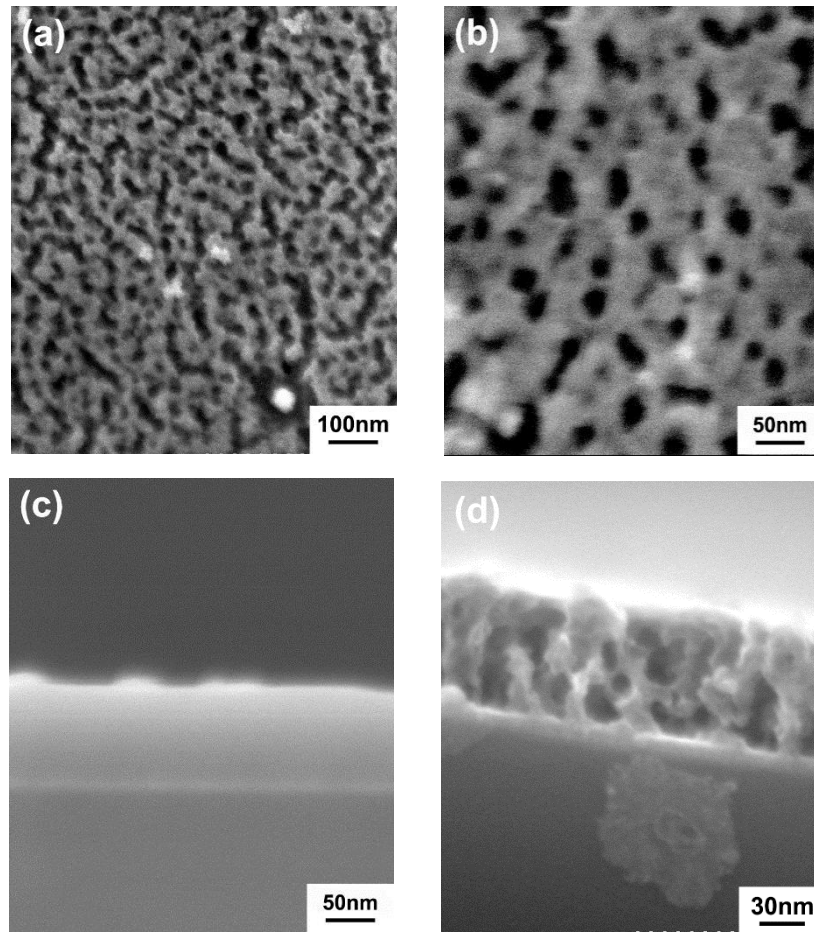


Figure 5.1 (a) and (b) are SEM morphology of the sample Cr interlayer sample dealloyed with distilled water for 24 hours under different magnification; (c) and (d) are the as-deposited and as-dealloyed sample cross section, respectively

Battery tests have been applied on Cr interlayer np-Si samples. The as-dealloyed np-Si film sample that had ~20nm pore size was used as the collector acting as anode in a coin type half-cell. Some Si has lost during dealloy which was indicated by the film thickness shrinking and was detected by ICP in the research. However, the exact amount Si on the electrode has not been found out at this point, so the Si that has been sputtered on the substrate was taken as the mass that involved in the battery cycling. More experiments are needed to perform to measure the effective mass on the electrode.

As plotted in Figure 5.2, the np-Si anode was cycled with C/5 rate for 30 cycles. The GCPL cycling result shows that the np-Si anode has impressive specific capacity up to 1100 mAh/g and cycling stability up to 30 electrochemical cycling. The surface morphology of the np-Si anode sample after cycling with C/5 rate for 30 cycles is showing in Figure 5.3. From the SEM images, it is noted that the np structure of the np-Si electrode still remains similar to its structure before cycling, which indicates that the fine-sized and uniform porous structure of the np-Si anode provided the sufficient room for Si to swell during the lithiation and delithiation. It is also impressed that, as shown in Figure 5.3a, the surface of the np-Si with Cr interlayer electrode is still very smooth and no macro crack presents on the surface. Compared the cycled electrode morphology with other researchers' results in which pure Si thin film was cycled [26], it is believed that the porous structure played a critical role to minimize the crack possibility during the cycling. And the as-dealloyed 100% pure np-Si is promising for the anode materials of LIB.

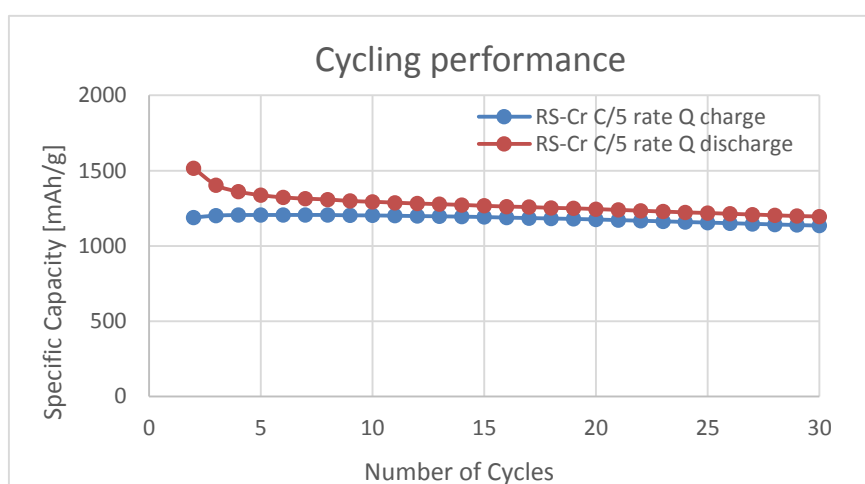


Figure 5.2 Cycling performance of 100nm np-Si with 10nm Cr interlayer anode sample cycled with C/5 rate

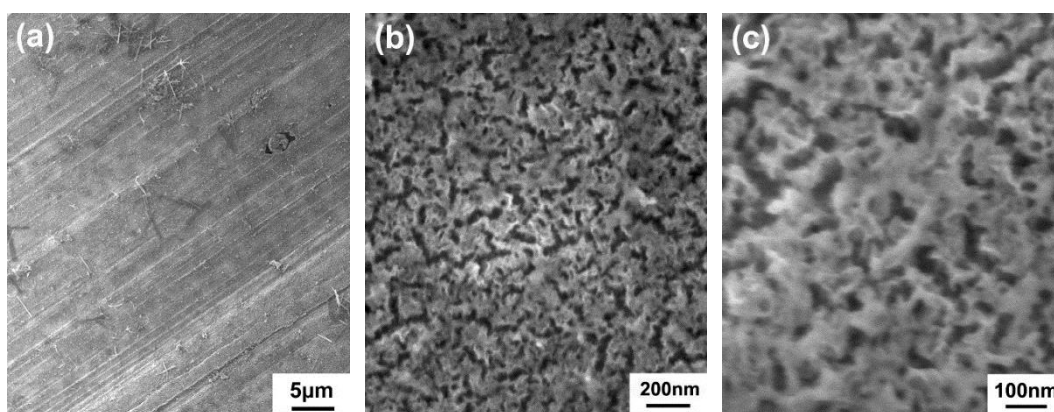


Figure 5.3 Morphology of the np-Si (10nm Cr interlayer) electrode after 30 cycles under different magnification

100 nm and 200 nm precursor Si-Mg films with 10nm Au interlayer np-Si samples have also been fabricated to act as the anode for LIB half cells to identify the thickness effect on the battery performance. As shown in Figure 5.4 the 200 nm precursor-Au interlayer sample cycled with C/5 rate has the lowest specific capacity. Under the same cycle rate C/5, 100nm np-Si electrodes had a capacity which almost doubled the 200 nm electrode in the beginning. However, after ~15 cycles, the capacity started to decrease. And the capacity of 100nm precursor electrode became close to the 200 nm one when it reached 30 cycles. Though the 200 nm electrode had a lower starting specific capacity, it showed more stable cycling performance during the 50 cycles. When the 100 nm precursor film np-Si electrode cycled with C/5 and C/10 rates, the specific capacity were starting at the same level and all slowly decreasing towards the same ending capacity level. The sample cycled at C/10 rate showed the largest capacity drop after 50 cycles. After 50 cycles, the 200 nm sample cycled with C/5 rate had similar capacity as the 100nm precursor sample that cycled with C/10 rate. Comparing this results with the Cr

interlayer sample's cycling performance, the Cr interlayer sample did not have the highest specific capacity in the beginning; however, it had the most stable specific capacity. Its capacity demonstrated almost no change after 30 cycles.

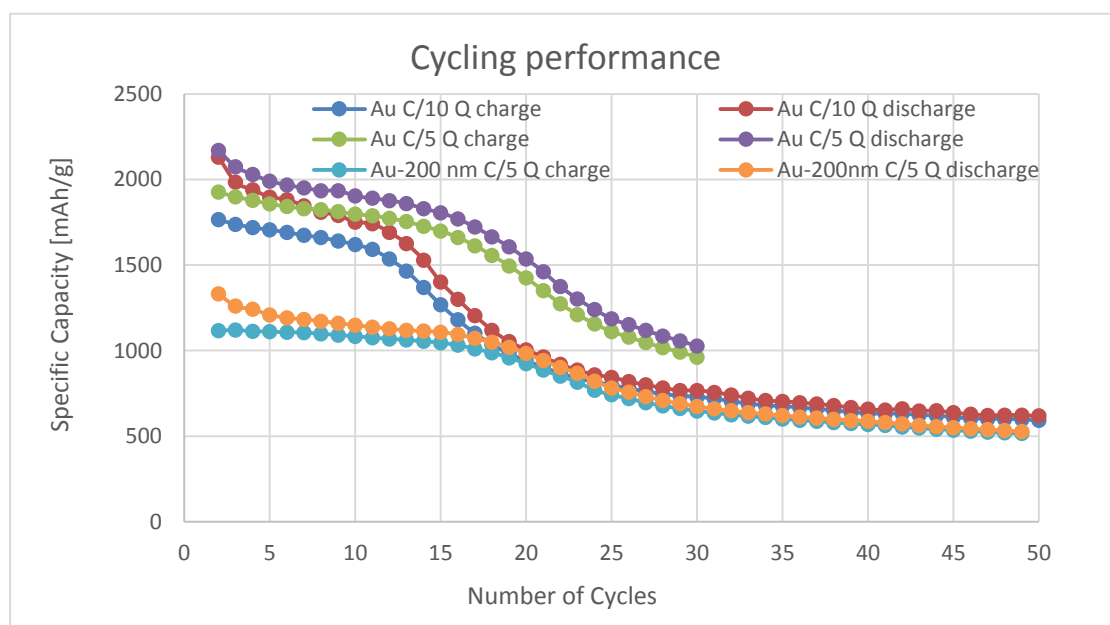


Figure 5.4 Cycling performance of RS-Au anode sample cycled with C/5 and C/10 rate

Figure 5.5 shows the morphology of the Au interlayer sample before and after cycling.

The morphology of the 100nm precursor and 200nm precursor samples that dealloyed by the same method are slightly different. 200nm precursor film shows more hierarchical feature (Figure 5.5a and 5.5b). The macro crack on the 100nm precursor film anode as shown in Figure 5.5b was believed to be due to the roughness of the Cu foil substrate. The stress during dealloying caused the cracks happened along the machining scratch of the Cu foil substrate [85]. Figure 5.5c shows the morphology of the RS-Au-100 nm sample that was cycled with C/5 rate for 30 cycles. It is clear that the np structure of the electrode was deformed after 30 cycles. This failure may be due

to the macro defects of the as-dealloyed np-Si film. The reason of why the electrode sample Cr and Au interlayer sample with similar starting morphology end up with totally different structure after cycled after 30 cycles is unclear for now. The coulombic efficiency of Cr and Au (100 and 200nm) interlayer coin cell cycled with different cycled rate are showing in Figure 5.6. All coulombic efficiency are close to 98% after 30 cycles. More research focus on the effect of the structure on the cycling performance will be done in the further research.

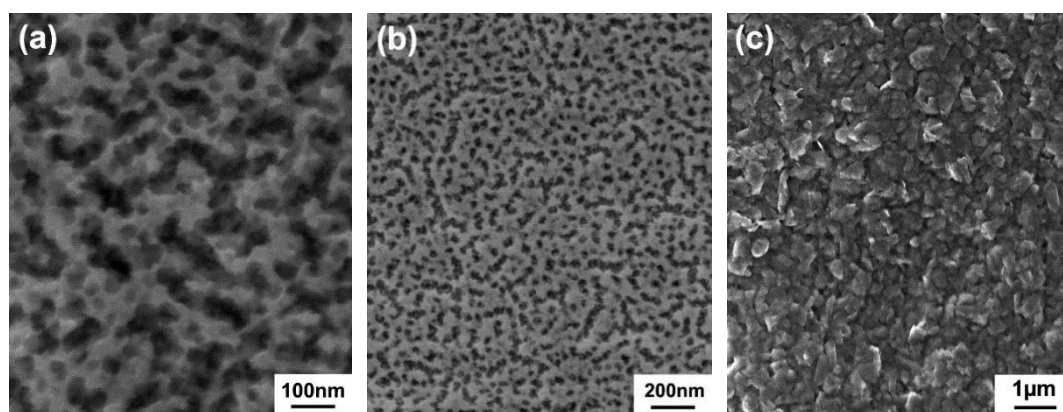


Figure 5.5 Plane view of the np-Si (10nm Au interlayer) electrode (a) 200nm precursor film after dealloying before cycling (b) 100nm precursor film after dealloying before cycling, (c) the morphology of as-dealloyed 100nm precursor film anode after 30 cycles

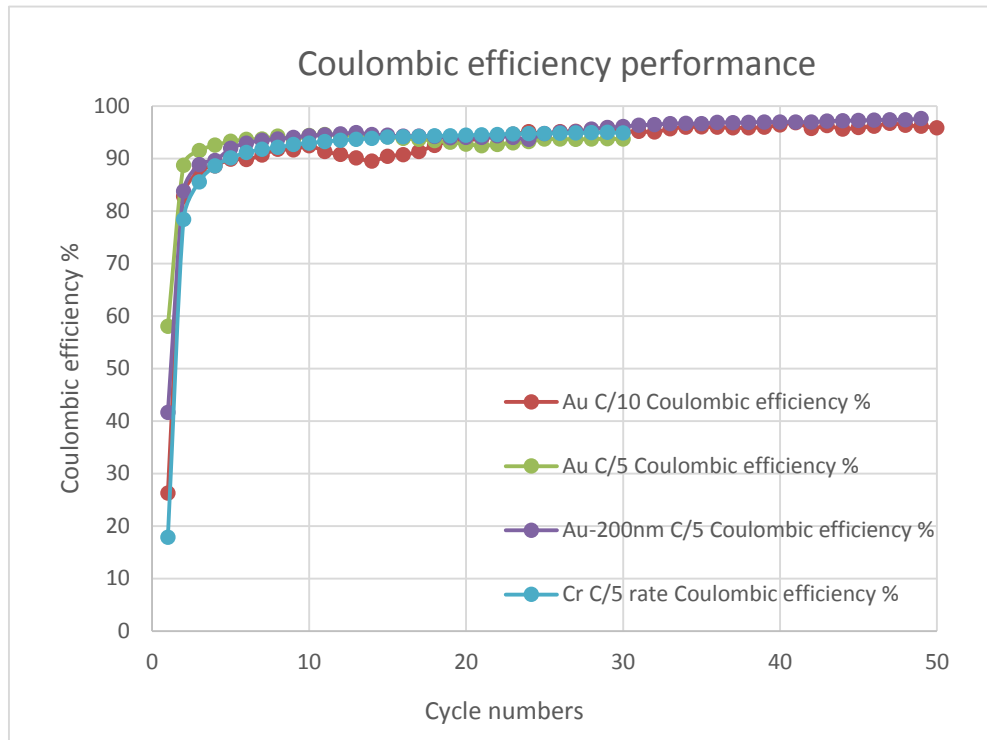


Figure 5.6 The coulumbic efficiency of Cr and Au (100 and 200nm) interlayer coin cell cycled with different cycled rate

Kapton, a polyimide film with high mechanical and thermal stability, was also tried as the substrate of the electrode in this research. 100nm thick Cu was first deposited on both sides of the Kapton substrates as the current collectors, then 10nm Au was deposited as the interlayer. As shown in Figure 5.7, the morphology of as-dealloyed sample with Kapton substrate under different magnification shows that the np structure on the Kapton substrate is more continuous and uniform than the structure on Cu foil substrate. And contributed by the smooth surface of Kapton, there was no macro cracks on the as-dealloyed samples. The battery cycling performance of the np-Si on Kapton substrate was also carried out by GCPL measurement with different C-rate. The results are shown in Figure 5.8. Although the Kapton substrate sample has the best as-

dealloyed np-Si structure, the cycling performance of both C/5 and C/10 rate testing showed very low specific capacity, which was only around 100-200 mAh/g. It indicate that the binding force between the np-Si film, interlayer and substrate is one of the critical aspects for LIB.

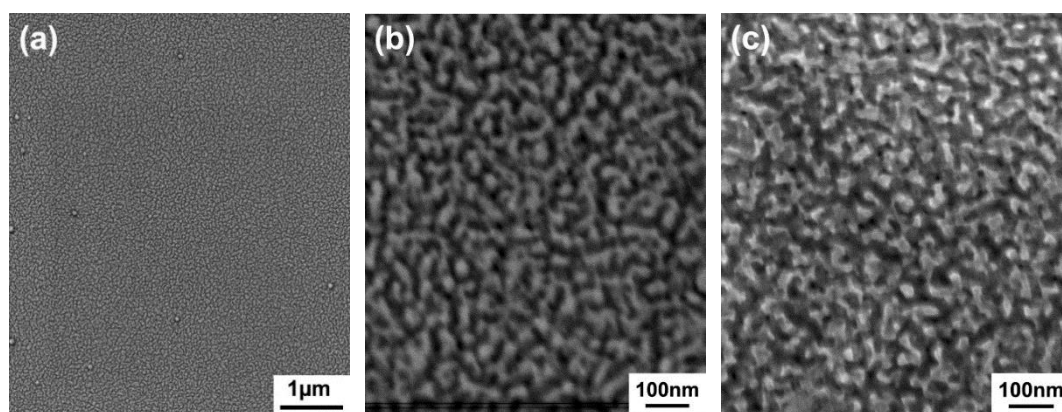


Figure 5.7 Plane view of the Kapton substrate np-Si electrode (a) and (b) are the morphology before cycling under different magnification (c) is the morphology after cycling

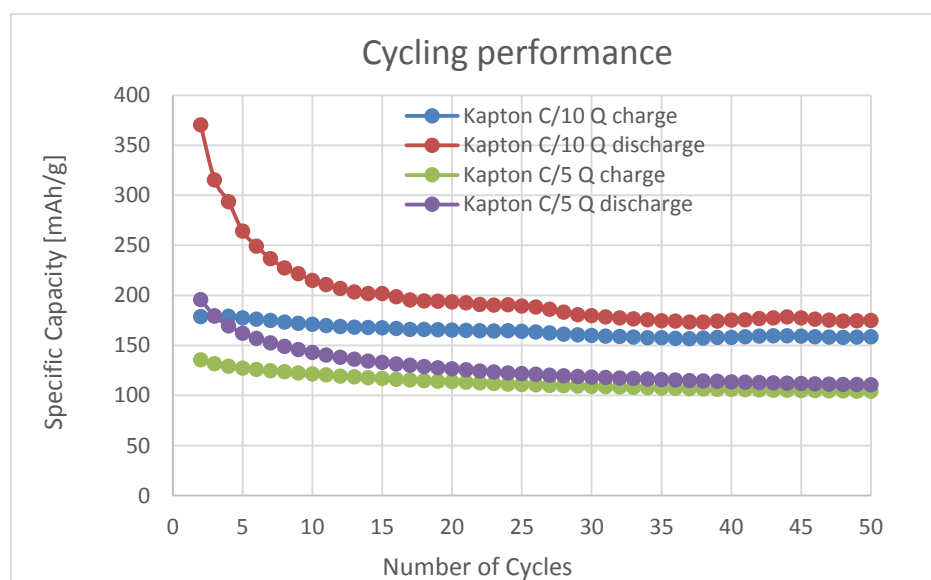


Figure 5.8 Cycling performance of np-Si with Kapton substrate anode sample cycled with C/5 and C/10 rate

5.4. Summary

In summary, the optimized composition $\text{Si}_{53}\text{Mg}_{47}$ precursor thin film yielded an open np structure with the ligament size of 20~25nm when dealloying with distilled water which is totally environment friendly. The as-dealloyed np-Si thin film that has been tested as an anode in LIB with electrochemical battery testing in which the specific capacity of the as fabricated LIB has achieved ~2000mAh/g. Different interlayer sample has an noticeable effect on the behave of the cycling performance. Also, the film thickness play a role on the capacity of the as tested LIB.

More work still needs to be conducted in the future. The effective mass of np-Si on the electrode, which is important for the battery cycling current and specific capacity, is subjected to be exactly measured or calculated. The macro cracking issue due to the Cu foil substrate machining defect needs to be solved. The deformation behavior of the np-Si thin film will be studied by in-situ TEM. The np-Si thin film which could allow the relaxation of the strain and stress during the volume expansion/ contraction with the lithiation/ delithiation for LIB will be further developed in the following research.

Chapter 6. Mechanical behavior of nanoporous Silicon

Nanoporous silicon (np-Si) is an attractive potential anode material for lithium ion batteries (LIBs) as it offers a large amount of free volume for lithium insertion and de-insertion, allowing the anode to swell and contract without cracking during lithium cycling. Understanding the mechanical behavior of np-Si is challenging, as the nanoscale ligaments (20 nm wide) induce size effects and can change the fundamental deformation mechanism(s) in Si at this length scale. High-purity (100% Si content) np-Si thin film was fabricated by dealloying precursor SiMg alloy film and the mechanical behavior was measured for these specimens. In-situ nanoindentation in the TEM, performed on as-dealloyed thin film np-Si, revealed that this material can withstand extensive deformation without exhibiting brittle fracture.

6.1 Introduction

Many research works have been carried out to pursue better understanding of the np materials mechanical behavior in the past decade. A basic conclusion for np materials is that when the materials grain size approaches 5-10 nm, the nanophase materials may deform in a different way from its bulk materials [52]. Nanoporous materials exhibit mechanical properties different from their dense/bulk counterparts therefore offer an opportunity to study size effects on mechanical behavior. Fredrik O stlund, et al. [86] discovered size effect in compression tests on Si pillars with sub-micrometer, where the small Si pillars show ductility comparable to that of metals. The critical diameter of Si

pillar is between 310 and 400 nm. Over the size range of 1 μm down to 200 nm the Si columns transitioned from predominantly brittle to ductile behavior at room temperature.

The recent development of in-situ TEM mechanical testing allows the observation of the nanoporous materials' dynamical mechanical behavior. Especially, the combination of TEM and in-situ TEM nanoindentation technique provides a unique possibility to study the deformation of the materials when they are indented [56]. With this technique, the nucleation and motion of dislocations can be observed while a load-displacement curve is simultaneously recorded, allowing direct correlation of measured mechanical behavior with microstructural changes. Many of the studies have been conducted with the aid of nanoindentation technique. A J Lockwood et al. [87] study the dynamical mechanical deformation properties of 50nm Si nanoparticle clusters by in-situ TEM nanoindentation. The Si nanoparticles loaded with displacement controlled load fractured along the weak interface between two nanoparticles.

The development of lithium-ion batteries requires a novel anode material that can replace the currently used anode material, carbon, which has relatively low energy storage ability. Si which has the lower electrical discharge potential and higher charge capacity provides the possibility of serving as the anode material in LIB. However, Si, as the anode material suffers the large strain that accompanies charge-discharge cycling, due to swelling of the Si during lithium (Li) insertion and deinsertion. Properly structured materials could avoid the problems caused by Si swelling. Np-Si which could

provide sufficient room during battery cycling has drawn lots of attention [Xu Jiang Np-Si for LIB]. The recent interests in nanoscale materials have led to advances in the understanding of these promising materials. However, the mechanical properties of np-Si still lacks understanding and little attention has been given brittle nanoporous materials fabricated by dealloying, e.g. np-Si. The study of the mechanical behavior of np-Si in this research offers an opportunity to study size effects on mechanical behavior Si which can help to understand the performance of np-Si anode in LIB.

6.2 Experimental

The np-Si thin film was fabricate by deposition followed with dealloying [84], during which Mg was selected as the sacrificial elements. The Si-Mg precursor film was deposited by magnetron co-sputtering from Si and Mg targets (both 99.99% purity) in a high-vacuum chamber (AJA ORION system) at room temperature. The sputtering system had a base pressure $\sim 10^{-8}$ torr and a working pressure of 2.5×10^{-3} torr (Ar gas). The substrate height was 55 mm above the confocal sputter guns, and substrate pre-cleaning was performed by biasing with RF power (35 W) for 1.5 minutes at an Ar pressure of 2.5×10^{-2} torr. The same deposition conditions were applied for preparation of all samples.

Dealloying process was followed with deposition to conduct the np-Si while distilled water was used as etchant which was totally environmental friendly. The as-deposited samples were immersed in distilled water 24 hours for dealloying. The dealloying etchant and dealloying procedure have been optimized in previous study [84].

TEM is one of the most powerful tools to directly observe microstructures of most thin films and bulk materials. In this research, the crystal structure and dimension of the as-dealloyed samples was analyzed using a JEOL 2010F transmission electron microscope (TEM). Disks for making TEM samples were produced by ultrasonic coring, followed by dimpling the Si wafer side of the substrate/film disk. For TEM samples only, a Si wafer with amorphous SiO_x and SiN_x layers was used, with the SiN_x layer acting as an etch stop and also as a supporting membrane for the np-Si film. After dimpling, the remaining Si and a- SiO_x were removed by chemical etching with a solution of HNO_3 :HF:acetic acid (2:1:1) [64].

The in-situ TEM indentation study was analyzed inside a JEOL 3010 TEM operated at 300 kV (National Center for Electron Microscopy, Lawrence Berkeley National Laboratory, Berkeley, CA). In-situ nanoindentation of dealloyed np-Au on Si wedges was performed with a Hysitron PicoindenterTM, in which a cube corner indenter with radius of curvature 100 nm was used. All indentations were performed under displacement control. The np-Si film was made by deposited SiMg film on 1000 μm thick H type Si wedge wafer followed with dealloying.

6.3 Results and Discussion

The in-situ nano-indentation in TEM was designed to test how much strain the thin film can accommodate, thus a series of strain levels were set in the test, i.e. in the ranges of <10%, 20%-30% and 60-70%. The 'strain' in this chapter is represented the film's thickness change during indentation compared to its original thickness. It is necessary

to note that the strain through the deformed sample area was not homogeneous because the different ligaments were subjected to different amount of deformation, and also different types of deformation. The strain referred in this chapter is not an actual strain because the ligaments subjected to different amount of deformation, and also different types of deformation (most of the ligament were bent rather than compressed under indenter).

A very small indent depth $\sim 9\text{nm}$ resulting a max load $\sim 4\mu\text{N}$ was first applied. The load and displacement curve with a strain range $\sim 9\%$ is shown in Figure 6.1. The curve appears like elastic deformation range within 10% strain as no elastic-plastic transition point nor slope change in the loading curve. The relationship of load and displacement can be fit in a linear relationship during the loading process. Figure 6.2 shows the TEM images captured from in-situ indentation video on load displacement curve with strain range $<10\%$. Figure 6.2 (a) shows the np-Si film before the indenter approached the film, (b) is the moment of the max indent depth being $\sim 9\text{nm}$ and (c) is after the indenter was removed from the film. The film thickness did not have any change before and after indentation, which testify that the film is under elastic deformation with $\sim 10\%$ strain. Also from Figure 6.2, it was noticed that some materials presented at the indenter tip prior the indentation. According to Eric A. Stach et al. [88] the debris clings on the indenter after a deep indentation may result from a build-up of static charge on the diamond caused by exposure to the electron beam.

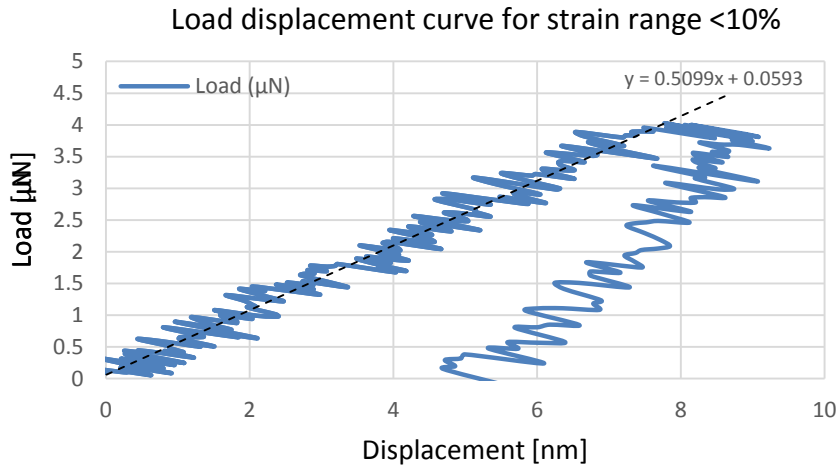


Figure 6.1 Load displacement curve with strain range <10%

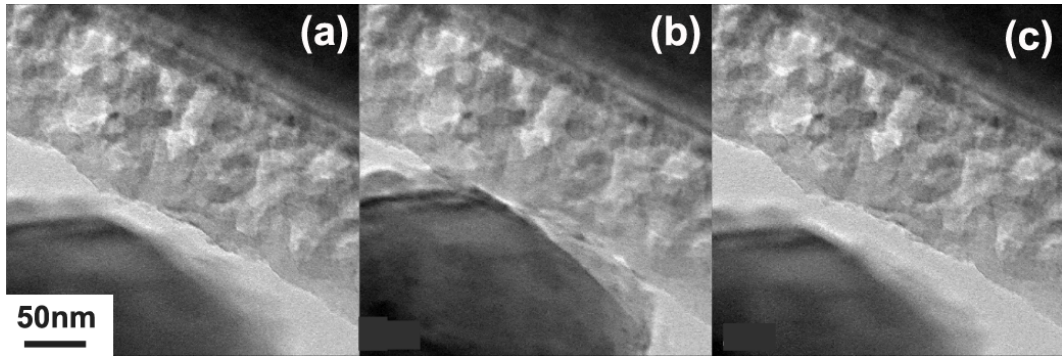


Figure 6.2 TEM images captured from in-situ indentation video upon above load displacement curve with strain range <10%, (a) before indentation (b) at the max deformation point (c) after indentation

As shown in Figure 6.3 are the loading curves with strain range 20%-30%. The curves are plotted against indenter impression depth. All the curves show similar trend, i.e. the load increases with compressive strain and exist two regions similar to the stress-strain curves in bulk materials, i.e. elastic region and plastic deformation region (obviously different hardening rates). In order to further understand such mechanical behavior, the two curves enveloping all the rest curves were selected and plotted in Figure 6.3(b).

Because both regions appear linear trend, thus linear fitting was calculated using the portion of data corresponding to each region respectively and for each curve. For simplicity, the intersection of the linear fitting can be regarded as the onset of plastic deformation in this study. Starting from onset point to the beginning of unloading, all curves show steady increase in load without any drops or significant deflection, thus it can be assumed that the deformation of film is steady and no structural failure or breakage has occurred before unloading. In another word, these films can stand up to 30% strain in these tests.

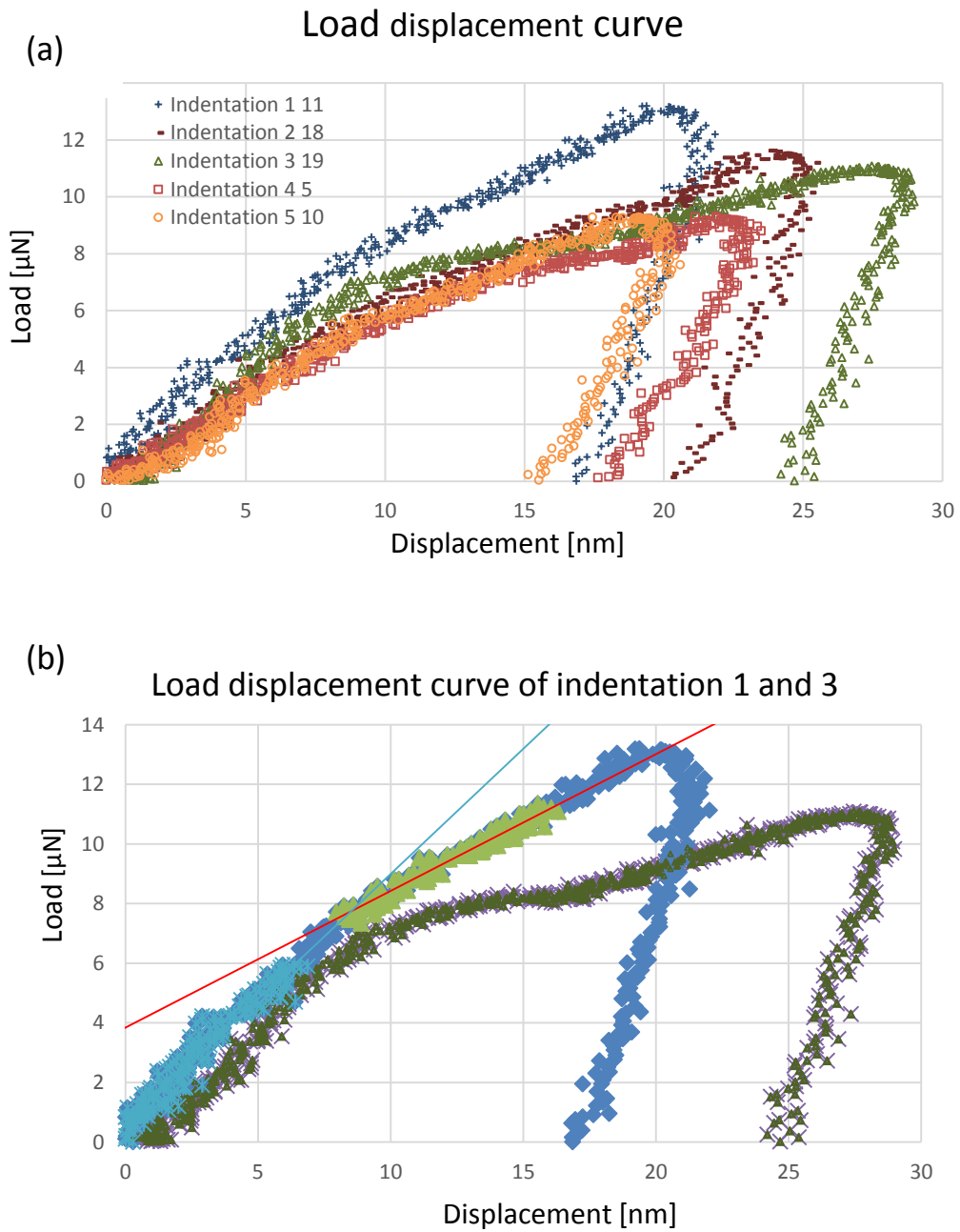


Figure 6.3 (a) Load displacement curve with strain range 20%-30%, (b) Load displacement curve of indentation 1 and 3

In the middle-strain-level tests, a very interesting phenomenon was observed. As shown in series of video frames in Figure 6.4 which was captured from in-situ TEM indentation of np-Si thin film at acquisition rate of 1 image/10 second. This np-Si film

was dealloyed from 150 nm precursor SiMg alloy thin film deposited on Si ridge substrate. The morphology of as-dealloyed np film prior to indentation under TEM mode is shown in Figure 6.4 (a) in which the indenter is also visible close to the film. The film's thickness was measured as ~100 nm before indentation. The as dealloyed np-Si film has an open porosity with the average ligaments size of ~11-13 nm and pore size of ~10 nm. The ligaments circled with dish line in Figure 6.4 (a) became denser (Figure 6.4 (e)) during the indentation loading cycle, showing corresponding decrease in electron transparency. The pore circled with black dish line in Figure 6.4 (a) was being compressed during the loading with a decreased size along indenter loading (Figure 6.4 (e)). When the indenter was removed from the film, this pore acted as initial cracking point, and the right side of the film stucked to the indenter during unloading cycle. Figure 6.5 combined Figure 6.4 (a) and (k) together illustrated the film thickness change before and after indentation. Two parallel white lines were draw along the substrate edge and the top edge of the film. The sponge like interconnected pores and ligaments structure did not collapse after indentation. Instead, the film thickness between the white boundary lines present no noticeable change before and after indentation. The real time load-displacement curve tested from the above video is shown in Figure 6.6. The max load is about ~6 μN corresponding to ~30 nm max deformation. The thin film was deformed to 30% in strain during loading cycle, and it reversed back to its original thickness in unloading cycle in Figure 6.5, which indicated the film recovered from ~30% deformation produced by indentation. This 30% deformation recovery is surprisingly high considering the very brittle nature of Si.

Fredrik Ostlund's et al. [86] studied the Si pillar and reported the maximum engineering strain can reach 22% in the test.

This is interesting because it demonstrates a totally different behavior, i.e. only showed elastic deformation but not any plastic counterparts. As shown by load-displacement evolution against time in Figure 6.7, however, these data eludes the intriguing scenario above. The curves shows that the load bounce back to positive load (tensile load) starting at the beginning of unloading cycle. This might be accounted for by Si being stick to the indenter, thus the compressed thin film was actually pulled back by the indenter. So with this assumption, the fully reversibility is not resulted by elasticity of the film itself. Even though after the film reverse back to the original thickness, no cracks/fractures was observed in thin film. This means that, being deformed by an external force, the film can stand a strain level in the range of 30%, and reverse fully back "intact" without cracking.

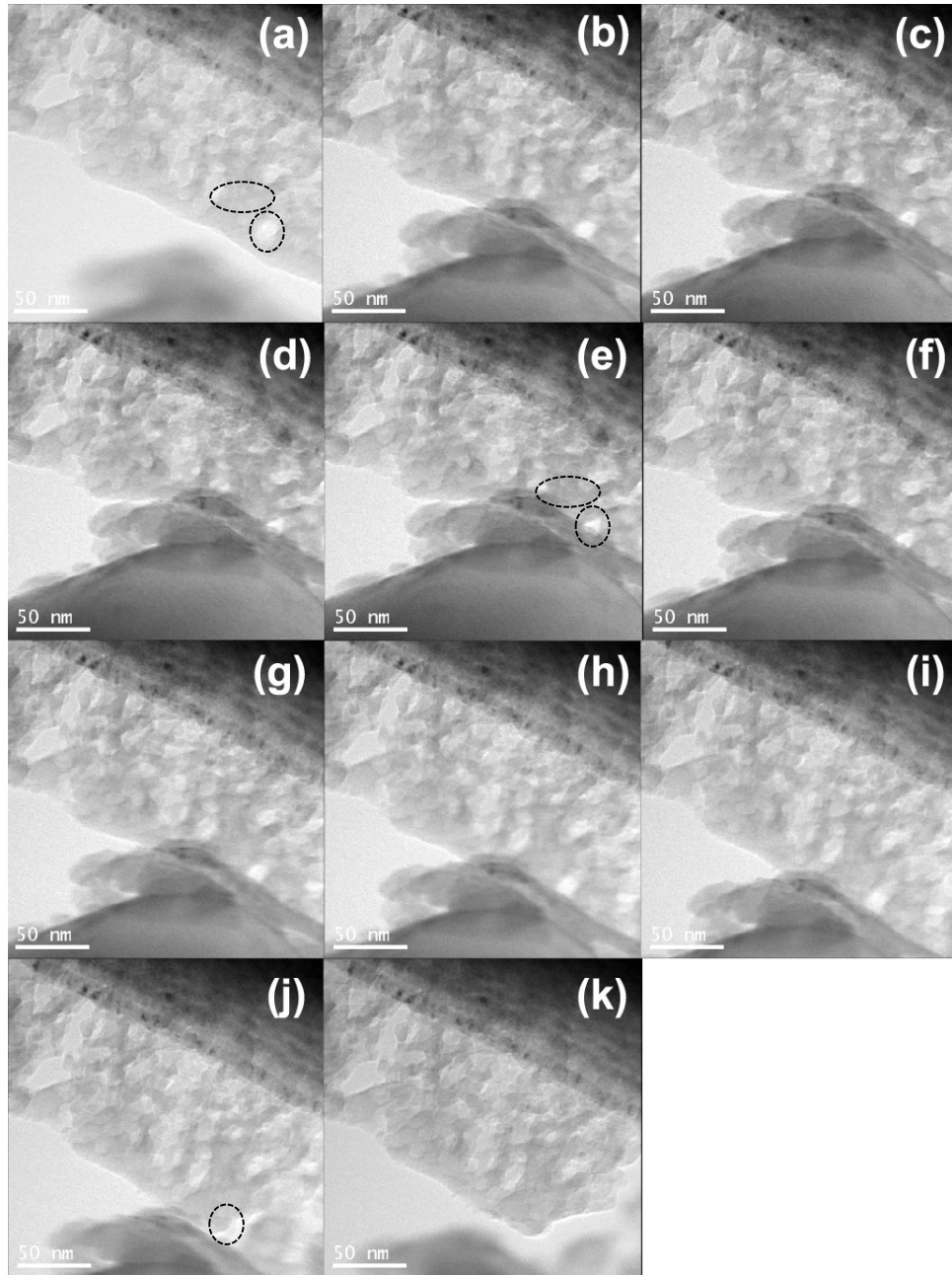


Figure 6.4 Series of video frames from in-situ indentation of np-Si thin film (a)
immediately prior to loading (f) upon removal of load

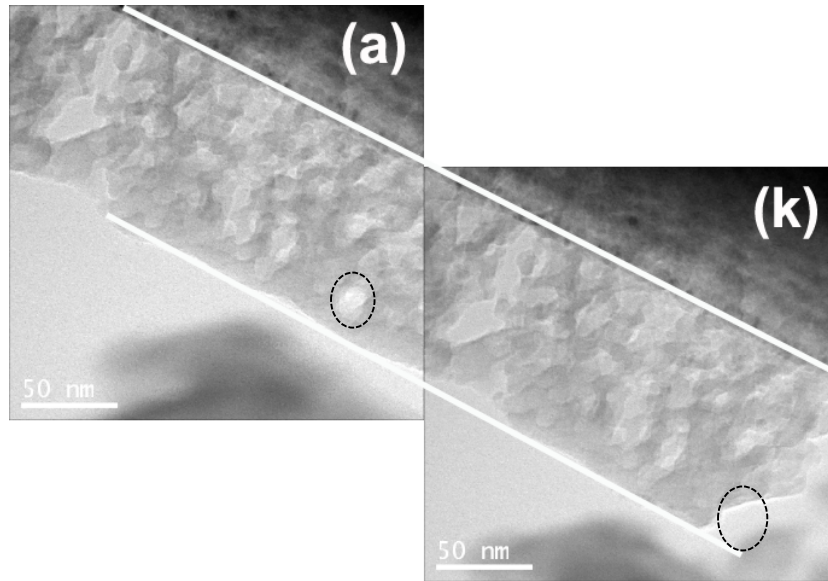


Figure 6.5 Film thickness did not show noticeable change before and after indentation

(a) before indentation (k) after indentation

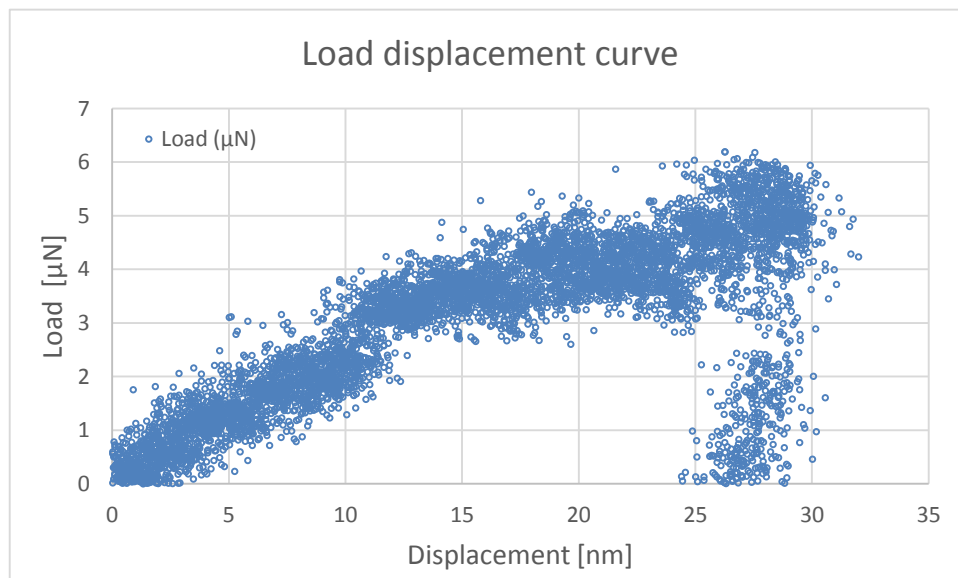


Figure 6.6 Load displacement curve of 100nm film in-situ indentation

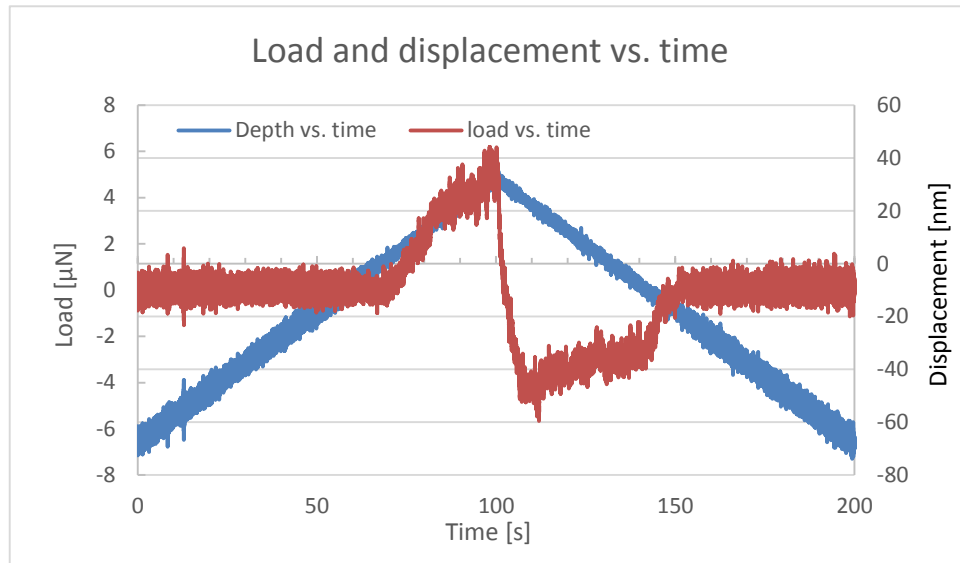


Figure 6.7 Load and displacement evolution during the above indentation

Inspired by such good formability as seen above, the high strain level tests were carried out, as attempts to reaching the maximum potential of the thin films. As noticed in Figure 6.8, the work hardening rate increases with strain. However, this might be contributed by two possible reasons, i.e. (1) actual work hardening from the thin film itself (materials being condensed) and (2) support from harder Si substrate. It is difficult to differentiate the two contributions quantitatively, as the main objective in this study the attention was focused on how much strain the thin film can accommodate. The indentation depth in curve 1 was about 69 nm and two load-drops were observed during this indentation curve. However, there appeared no obvious drop in load displacement curve 2 in Figure 6.8 all the way to 62% strain. The drops in curve 1 were possible because of the np-Si deformed easily in the initial stages of nanoindentation as only the outermost layer of ligaments was compacted by the indenter. Upon further indentation, the "compaction front" of deformed np-Si moved into the film, ahead of the indenter,

successively collapsing each neighboring layer of ligaments. This phenomena has also been observed in np-Au thin film [56]. The different behaviors of the 2 indentations could also be attribute to possible pre-defect in the film/indentation.

The TEM images captured from these two indentations videos are shown in Figure 6.9. Five frames was taken from each indentation video, the images were snap at the second before the indenter touched the film, during the indentation, at the max deformation point, during the unloading, and the final stage, respectively. Figure (a)-(e) in 6.9 correspond to indentation curve 1, (f)-(j) correspond to indentation curve 2. From the Figure 6.9 (e) and (j), it is clear that the film was attached to the indenter during the unloading and pulled away from the substrate. Although ~70% deformation result in film delamination during unloading, it is hard to statistically claim that the thin film has a limit in strain at ~70% because of limited sampling size. More statistical and repeatable tests should be carried out in the future work.

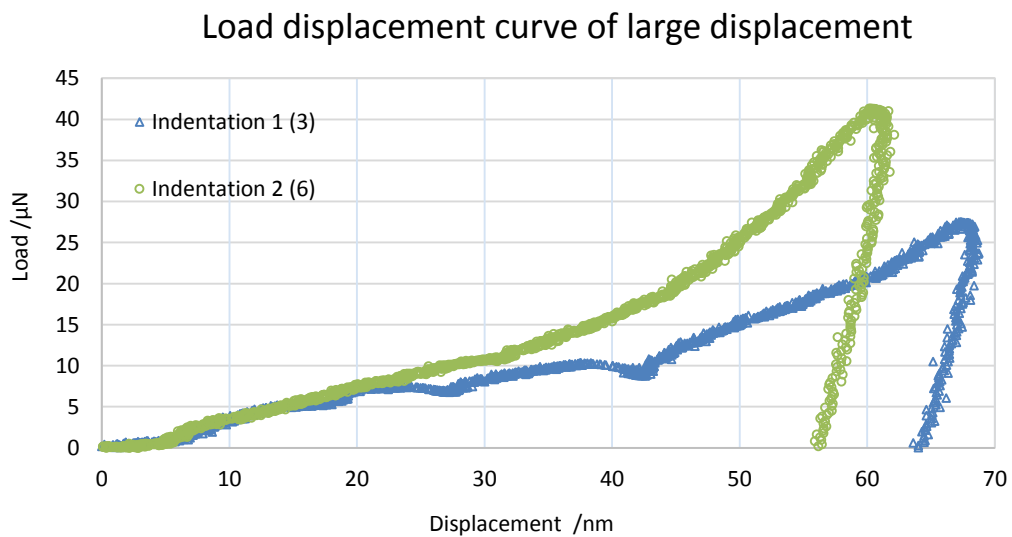


Figure 6.8 Load displacement curve with strain range 60%-70%

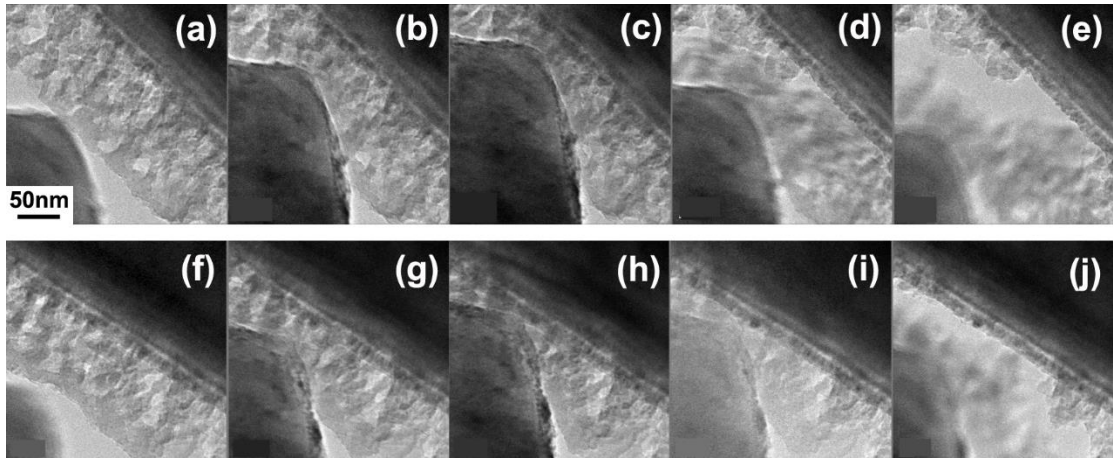


Figure 6.9 TEM images captured from in-situ indentation of large displacement (a)-(e) are from indentation curve 1 (f)-(j) are from indentation curve 2

6.4 Summary

Therefore in summary, the as dealloyed np-Si thin film exhibited a sponge-like behavior in in-situ nanoindentation test which showed very promising and inspiring capability in accommodating compressive stress and strain. Thickness of the np-Si thin film could be fully recovered after the indenter removed from the film under particularly strain. The maximum deformation in thickness was up to 30%, which was impressive considering about the brittle feature of Si. Although this loading mode is different from internal force during lithiation and de-lithiation, these test in this chapter can still imply such thin film is good candidate for Li battery application.

Chapter 7. Response of nanoporous Palladium thin films to hydrogen gas

Palladium (Pd) is a responsive and reliable material for hydrogen sensing due to its selectivity and strong interaction with hydrogen gas. This chapter demonstrates a method to fabricate nanoporous palladium (np-Pd) thin films by dealloying the precursor Pd-Ni alloys that were deposited by magnetron co-sputtering. With an optimized precursor alloy composition and dealloying procedure, the np-Pd films exhibited a uniform, crack-free and sponge-like structure with open porosity. The np-Pd consisted of interconnected ligaments that were each as small as 5-7nm in width. SEM, TEM and EDS were used to characterize the thin films. Changes in np-Pd thin film stress due to hydrogen exposure were measured with wafer curvature system. The high surface area to volume ratio of np-Pd thin film resulted in high sensitivity to H₂, even at low concentrations, and showed promise for future applications of this material as a hydrogen sensor.

7.1 Introduction

Hydrogen has been drawing a lot of attention as a renewable clean energy source [32]. However, as a high explosive and flammable but colorless, odorless and highly diffusive gas, the reliable, fast, accurate and economical hydrogen detector is highly desired for the safety use of hydrogen gas [33, 34]. Around all the alternative hydrogen detection materials, Pd has been considered as a promising candidate because of its

excellent selectivity to hydrogen and high solubility of H in Pd [7]. The reaction between H and Pd is spontaneous and reversible at room temperature. In the reaction of H with Pd, the H atoms occupy the octahedral sites in the face-centered cubic structure of Pd and are able to form the either of immiscible α or β phase, depending on different H/Pd stoichiometric ratio [8]. Such phase transformation results in internal stress change in the structure of Pd, which can be measured as an indicator for the existence of H₂. Although there has been a bunch of commercial Pd thin film sensor, however, most of them only have quick response at a relatively high H₂ concentration. The reliable and rapid detection of low concentration H₂ is still desired to be enhanced the safe use of H₂. Nanostructured Pd thin film, with much larger contact area per volume, is expected to have different hydrogen absorption/desorption behavior that may be used to improve the H₂ sensing techniques [45, 46]. A novel method to fabricate the np-Pd thin film with 15% remnant Ni was presented in this investigation. The investigation of the hydridation/dehydridation behavior study shows the as fabricated Pd thin film had a quicker and sensitive response to H₂.

7.2 Experiments

Sputtering deposition is a technique used to deposit the thin films onto a surface (substrate) by first creating gaseous plasma and then accelerating the ions from this plasma into some source material (target). In this research work, an AJA (ORION system, AJA International Inc., North Scituate, MA, USA) magnetron sputtering system was used to prepare the thin films in which the base and working pressure were

$\sim 10^{-8}$ Torr and 2.5×10^{-3} Torr, respectively. Sputtering was carried out under an inert Ar gas atmosphere at 19.9 sccm at room temperature. The Sub-height was optimized to be 55mm. The 180 μ m-thick single crystalline Si wafers, oriented in (100) with 50nm silicon nitride out layers, were used as the substrate in this research. Sub-clean was conducted on substrates with RF 35 W for 1.5 minutes at pressure 2.5×10^{-2} Torr before film deposition. To increase the adhesion of the films and balance the initial wafer stress, 2nm Ta and 2nm Pd interlayers were sputtered subsequently on both sides of the wafer substrate prior to the Pd-Ni alloy thin film deposition. These basic deposition parameters were kept same for all the following sample preparations in this research.

Dealloying, which is a common corrosion process during which an alloy is ‘parted’ by the selective dissolution of the most electrochemically active of its elements, was used in the present work. The as-deposited Pd-Ni films were immersed in 25% (vol. %) sulfuric acid for several hours to process the dealloying, in which the sulfuric acid reacted with Ni as following: $\text{Ni(s)} + \text{H}_2\text{SO}_4\text{(aq)} \rightarrow \text{NiSO}_4\text{(aq)} + \text{H}_2\text{(g)}$. To achieve the fine porous structure, Oleic acid and Oleylamine acid dissolved in the ethanol was used as the surfactant [63]. The microstructure of the thin films was examined using a high resolution scanning electron microscopy (SEM Hitachi S-900) operated at 6kV. And scanning electron microscopy (SEM, Hitachi S-4300) equipped with a PGT EDS system was used to characterize the chemical composition of the films. In order to exclude the effect of 2nm Pd interlayer on characterization of the chemical composition, the chemical composition measurements of the as deposited and as dealloyed thin films

were carried out on the thin films without the 2nm Pd interlayer. The crystal structure of the as-dealloyed samples was also analyzed using an electrodes transmission electron microscopy (TEM, JEOL 2010F).

The thin film stress map before and after dealloying and in-situ stress evolution during the absorption/desorption was measured with a wafer curvature system (FLX-2320-S, Toho Technology Co.). Ultra-pure nitrogen (99.999% purity) was used to purge the chamber for ~20 minutes followed by absorption/desorption experiments during which zero grade hydrogen (99.9% purity) and nitrogen were controlled by separate flow meters to make the H₂-N₂ mixture at the desired H₂ concentration. A laser with 785nm wavelength was used to scan the film every 30 seconds to measure the internal stress of the thin film.

7.3 Results and Discussion

The morphology of the as dealloyed np-Pd film that exhibits a totally cracking free with uniform fine pores surface is shown in Figure 7.1. The as distributed interconnected sponge like structure exist the ligaments and pores (~5nm in size) contacted with each other. The chemical composition of the precursor PdNi alloy film that results in the most uniform and finest porous structure after dealloying was optimized to be Pd ~20% (at. %). After dealloying in the mixture of sulfuric acid and surfactant for 5 hours, the ~100nm thick as-deposited film exhibited a ~80nm thick structure with nanoporous throughout the whole film. The cross section of the as dealloyed np-Pd sample is shown in Figure 7.1c. The shrinkage of the film thickness may be due to the loss of most Ni

and some Pd during dealloying. Although Pd is nobler than Ni, its slow dissolving in the nitric acid may also result in the decreasing of the film thickness. The amount of the remnant Ni concentration in the as dealloyed film depends on the dealloying time and the original film thickness. For example, 50nm thick film resulted in ~6% (at. %) remnant Ni after dealloying for 5 hours while the 100nm thick film left with ~30% (at. %) Ni for the same dealloying time.

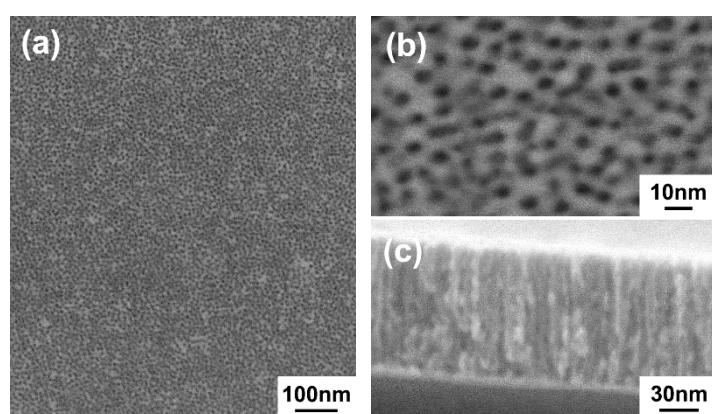


Figure 7.1 (a) and (b) are plan view of 100 nm precursor film dealloyed for 5 hours under different magnification; (c) the cross section view of the same film

To study the details about the ligaments structure of the np-Pd film, ultra thin film (~35nm precursor alloy film) was deposited on SiN_x coated Si wafer followed with ultrasonic cutting, dimpling, chemical etching and dealloying for the TEM observation. Figure 7.2a and 7.2b show the plan view morphology of the np-Pd film in bright field mode under different magnification. The uniformed np-Pd with the ligaments size around ~5nm, some of the ligaments are even smaller with the size 3-4nm. The pore size is around 5nm while some ultrafine pores were able to be observed on the ligament in the STEM image of the np-Pd film as shown in Figure 7.2c. With higher

magnification some pore with even smaller size around 2nm were observed. The selected area electron diffraction (SAED) pattern shows diffraction rings (Figure 7.2d), suggesting that the as-dealloyed np-Pd was polycrystalline. The characteristic rings in the polycrystalline can be indexed to the {111}, {220} and {311} allowed reflecting planes expected from fcc Pd.

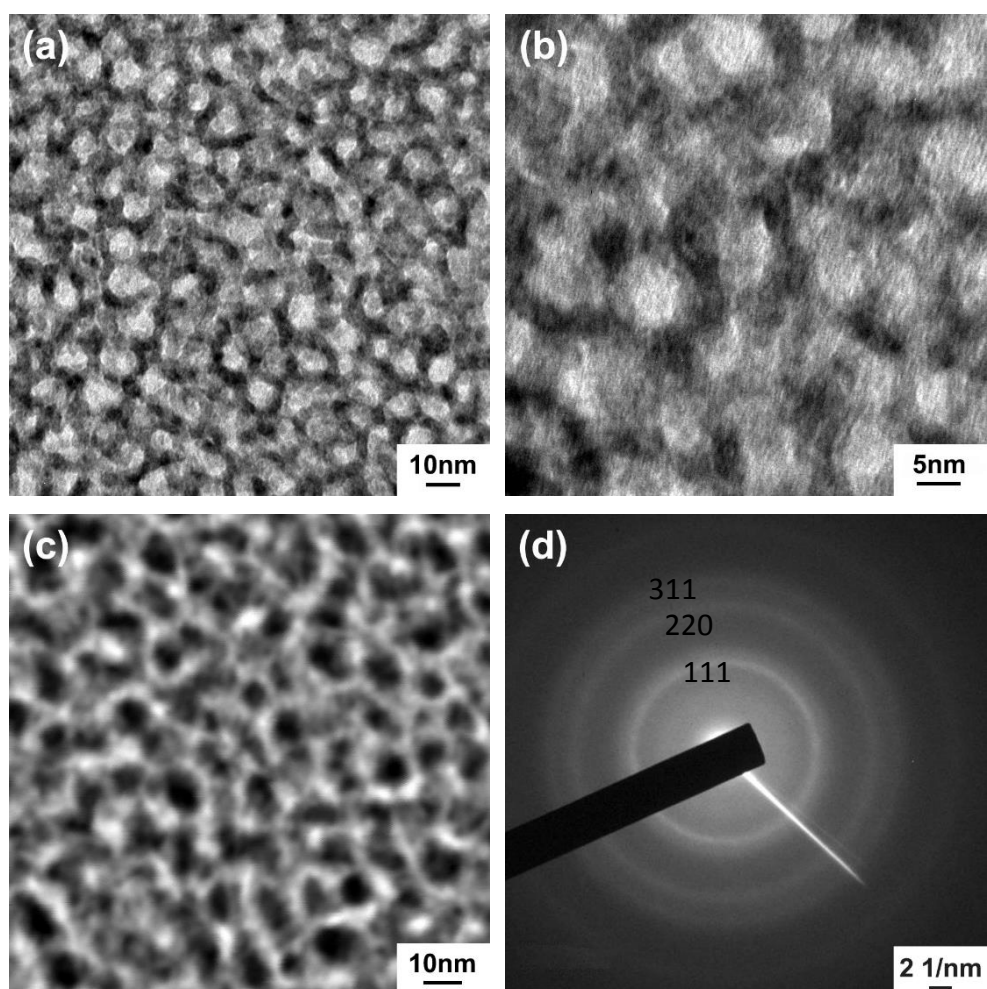


Figure 7.2 (a) , (b) and (c) TEM images of the np-Pd thin film; (d) diffraction pattern of the film

The film stress was measured using the wafer curvature system (FLX 2320 S, Toho Technology Co.). The laser source with 785nm wavelength was used to scan the film

every 45° to distribute a 3D stress map that could indicate the stress situation of the entire film. The film stress was calculated by the Stoney's equation:

$$\sigma_f = \frac{E_s}{(1-\nu_s)} \left(\frac{h_s^2}{6Rh_f} \right) \quad \text{Equation 7.1}$$

Where:

E_s is Young's modulus of the substrate, ν_s is Poisson's ratio of the substrate, h_s is substrate thickness, h_f is film thickness and R is radius of the curved substrate (thin film).

The stress of 300nm as deposited PdNi film was mapped on a 3 inch Si wafer coated with 50nm silicon nitride. The initial stress of bare wafers was measured with a quartz plate every 45° before deposition and the stress introduces by the Ta and Pd interlayer was subtracted. Figure 7.3a shows the stress map of 300nm precursor PdNi alloy film. During dealloying, as the Ni atoms dissolve in the sulfuric acid the Pd atoms diffused to form the np-Pd ligaments. The as deposited PdNi precursor film holds an average 762.49MPa stress and after dealloying for 21 hours the film stress relaxed about 700 MPa from its original stress level, which decreased to 39.77 MPa as average, as shown in Figure 7.3b.

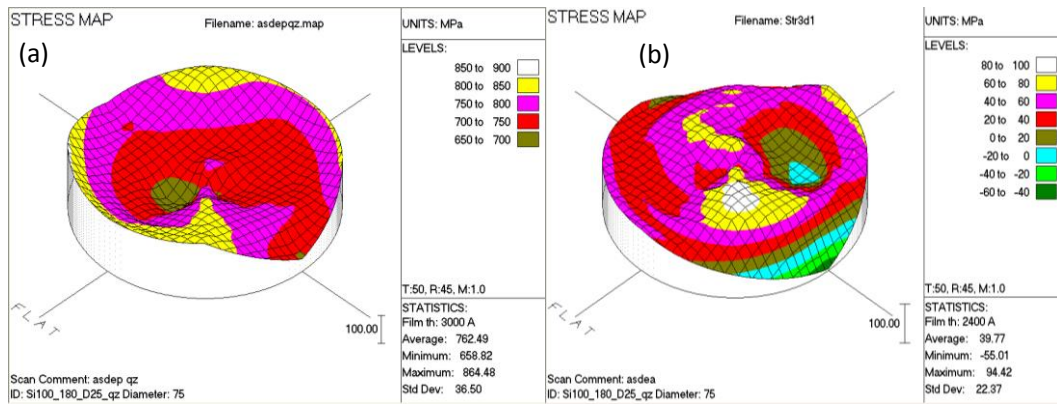


Figure 7.3 (a) and (b) are stress map of 300nm film before and after dealloying, respectively

300nm precursor PdNi thin film and 100nm dense Pd thin films were deposited for the hydridation experiment. After being dealloyed in sulfuric acid mixture for 21 hours, the as dealloyed np-Pd film exhibited a ~240nm thick porous structure with the ligaments size around 5~7nm. The remnant Ni content was around 15 at. %. As R. C. Hughes [89] reported that, compared with the pure Pd film, remnant Ni (15 at.%) in PdNi alloy could be a good material for hydrogen sensor due to that the Ni can cause the Pd lattice to contract and suppress the transition from α to β phase. 15ml/min hydrogen under 1 atm pressure was mixed with the 99.99% purity nitrogen gas to form the hydrogen gas mixture with the concentration 0.53% (vol.%). The H₂ was controlled by the flow meter between 0 and 0.53% (vol.%) with the N₂ was flown in during the whole measurement. The stress curves of the pure Pd film and the np-Pd film during the hydridation/dehydridation test are shown in Figure 7.4. Once contacting with hydrogen, the pure Pd film has a rapidly compressive stress drop as shown in Figure 7.4a. The dense Pd film stress was kept going down for over 10 minutes to reach its plateaus in the compressive

stress region, and after switching off the H_2 gas the film stress gradually relax to its starting stress level in 30 minutes. The as dealloyed 240nm np-Pd film which has comparable Pd atom number to the 100nm dense Pd film was tested with the same H_2 absorption/ desorption cycling. The np-Pd film shows a rapid compress stress response to the hydrogen within 30 seconds when contacting with H_2 , and presented a significant different behavior during the dehydration process compare with dense Pd film. After closing H_2 , the film stress rapidly relaxes back to its original stress within one minute, which is tens times faster than the dense film (Figure 7.4b). The average stress changes corresponded to H absorption and desorption in the film, about 17 MPa, had a stable repeatability during the cycling. The slightly increasing trend of the whole curve during the whole experiment was believed to be due to the N_2 , as the stress was increasing slowly with the time under pure N_2 flow in. Although the dense film has much higher capacity to absorb hydrogen, however it has longer response time compare with the porous film. There are may be two reasons of the high response time of the np-Pd, one is the porous structure of the film provides more contact area between the Pd and the H_2 gas which cause the H_2 molecular adsorption and dissociative chemisorption easier than on the dense film; another one is the fine ligaments ensure the following absorption step has shorter and faster hydrogen diffusion path than the dense film [90]. When the hydrogen atoms contact with Pd, they prefer to located at octahedral interstitial sites, causing the lattice expansion and introducing the compressive stress in the film. The porous structure provides sufficient room for the Pd ligament during the hydridation and dehydration, which increase the sensitivity of the Pd film to the hydrogen and

avoid the film cracking during the process.

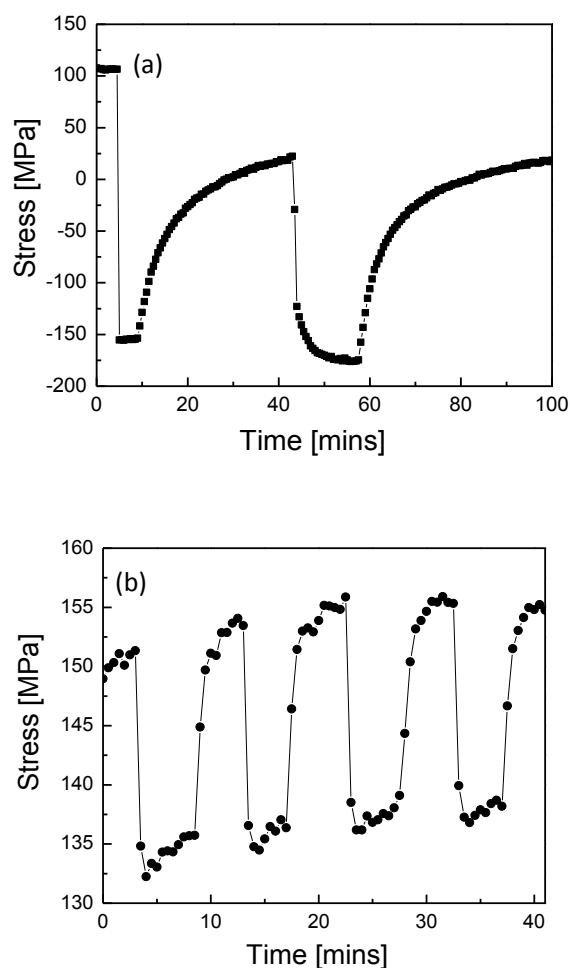


Figure 7.4 (a) Stress curve of 100 nm dense Pd film during H₂ cycling measurement

(b) Stress curve of 240nm np-Pd film during H₂ cycling measurement

The film stress change of 100nm dense Pd film and 240nm np-Pd film was also studied with varying H₂ concentrations, respectively. During the experiment N₂ gas was kept flowing into the chamber while the H₂ gas was opened each time with different H₂ flow rates to generate different H₂ partial pressure ranging from 1.8 mbar to 10.6 mbar. At each desired H₂ concentration, H₂ was hold about ~5 minutes for data recording. For the np-Pd film, the stress drop between the starting point and the first lowest point after

flowing into H_2 was considered as the film stress change due to the hydridation. For the dense Pd film the stress change between the starting point and the average of the plateau was taken as the stress change due to H_2 . The different hydridation slope of forming phase transformation (α to β) region has never presented in this experiment on either dense Pd film or np-Pd film. For the np-Pd film, the film stress dropped to its lowest level and reached its plateau with in one minute. As shown in Figure 7.5a, the stress change increases with the partial pressure of H_2 . The stress change of the dense film varies from ~140 MPa to ~300MPa while that for np-Pd film varies from ~12MPa to ~24MPa. The relationship between the log-scaled stress change of the film and log-scaled partial pressure of H_2 indicates that the dense Pd film and the np-Pd film have the slopes about 0.41 and 0.35 (Figure 7.5b), respectively, which is slightly lower than Sievert's constant (0.5) that describing the H_2 solubility in Pd metal [91].

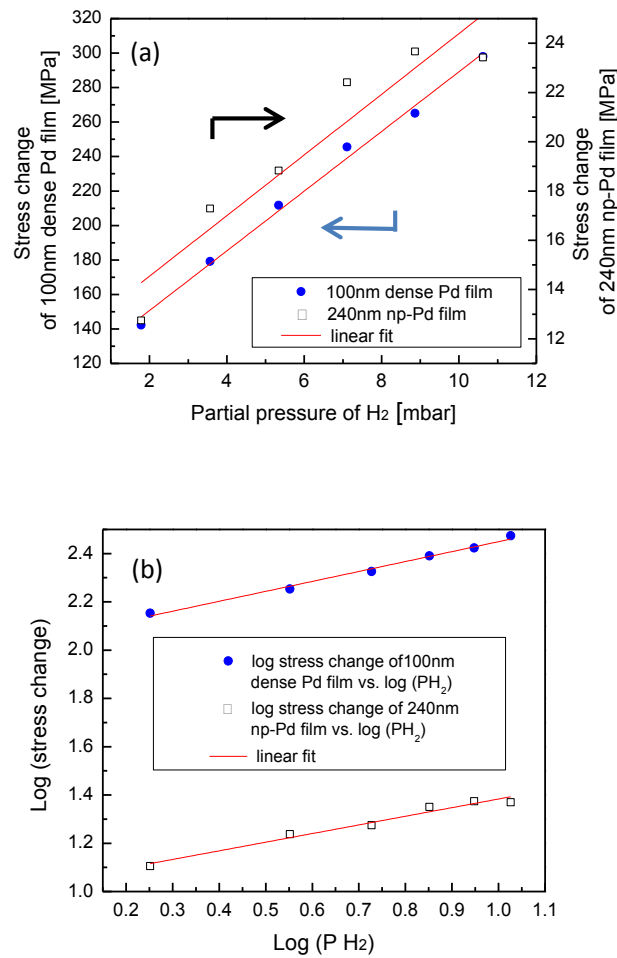


Figure 7.5 (a) Plot of stress change and partial pressure of H₂ (b) Plot of log (stress change) and log (partial pressure of H₂)

7.4 Summary

Fine np-Pd film with the ligament size around 5~7nm has been fabricated by dealloying as deposited PdNi thin film with suitable etchant. The optimized precursor alloy composition and dealloying procedure that yielded the best nanoporous structure has been developed. The morphology of the cracking free sponge like interconnected ligament structure has been studied by SEM and TEM. The hydridation and

dehydration behavior of the np-Pd film has been investigated by the stress change in the film during the absorption and desorption process. The as fabricated porous Pd film exhibited high sensitivity to low concentration H₂ gas, which is promising to be used as the hydrogen sensing materials in the future.

Chapter 8. Transfer from single layer np-Pd to multi-layer np-Pd thin films

8.1 Introduction

Nanostructured materials always refers to those materials with structural elements, clusters, crystallites or molecules, with the dimension within 100nm range [92]. With the high surface area to volume ratio and the nanoscale size effect on the physical and chemical property, it has received both academic and industrial attention in the last decades. Among all the nano structure synthesis methods, dealloying, also refer as selective dissolution, is one of the most efficient method to fabricate np structured material [93, 94]. Dealloying has been widely studied to fabricate porous material, np-Au from Au-Ag alloys [95], monolithic np-Cu from Mn-Cu alloy [96], np-Pd from Pd-Ni [97]. Conventional dealloying does not allow precise control of pore size. However, precursor alloy composition and dealloying conditions such as etchant concentration, dealloying temperature, dealloying time, agitation of etchant has significant effects on morphology of the as dealloyed structure [98]. Low temperature dealloying technique was developed by L. H. Qian et al. to tailor the characteristic length scale of np-Au in order to achieve the ultrafine np Au for advanced functional applications [99]. Thermal cycling was also reported by Ye Sun et al. [100] to widen the np-Au as dealloyed ligaments. Lei Wang et al. [101] tailored the np-Au and np-Ir structure by dealloying multilayered precursor to achieve the layered np architecture. However, predictable

design or quantitative control of pores and ligaments geometry cannot be controlled by dealloying normally. In this chapter, np-Pd was controlled by dealloying multilayered PdNi precursor film. The thickness combination of the multiple layer has been carried out to manipulate the np structure.

8.2 Experimental

The multilayer deposition was also fabricated in AJA (ORION system, AJA International Inc., North Scituate, MA, USA) magnetron sputtering system. The base and working pressure were $\sim 10^{-8}$ Torr and 2.5×10^{-3} Torr, respectively. Sputtering was carried out under an inert Ar gas atmosphere at 19.9 sccm at room temperature. The Sub-height was optimized to be 55mm. The 180 μm -thick single crystalline Si wafers, oriented in (100) with 50nm silicon nitride out layers, were used as the substrate in this research. Sub-clean was conducted on substrates with RF 35 W for 1.5 minutes at pressure 2.5×10^{-2} Torr before film deposition. To increase the adhesion of the films and balance the initial wafer stress, 2nm Ta interlayers were sputtered subsequently on the wafer substrate prior to the Pd-Ni alloy thin film deposition. These basic deposition parameters were kept same for all the following sample preparations in this research. The dealloying was processed in 25% (vol. %) sulfuric acid with Oleic acid and Oleylamine acid as the surfactant. The microstructures of the thin films were examined using high resolution scanning electron microscopy (SEM Hitachi S-900) operated at 6kV.

8.3 Results and Discussion

The deposition of multilayer samples were fabricated by programming the gun shutters to open and close in a sequential order. Four different multilayer samples with different Pd interlayer thicknesses has been investigated. The details of the film layer configuration are shown in Table 8.1. To increase the adhesion of the film to substrate, 2nm Ta and 2nm Pd interlayer was sputtered before the film deposition in all situation. In the previous study results on the np-Pd thin film , the nano pores of Pd has the size of 5-7 nm. Therefore, 14 nm, approximately pore size plus ligaments size, was deposited as the interlayer thickens for most of the cases. Multilayer sample 1 (ML1) namely has a three-layer structure. 2nm Pd interlayer was sputtered between each PdNi alloy layer and the deposition sequence was repeated for three times. Multilayer sample 2 (ML2) has 74 nm thickness with 5 layers of PdNi alloy film separated by 1nm Pd layer. Multilayer sample 3 (ML3) has similar layer structure as ML1 but has two more layers than ML1. Multilayer sample 4 (ML4) also has five layers, instead of 14 nm thick for each PdNi alloy layer, 20nm PdNi film being deposited between each 2nm Pd separation layer. The PdNi precursor alloy layer was deposited under Pd and Ni targets powered by DC at 10W and 143W respectively. The deposition setting would result in 18 at. % Pd in the PdNi alloy layer as studied in Chapter 7.

Table 8.1 Schematic diagram of 4 multilayer samples

	14nm Pd-Ni	14nm Pd-Ni	20nm Pd-Ni
	1nm Pd	2nm Pd	2nm Pd
	14nm Pd-Ni	14nm Pd-Ni	20nm Pd-Ni
	1nm Pd	2nm Pd	2nm Pd
14nm Pd-Ni	14nm Pd-Ni	14nm Pd-Ni	20nm Pd-Ni
2nm Pd	1nm Pd	2nm Pd	2nm Pd
14nm Pd-Ni	14nm Pd-Ni	14nm Pd-Ni	20nm Pd-Ni
2nm Pd	1nm Pd	2nm Pd	2nm Pd
14nm Pd-Ni	14nm Pd-Ni	14nm Pd-Ni	20nm Pd-Ni
2nm Pd	2nm Pd	2nm Pd	2nm Pd
2nm Ta	2nm Ta	2nm Ta	2nm Ta
Substrate	Substrate	Substrate	Substrate
ML1*	ML2	ML3	ML4

* MLx = Multilayer sample x

The composition of the multilayer samples before and after dealloying was tested by EDS as shown in Table 8.2. Because of the Pd separation layer, the Pd content in the as deposited multilayer samples were all higher than the single layer PdNi thin film. Oleic acid and Oleylamine acid mixed with ethanol was kept using as surfactant in the multilayer sample dealloying as it immobilize surface diffusion of Pd atoms during dealloying [63]. The dealloying was processed in 25% (vol. %) sulfuric acid with surfactant for 7 hours. The EDS was conducted on the as dealloyed film for composition. The ML1 had only 5.65 at. % Ni left after dealloying, up to 94.5% Pd remained in the film, which was a higher Pd content than single layer np-Pd film. ML2 and ML3 had 42.2 at. % and 50.6 at. % residual Ni, respectively, maybe due to the partial dealloying.

ML4 has a relatively high Pd content after dealloying among these multilayer np-Pd films.

Table 8.2 Composition of multilayer samples

	ML1		ML2		ML3		ML4	
at. %	Ni	Pd	Ni	Pd	Ni	Pd	Ni	Pd
As-deposited	73.2	26.8	73.5	26.5	67.9	32.1	77.6	22.4
As-dealloyed	5.65	94.5	42.2	57.8	50.6	49.4	17.6	82.4

The ML1 did not result in np structured Pd after dealloying. The possible reason is that three PdNi alloy layers structure with 2nm Pd separation layer resulted in Pd rich in the whole structure and most of the Ni atoms was etched during dealloying leading to Pd dense structure. As shown in Figure 8.1 is the morphology of ML2 in which the pores size and ligaments width were determined from measurements of plan view SEM images. At least 50-100 ligaments were measured for a decent statistics (same for following measurements) and the results indicated that the uniformly distributed np structure consisted of pores and ligaments of approximately 5.1 nm and 7.0 nm in size respectively, which was the same size scale with the single layer np-Pd. However, the cross section of the ML2 did not appear any layered structure as expected.

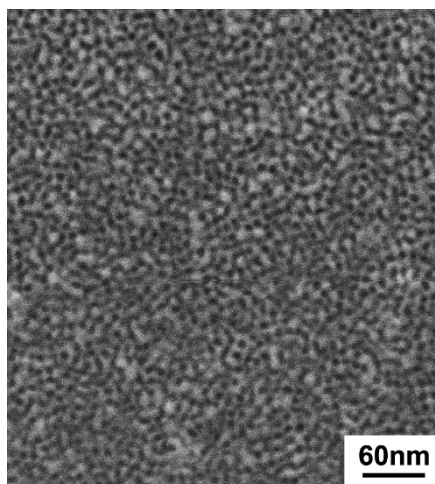


Figure 8.1 Morphology of ML2, pores are approximately 5.1 nm and ligaments are about 7.0 nm

The ML3 appears np structure with ~ 3.7 nm pore size and ~ 7.8 nm ligaments. The surface morphology of ML3 is shown in Figure 8.2 (a). The porous structure appears denser than ML2. Layered structure has been observed in the cross section structure of ML3 (Figure 8.2 (b)) where the three pure Pd layers could be distinguished from the image. The porous layer between the dense layers appears indeed porous, however, the ligaments that stand between the boundary layer were much wider than the ligaments on the surface. Overall, the ML3 has layered structure after dealloying, the np-structure is denser than ideal layered np-Pd structure.

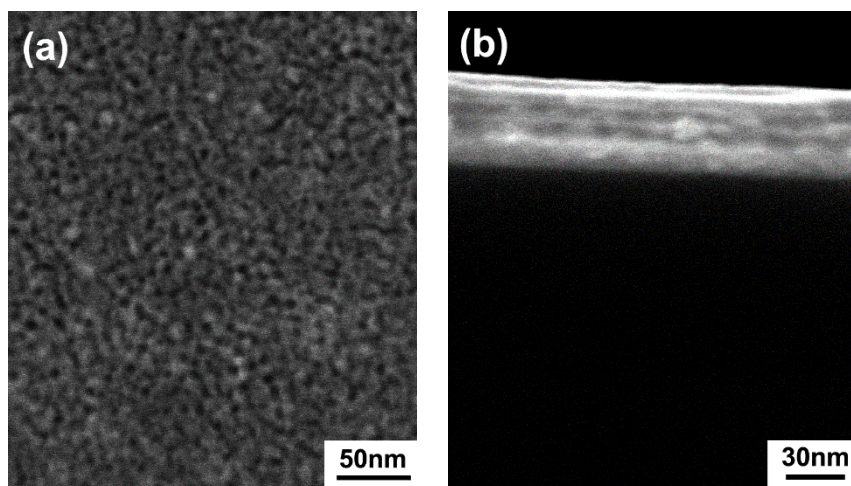


Figure 8.2 Morphology of ML3 (a) plan view (b) cross section view

Layered np structure was observed in ML4 throughout the whole film. The pore size and ligament size as measured from the surface SEM image of Figure 8.3 (a) are $\sim 5.2\text{nm}$ and $\sim 6.7\text{nm}$ respectively. The pore and ligament sizes of ML4 are close to those of single layer np-Pd thin film samples. In precursor ML4 thin film sample, 5 layers of 20nm PdNi alloy were separated by 4 layers of 2nm Pd. Cross section SEM images are shown in Figure 8.3 (b) and (c) demonstrating the internal film morphology after dealloying. 4 porous layers and 3 separating Pd layers were visible. Approximately 9.4nm dense top layer appears on the surface layer. Figure 8.3 (d) was enlarged from Figure 8.3 (c) to illustrate the details of the layered structure. The average spacing (porous layer plus pure Pd layer) of ligament layers was measured as 8.7nm . The ligaments along the separation 2nm pure Pd layer was measured as 4.4nm after dealloying, which probably was due to the Pd atom diffusion and agglomeration during dealloying towards the Pd rich layer. The bridging ligaments between two layers were oriented perpendicular to the pure Pd layers, similar to the phenomenon as reported by Lei Wang in multilayer Ir/Ir-Ni and Au/Au-Ag film [101].

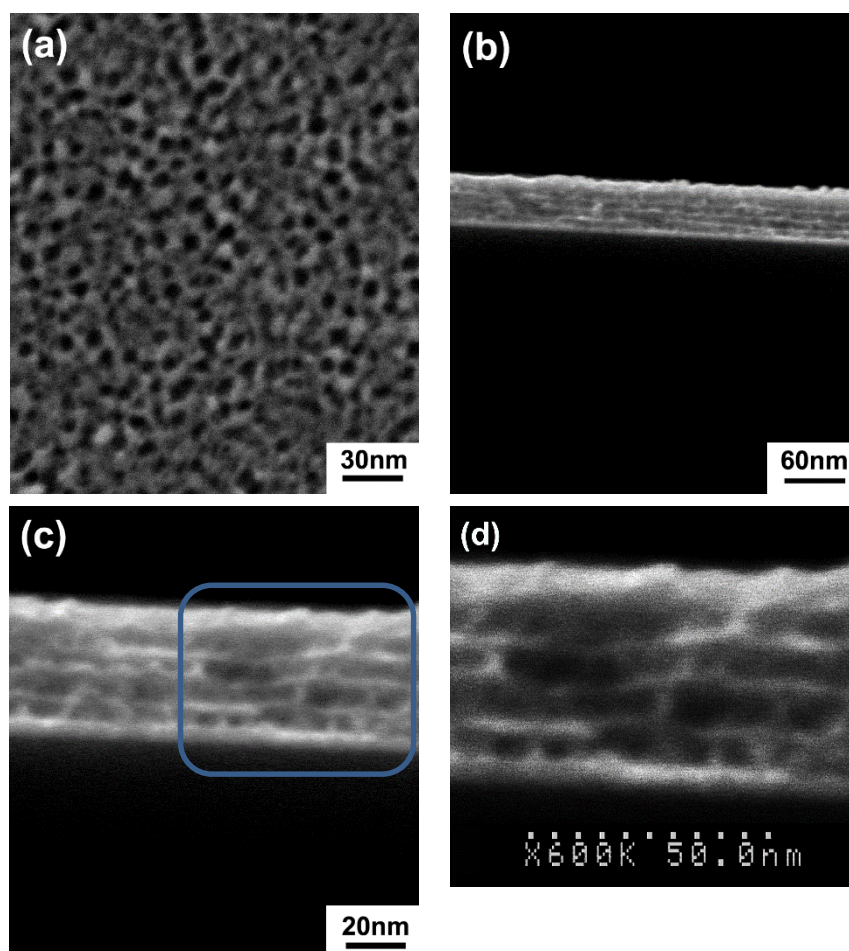


Figure 8.3 Morphology of M-4 (a) plan view, (b) and (c) are the cross section view under different magnification, (d) enlarge of the square marked region in (c) with its original scale bar

The np-Pd dealloyed from single layer PdNi alloy film are shown in Figure 8.4. The 100 nm precursor PdNi film was deposited with the same deposition power as the one used in deposition of the PdNi layer in the multilayer films. In other words, the film composition of this single layer film has the same composition as the PdNi alloy layer in the multilayer film. From the cross section view, the ligaments appeared straight forward from substrate to the top of the np-Pd film. Comparing it with the multilayered

np-Pd/Ni (Figure 8.3 (d)), the ML4 revealed apparently different structure than regular np-Pd thin film. From the EDS result, after dealloying, the Ni content in the film is about 17.6 at. %, which is even lower than the residual Ni in the as-dealloyed single layer np-Pd film. The separation pure Pd layer did not behave like an atom diffusion barrier during dealloying, instead it served as a ‘seed’ layer during the formation of the np structure. The Pd layer changed the diffusion and agglomeration of Pd atoms during dealloy yields, unlike single layer film which yielded perpendicular ligaments distributed between the layered structures.

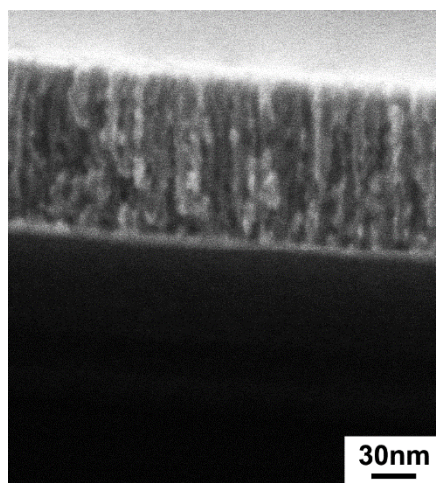


Figure 8.4 Cross section as dealloyed single layer 100nm precursor PdNi film

The pore and ligaments size was indeed affected by the thickness combination of different layers. Among the three samples that resulted in np structure after dealloying, ML2 has 5 layers of 14 nm PdNi with 1 nm pure Pd; ML3 had 5 layers of 14 nm PdNi with 2 nm pure Pd; ML4 had 20nm PdNi with 2 nm pure Pd. After dealloying, ML2 resulted in 5.1 nm pores and 7.0 nm ligaments; ML3 3.7nm pores and 7.8 nm ligaments and ML4 5.2 nm pores and 6.7 nm ligaments. The ML2 and ML3 had same thickness

of PdNi alloy layer but different thickness of separation Pd layer, as the ML2 did not presents any layered structure after dealloy, it revealed that if the pure noble metal layer is too thin to provide a ‘seed’ layer for the noble metal to diffuse and aggregate during dealloying, thus the layered structure would not be formed. ML3 and ML4 has the same thickness of separation Pd layer but different thickness of alloy layer, although they both showed np layered structure after dealloying, The structure of ML3 is much denser than that of ML4. In sum, the thickness ratio of the alloy layer and pure metal layer would play a role on the finished np structure. For np-Pd, the optimized alloy layer thickness is 20 nm instead of 14 nm as sum of the pore size and ligament size in single layered np-Pd thin films.

8.4 Summary

The as-deposited multilayer PdNi films with various configuration of alloys and pure Pd layers, different thickness combination led to different as dealloyed np structure showing layered architecture. The as dealloyed film presented periodic cells with ordered ligaments layers throughout the film thickness. The bridge ligaments between the layers oriented vertically to the bounding layers. The pores and ligaments size could be controlled by tuning the thickness of the PdNi alloy layer and the separation layer. Manipulating the alloy / pure metal thickness could lead to achieve the desired structure with targeted ligaments and pore size. Too thin noble metal separation layer would not provide the ‘seed’ for the noble metal to diffuse and aggregate during dealloying and too thick separation would create a barrier that slow the further dealloying underneath

it. For the future work, film with more layers should be explored to study the thickness effect of the alloy and separation layer on the final layered np structure. By adjusting thickens ratio of the alloy and pure element, the pore and ligaments size could be manipulated. Desired np structured Pd could be fabricated for sensing and storage application.

Chapter 9. Bulk nanoporous Pd with ultra-fine pore size

9.1 Introduction

Nanoporous metals could be fabricated via dealloying by remove the less noble metal in the alloy system and leaving a nanoporous sponge like structure of the more noble metal throughout the entire sample. This technic has been applied to various alloy system to produce np-Au [102], np-Pt [60], np-Ni [103], np-Cu [104] and np-Si [105]. Among all these np-structured samples, np-Pd that offers high amount surface area draws a lot attention due to its great potential for catalytic application, hydrogen storage and sensing application. Xiaoguang Wang et al. [106] achieved fine ligaments size np-Pd via dealloying PdAl alloy in alkaline solution. Masataka Hakamada et al. studied the dealloying behavior and structure of Pd-M (Fe, Co, Ni) alloys [107] as well as the thermal coarsening of np-Pd [108]. Nanoporous materials may exhibit mechanical properties difference from their dense/bulk counterparts, and offer an opportunity to study size effects in mechanical behavior. Fredrik O Stlund, et al.[86] discovered when the size range is reduced from 1 μ m down to 200 nm the Si columns transited from predominantly brittle to ductile behavior at room temperature. When the ligaments size of np-Au decreased to 10 nm, the shear stress of the np-Au film increased to approximately 60% of the realistic estimate of the theoretical shear strength for gold [56]. Although research has been conducted on the preparation of the np-Pd, the mechanical behavior of the as fabricated np-Pd has never been studied. In this chapter, we discussed the fabrication of np-Pd by electrochemical dealloying bulk PdNi and

PdCo alloy which resulted in very fine np structure, as well as the in-situ TEM indentation behavior of the as fabricated np-Pd. The research on the mechanical behavior of the np-Pd would help to understand the hydridation mechanism of np-Pd.

9.2 Experimental

Ni and Co were selected as the sacrificial elements to fabricate the np-Pd. Pure Pd (99.9%) sheet, pure Co sheet (99.9%) and pure Ni (99.9%) pellet were weighted proportionally to produce the alloy precursor bulk PdNi and PdCo samples by arc melter. Various composition combinations: Pd₁₄Ni₈₆, Pd₁₈Ni₈₂, Pd₂₀Ni₈₀, Pd₂₂Ni₇₈ and Pd₂₀Co₈₀, have been tried to obtain the best precursor alloy composition that yields the optimized bulk np-Pd structured sample after dealloying. The Edmund Bühler Compact Arc Melter MAM-1 was used in this study to fabricate the Pd alloy ingot. The vacuum chamber of the arc melter was purged with 2.5 atm Ar gas for 3-4 times for 3 minutes each time. The samples were melted with Ar gas flowing under 0.5mbar absolute pressure and each sample was flipped 4-5 times to uniform the Pd and Ni/Co distribution in the sample. In addition, annealing at 1000 °C under Ar atmosphere for 24 hours was applied to the as melted Pd₁₄Ni samples for homogenization. The as melted spherical samples were cut into 500µm thick pieces with the precision diamond saw (Isomet, Buehler). Then the sliced thin sample was mounted, grinded and polished with final finishing using 1µm diamond paste before dealloying.

To optimize the dealloying procedure, free corrosion dealloying, step dealloying and electrochemical dealloying have been explored. For the free corrosion dealloying, the

H₂SO₄ with and without surfactant under different concentration and various dealloying temperature have been attempted. The three electrodes electrochemical dealloying system and electrolyte were applied to form the nanoporous structure with a potentiostat (eDAQ) for all dealloying process. In this system, 0.1mol/L H₂SO₄ was, Pt and Ag/AgCl were used as the electrolyte, the counter electrode and the reference electrode, respectively, while the polished samples with various dimensions attached with an Ir wire holder was used as the working electrode. Samples were weighted before and after dealloying to track the weight loss due to dealloying. And the exposed area to the electrolyte of each sample was measured each time for the current density calculation. The anodic polarization measurement was conducted in order to find the critical potential. Different dealloying potentials have been tried to obtain the best np structure. The finishing of the dealloying was indicated by the current approached to zero on the dealloying current vs. time schematic. Dealloying time varies due to the size of the sample. The samples were rinsed with and immersed in distilled water, followed by using ethanol to remove the residual H₂SO₄ after dealloying. The scan rate for electrochemical dealloying was 20mV/s.

The structure of the as melted and as dealloyed samples were then studied under scanning electron microscope S-4300 (Hitachi) and S-900 (Hitachi). The Hitachi S3200 SEM was used to perform EDS analysis on the samples to determine the composition. The as fabricated bulk np-Pd was milled into np-Pd pillars by focused ion beam (FIB) under Zeiss SEM to perform the in-situ Pd pillar indentation.

9.3 Results and discussion

9.3.1 Microstructure study of np-Pd dealloyed from Pd₁₄Ni₈₆ precursor alloy

The amount of Pd and Ni based on the calculation that gave the desired atomic percent PdNi alloy always resulted in higher Pd content after arc melting which indicated that there was high Ni loss during the arc-melting process. To achieve the desired atomic percent sample, arc melting was applied multiple times to tune the Ni amount to approach the desired composition. The composition of the as melted PdNi samples were cut and checked by EDS on Hitach 3200 under area scan mode.

As listed in Table 9.1 is the dealloying condition on the Pd₁₄Ni₈₆ samples. At the beginning, the same dealloying method of fabricating np-Pd thin film was carried out. After free dealloying in concentrated H₂SO₄ at 25 °C for 1 day, the Pd content in the alloy increased from 14% to 31% (at.%). After dealloying for 5 days, some nano sized pores showed on the sample surface (Figure 9.1 (a)), however, the Pd content is about 38%, indicating that large amount of Ni was still under dealloying. The morphology of the sample dealloyed in concentrated H₂SO₄ without surfactant at room temperature for 5 days showed less porosity (Figure 9.1 (b)). The step dealloying was conducted on the polished Pd₁₄Ni₈₆ sample. The first step was carried out in concentrated H₂SO₄ with surfactant for the 1st day at 50 °C, then the sample was kept immersed in the etchant at room temperature for the following 6 days for the second step dealloying. As observed with SEM and EDS, cracks grew along the grain boundary after the first step dealloying and no porosity exhibited after the second step dealloying and Ni was left in the alloy.

All the dealloying conditions that are listed in Table 9.1 have been attempted to pursue the np-Pd structure, however, none of the above dealloying procedure results in promising np-Pd structure.

Table 9.1 List of the free corrosion dealloying condition of Pd₁₄Ni₈₆

	Temperature °C	Concentration of H ₂ SO ₄	Dealloying time /Days	Surfactant
Dealloying	Room temperature	25%	5	with
	Room temperature	concentrated	5	without
	25	concentrated	1	with
	25	concentrated	5	with
	50	25%	5	with
Step dealloying	50	25%	1	with
	Room temperature	25%	6	with

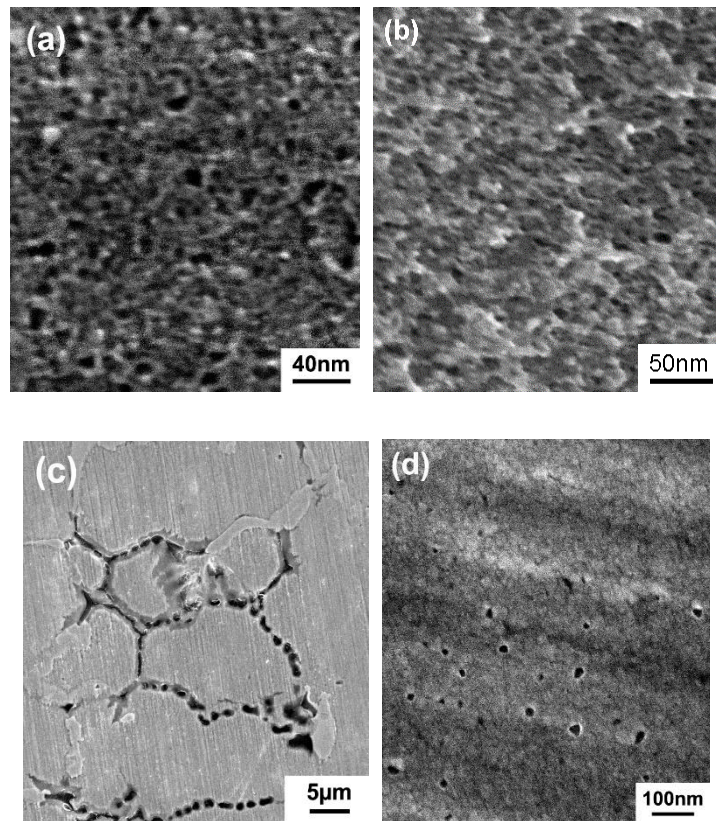


Figure 9.1 (a) dealloying in 25 °C H₂SO₄ for 5 days (b) dealloying in concentrated H₂SO₄ without surfactant at room temperature for 5 days (c) after 1st step dealloy in 25% H₂SO₄ at 50 °C for 1 day, pores along the grain boundary. (d) after 2nd step dealloying, the sample in (c) keep dealloying in 25% H₂SO₄ at room temperature for another 6 days

Electrochemical dealloying then applied as the free corrosion dealloying did not yield good np structure. A three-electrode system was used for dealloying, with Pt wire working as a counter electrode, a saturated Ag/AgCl electrode used as a reference electrode and the polished alloy piece carried by Ir wire holder serving as working electrode. The electrochemical dealloying was carried out in 0.1 mol/L H₂SO₄ electrolyte. Linear sweep was first conducted to the sample with a scan rate, 20mv/s, to

find out the critical potential. The electrochemical dealloying was then conducted on the sample at 0.2V, which was determined from the linear sweep result (Figure 9.2), for 18 hours until the current reached zero. After dealloying, the weight of the sample decreased from 0.0117g to 0.0034g indicating 70.94% weight loss. As shown in Figure 9.3 is the morphology of the samples after electrochemical dealloying. No np structure was observed from the top view image (Figure 9.3 (a)) and cracks were observed to form all over the surface and exist in the entire sample (Figure 9.3 (c)). The as dealloyed Pd sample was extremely brittle as implied by some surface region of the sample being broken (as marked with the white square in Figure 9.3 (a)). Figure 9.3 (b) is the close view of the structure in the white square in (a). Although the np structure did not present on the surface, it did yield np structure inside the sample as shown in Figure 9.3 (d) which is one spot in (b) under large magnification. The ligaments are contacted and the pores size is small. To improve the np structure and solve the cracking issue, the composition of precursor alloy was then adjusted to Pd₁₈Ni₈₂.

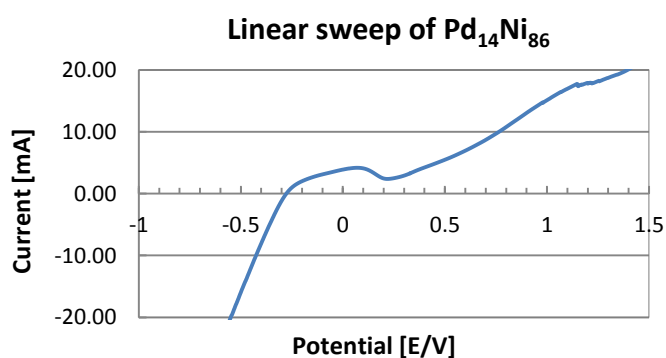


Figure 9.2 Linear sweep of Pd₁₄Ni₈₆

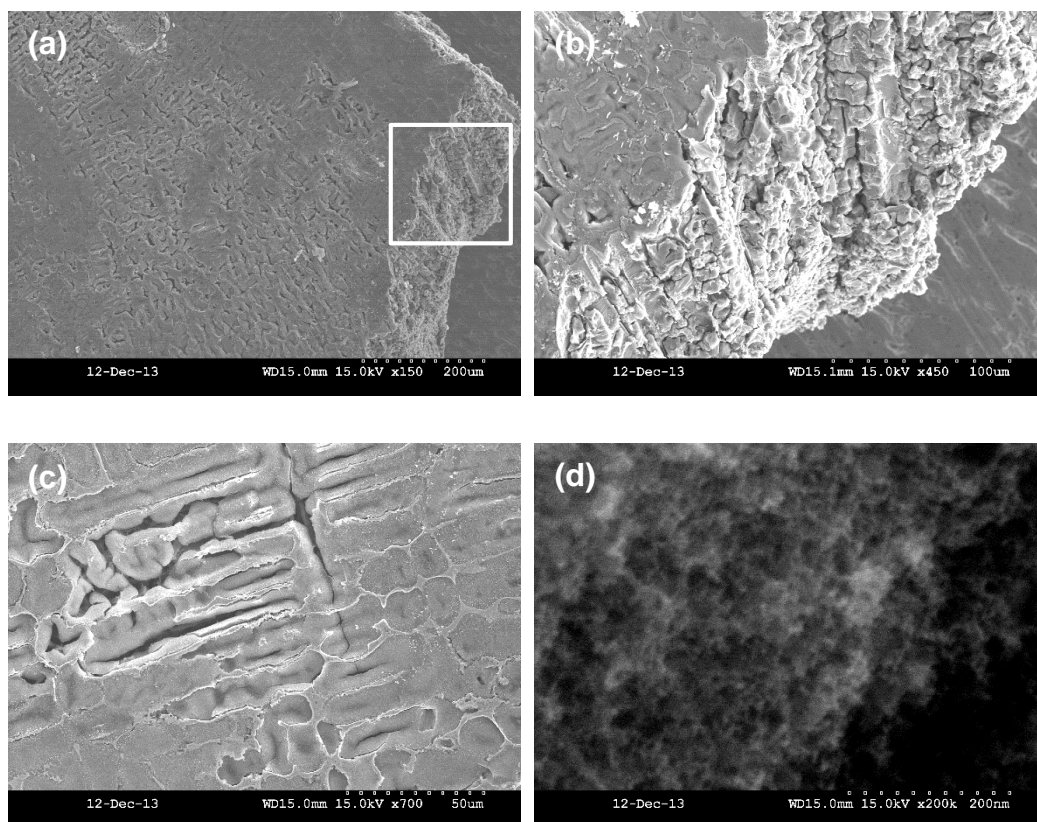


Figure 9.3 Morphology of bulk $\text{Pd}_{14}\text{Ni}_{86}$ after electrochemical dealloying (a) as dealloyed bulk $\text{Pd}_{14}\text{Ni}_{86}$ surface morphology, (b) the morphology inside the sample as indicated in the white in (a), (c) surface cracks, (d) zoom in one spot of (b) shows np-Pd structure

9.3.2 Microstructure study of np-Pd dealloyed from $\text{Pd}_{18}\text{Ni}_{82}$ precursor alloy

To adjust the composition of the PdNi precursor alloy that would yield best np-Pd structure, $\text{Pd}_{18}\text{Ni}_{82}$ alloy pellet was also arc melted. The linear sweep was conducted on both the Ir wire holder and the holder with polished $\text{Pd}_{18}\text{Ni}_{82}$ sample to find out the critical dealloying potential (Figure 9.4 (a)). The potential corresponding to the first lowest current drop on the $\text{Pd}_{18}\text{Ni}_{82}$ liner sweep, 50mV, was used as the electrochemical dealloying. The dealloying current reached zero after 15 hours of dealloying as shown

in the current density curve in Figure 9.4 (b).

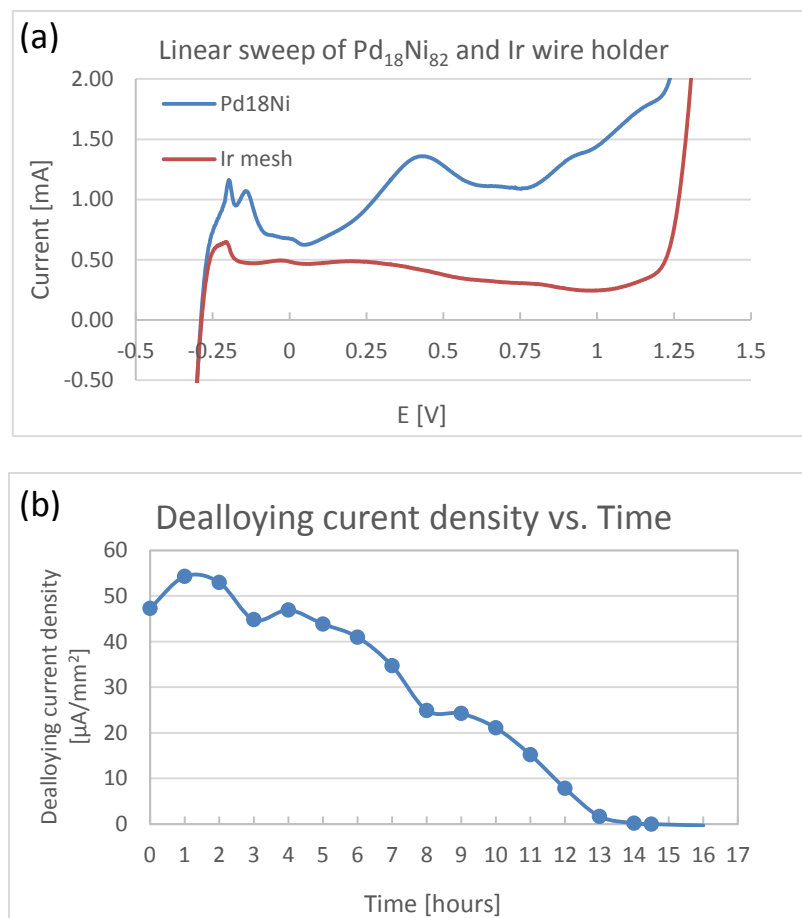


Figure 9.4 (a) Linear sweep of Pd₁₈Ni₈₂ and Ir wire holder (b) Dealloying current density evolution curve of Pd₁₈Ni₈₂

As shown in Figure 9.5 (a) and (b) cracks grew along the grain boundary both on the surface and inside the sample after dealloying. The sample thickness was $\sim 214\mu\text{m}$ before dealloying and $\sim 147\mu\text{m}$ (Figure 9.5 (c)) after dealloying, thus the thickness shrunk was $\sim 31\%$. The large volume shrinkage during dealloying was an obvious cause of the cracking, as well as the macro defects in the bulk sample. The measured mass before and after dealloying was 0.0082g and 0.0026g respectively, which indicates about 68% mass loss. From the plan view image, no np structure has been observed.

The cross section image Figure 9.5 (e) showing close to surface area, there is about 100 nm thick top dense layer. By EDS spot scan on both the top layer and inside the grain, it was confirmed that the dense top layer in Figure 9.5 (d) is Ni-rich. As shown by statistics of ligament size and pores size distribution in Figure 9.5 (f) and Figure 9.6, approximately 95% pores have size between 3-5nm, which is the smallest bulk nanoporous structured Pd that has never been reported. The average pore size is about 4.07 nm while the ligaments size is even smaller than previous np-Pd thin film. More than 35% of the ligaments are with the size ~5nm; 77% of the ligaments are about 5-7 nm. The ultrafine np-Pd would be a promising option for hydrogen storage and sensing as it provide more room for hydrogen swelling cycles and more contact area for increasing its sensitivity.

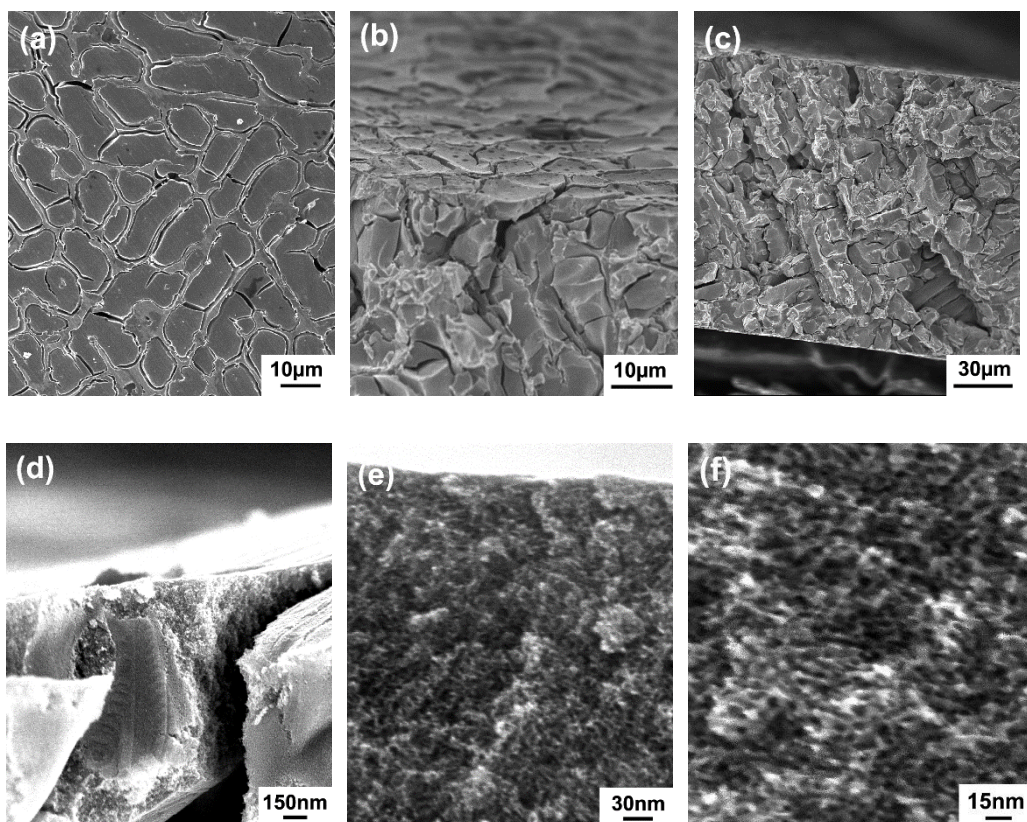


Figure 9.5 Morphology of the Pd₁₈Ni₈₂ after electrochemical dealloying for 14 hours

(a) plan view (b) cracks on the surface and inside the sample (c) cross section view (d) dense top layer and np structure at the broken region (e) cross section view with dense top layer (f) ultrafine np-Pd structure with pore size 3-5 nm

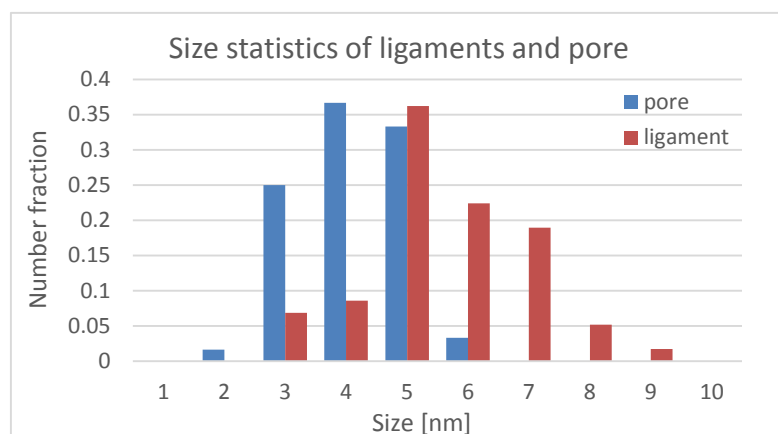


Figure 9.6 Size statistics of ligaments and pore

The back scattering electron (BSE) image of the as dealloyed np-Pd is shown in Figure 9.7. The PdNi alloy has the brunch rod structure and the Pd is rich in the grain boundary area as it is brighter in the BSE image. Even in the grain boundary, there are some dark region which indicates the as-arc melted sample is not homogeneous. Spot scan EDS was conducted on the as-melted sample and as-dealloyed sample as shown in Table 9.2. The composition was the average of three spot scan results. Inside the grain region that formed np-Pd structure after dealloying, the Pd content is about 13.52 at. % . The Pd is rich in the grain boundary region with a content 59.79 at. %. In the thin film form, the optimized composition to fabricate np-Pd is Pd 18% in the precursor alloy. When fabricate bulk PdNi sample the same composition was pursued as the optimized area scan composition. However, inside the bulk PdNi alloy, due to the brunch rod structure of Pd rich grain boundary, the optimized composition resulted in np-Pd was Pd_{13.5}Ni_{86.5} (within the grains) precursor alloy. Although the Pd-Ni alloy formed a continuous series of solid solutions over the entire composition and temperature range, a short range order has been reported [109] [110]. This rod like Pd rich structure was one of the main

reasons that caused the cracking during dealloying. the high Pd content, the grain boundary could not be dealloyed. The EDS spot scan on the surface of the as dealloyed sample indicated 45.84% residual Ni, which was due to the dense top layer showed in Figure 9.6. Inside the np-Pd region, the Pd content was up to 80%, which was close the residual Ni in np-Pd thin films.

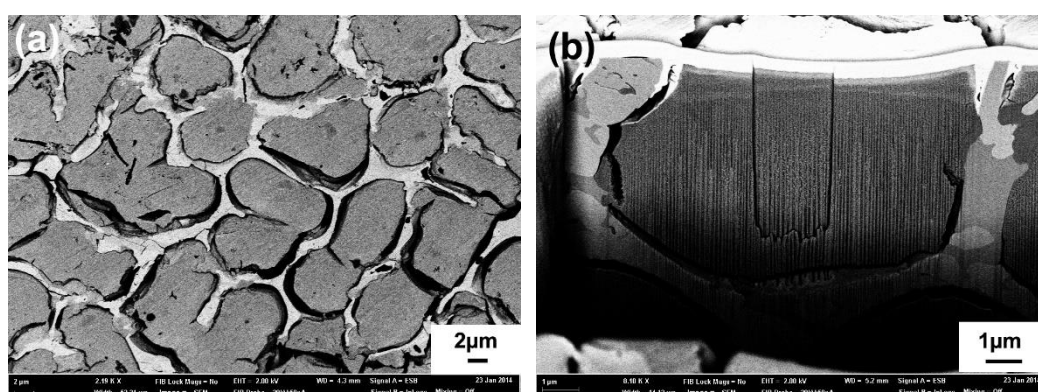


Figure 9.7 BSE image of as dealloyed np-Pd (a) surface morphology (b) inside grain structure imaged by cutting a slot on the sample by FIB

Table 9.2 EDS spot scan result on the top layer of as-melted and as-dealloyed PdNi alloy

Elements	Before dealloying (at.%)		After dealloying (at.%)	
	Inside the grain	Grain boundary	Inside the grain	Grain boundary
Pd	13.52	59.79	54.16	64.37
Ni	86.48	40.23	45.84	35.63

XRD has been applied on the as arc-melted Pd₁₈Ni₈₂ sample. Ni and Pd are both fcc structure, Ni has a lattice parameter ‘a’ as 3.5239 while Pd has a lattice parameter ‘a’ as 3.8908. As shown in Figure 9.8 and Table 9.3, the XRD scan result is shows 2θ of the peaks. Theas measured 2θ of peaks, 44.06, 51.17, 75.48 and 91.35, are close to the Ni’s

[111], [200], [220] and [311] but all shifted to a higher angle. In the crystalline phases and/or crystal structure peaks to higher values of the diffraction angle, this means that the lattice parameter is decreasing.

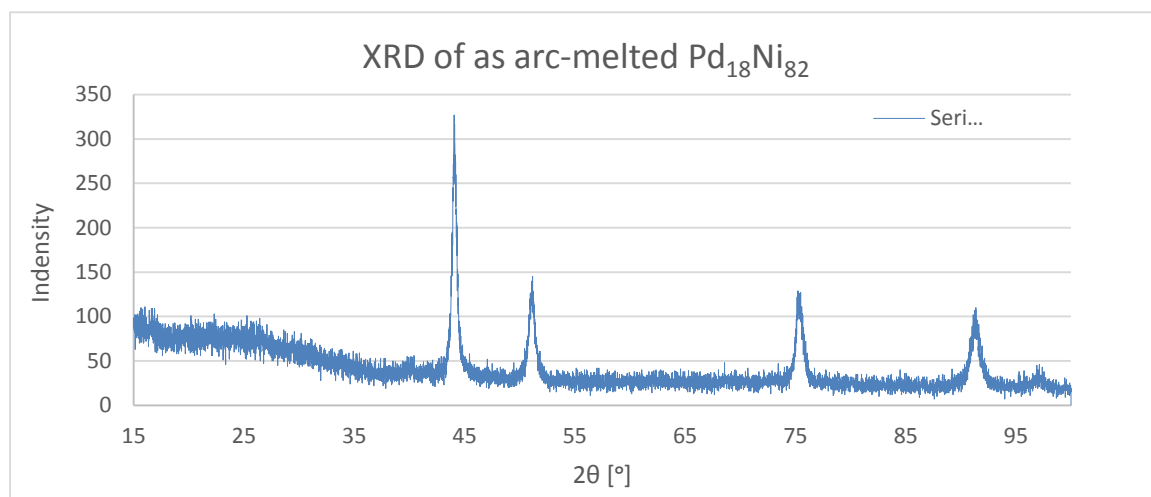


Figure 9.8 XRD scan result of as arc melted Pd₁₈Ni₈₂ alloy

Table 9.3 XRD parameters and scan results of Ni, Pd and PdNi alloy

Pd 2θ/°		Ni 2θ /°		Peaks 2θ/°	Shift between Ni's 2θ /° and peaks' 2θ /°
Pd 111	40.10	Ni 111	44.48	44.06	0.42
Pd 200	46.63	Ni 200	51.83	51.17	0.66
Pd 220	68.08	Ni 220	76.35	75.48	0.87
Pd 311	82.05	Ni 311	92.89	91.35	1.54

In order to reduce the cracks, annealing was conducted on the sample to uniform the composition distribution through the sample and enlarge the grain size to reduce the effect of the grain boundary. Arc melted sample was annealed at 1000 °C for 24 hours under Ar gas then slowly cooled down in Ar. The optical microstructure of the Pd₁₈Ni₈₂ sample before and after annealing are showing in Figure 9.9. After annealing, the as cast dendrites transferred to fully annealed and enlarged grains, showing the

homogenization was correctly processed at least from optical microstructure and thus the elemental distribution should have been better (more uniformly) than the as cast status. The grain reached the level of hundreds of micrometers.

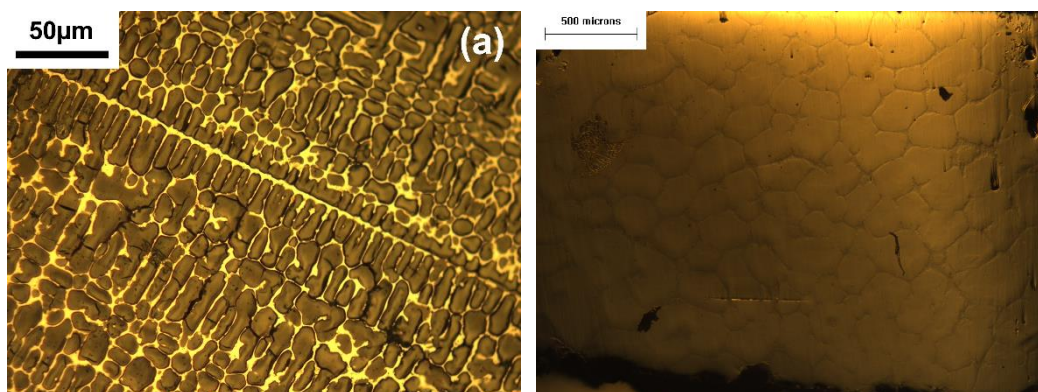


Figure 9.9 The optical microstructure of the Pd₁₈Ni₈₂ sample before and after annealing are showing in (a) before annealing (b) after annealing

The electrochemical dealloying that carried out on the as annealed Pd₁₈Ni₈₂ sample was under 250mV for 24 hours which results in 72% weight loss. The optical microstructure of as annealed Pd₁₈Ni₈₂ sample before and after dealloying are shown in Figure 9.10. As the result from EDS spot scan on both the dark boundary area and the bright area in Figure 9.7 (a), the cluster net structure is Pd rich rod. The as dealloyed sample was cracked and extremely brittle. Although the sample shrunk about 30% in the thickness, as shown in Figure 9.10 (a) and (c), the sample's size did not have notable changes from the 2D dimension.

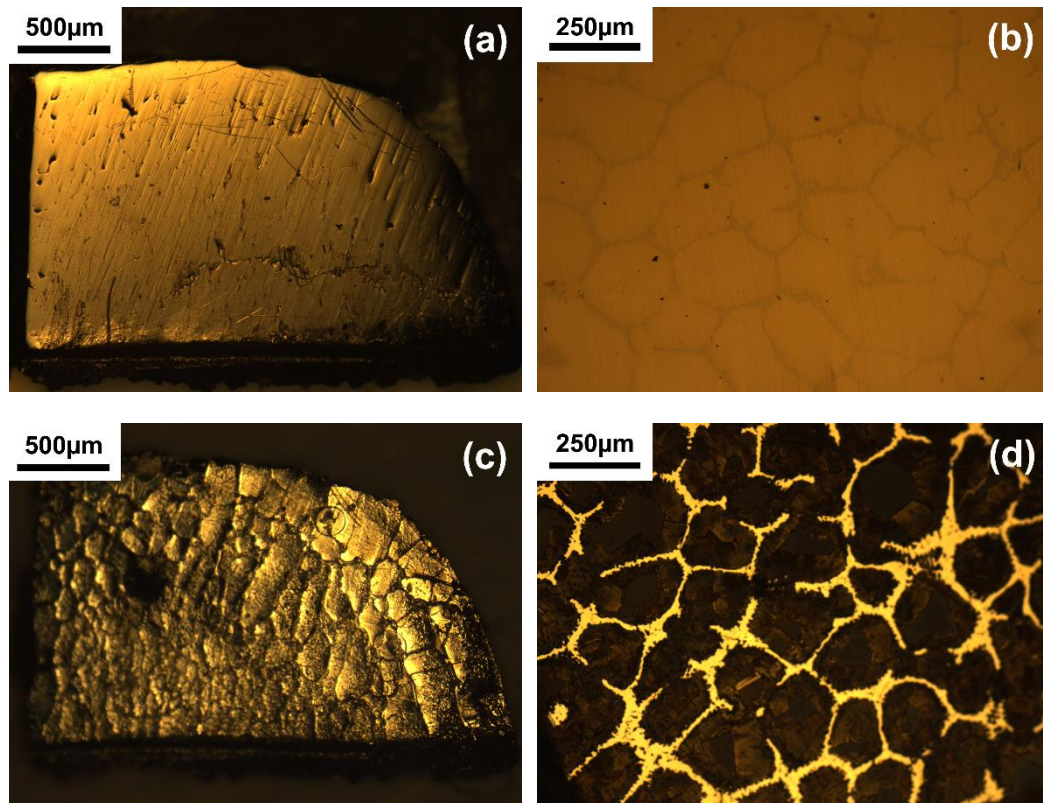


Figure 9.10 (a) and (b) optical microstructure of the as annealed $\text{Pd}_{18}\text{Ni}_{82}$ before dealloying, (c) and (d) are after dealloying

The structure of the as dealloyed np-Pd are shown in Figure 9.11. The top surface does present np structure as shown in Figure 9.11 (a). However, as in Figure 9.11 (b), it has very promising np structure inside the sample. The pore size is as small as 2-3 nm which is the smallest bulk np-Pd pore size that has never been reported. The ultra-fine np structure spreads all over the entire sample. After annealing, the grain boundary still cracks, however, the grain size grows ten times compare with the sample before annealing, less cracks inside the grain and in the whole sample as shown in Figure 9.11 (d).

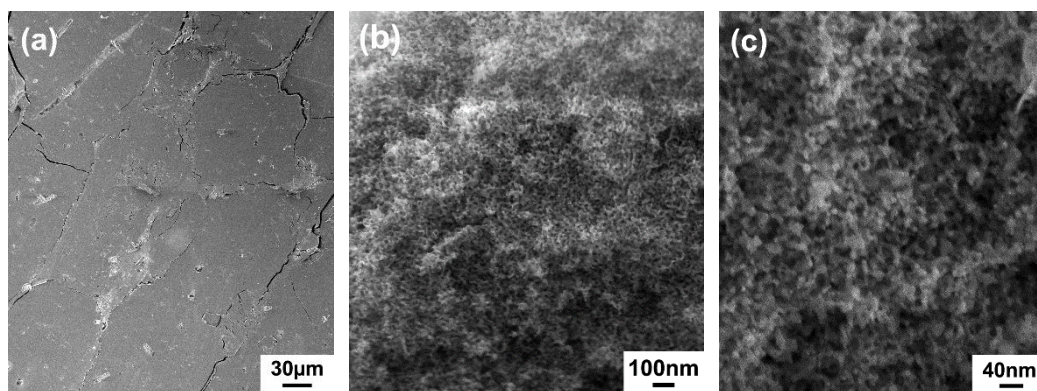


Figure 9.11 Morphology of the as annealed Pd₁₈Ni₈₂ after electrochemical dealloying under different magnification

9.3.3 Microstructure study of np-Pd dealloyed from Pd₂₀Co₈₀ precursor alloy

Owing to the cracking issue of dealloying PdNi alloy, Co was also selected as the sacrificial element in the Pd alloy system to fabricate the np-Pd. The linear sweep was also applied to search for the critical dealloying potential. Electrochemical dealloy was carried out under 200mV until the dealloying current decreased to zero. The as fabricated Pd₂₀Co₈₀ has grain sizes around 20-40 μm. Although the micro structure did not have the Pd rich cluster structure, large amount of cracks were presented over the whole sample that dealloyed from Pd₂₀Co₈₀ alloy (Figure 9.12 (a)). Besides the cracks, the as dealloyed bulk np-PdCo has uniform and continuous np structure. The pore size is around 7-10 nm as shown in Figure 9.12 (b) and (c), which is larger than the np-Pd dealloyed from Pd₁₈Ni₈₂.

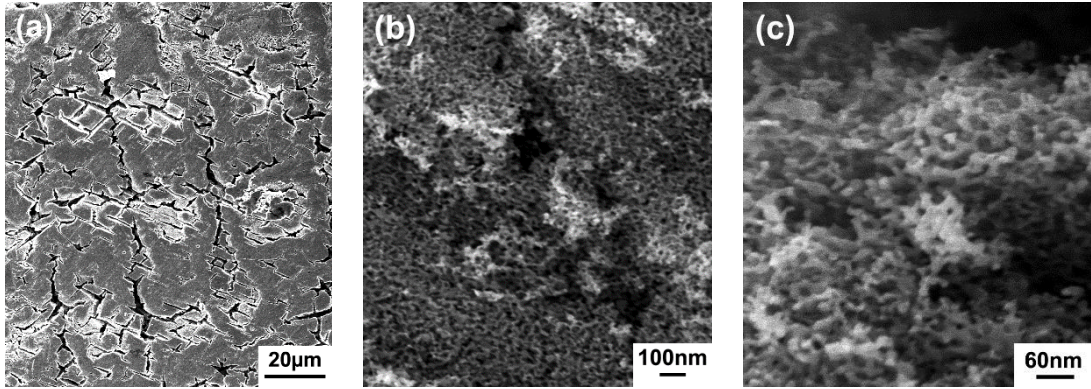


Figure 9.12 Morphology of as dealloyed Pd₂₀Co₈₀ alloy under different magnification

9.3.4 Micro-pillar compression test of bulk np-Pd

The np-Pd electrochemically dealloyed from Pd₁₈Ni₈₂ was milled using a focused ion beam, as shown in Figure 9.13, to create micron-scale pillars for compression testing in the TEM. The sample was thinned to a slice/wedge 40-50 microns thick, the columns were then milled near the edge/tip. The cracks that penetrated the sample are clearly shown in the cross section image after milling into the sample.

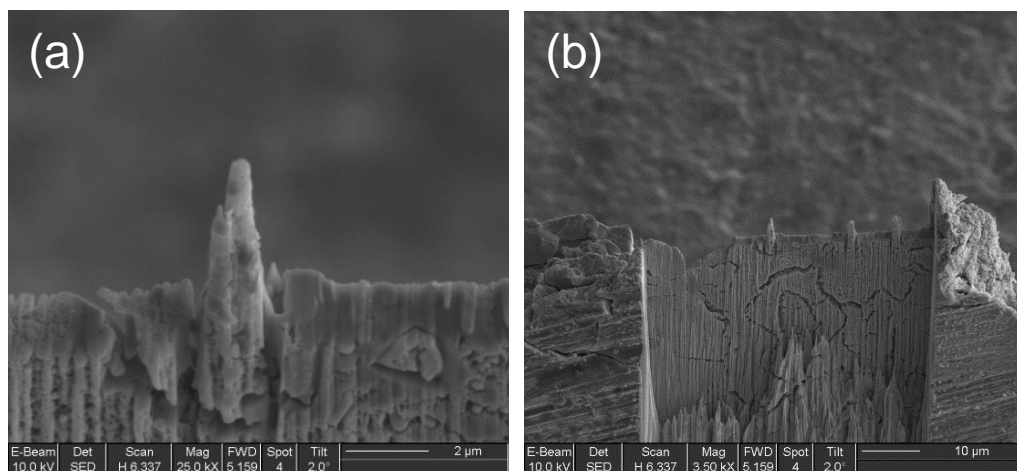


Figure 9.13 Np-Pd pillar (a) a single pillar, and (b) cross section image after FIB.

The load displacement curve, load vs. time curve and displacement vs. time curve are

shown in Figure 9.14. Additionally, images captured during the indentation experiment are shown in Figure 9.15. The as measured pillar geometry had a height of 1 μm and diameter of 0.62 μm . The maximum indentation depth was $\sim 0.45 \mu\text{m}$, corresponding to $\sim 44\%$ deformation. Although the bulk np-Pd is very brittle on a macroscopic scale, the np-Pd pillar did not break during indentation. Instead, the pillar became denser after indentation, as shown in Figure 9.15 (d). During the removal of load, the np-Pd pillar recovered $\sim 22\%$ of its original height. The final height of the pillar was $\sim 0.88 \mu\text{m}$ after unloading. The post-compression recovery may also be due to adhesion between the pillar and indenter during the beginning of unloading. After indentation, the top of the pillar was compacted instead of fractured. The stress-strain curve is shown in Figure 9.16, indicating a compressive yield stress of $\sim 105 \text{MPa}$ for np-Pd. As shown in the enlarged view in Figure 9.16, the yield strain is $\sim 7.3\%$. Linear fitting of the stress strain curve indicates a Young's modulus of $\sim 1.5 \text{GPa}$.

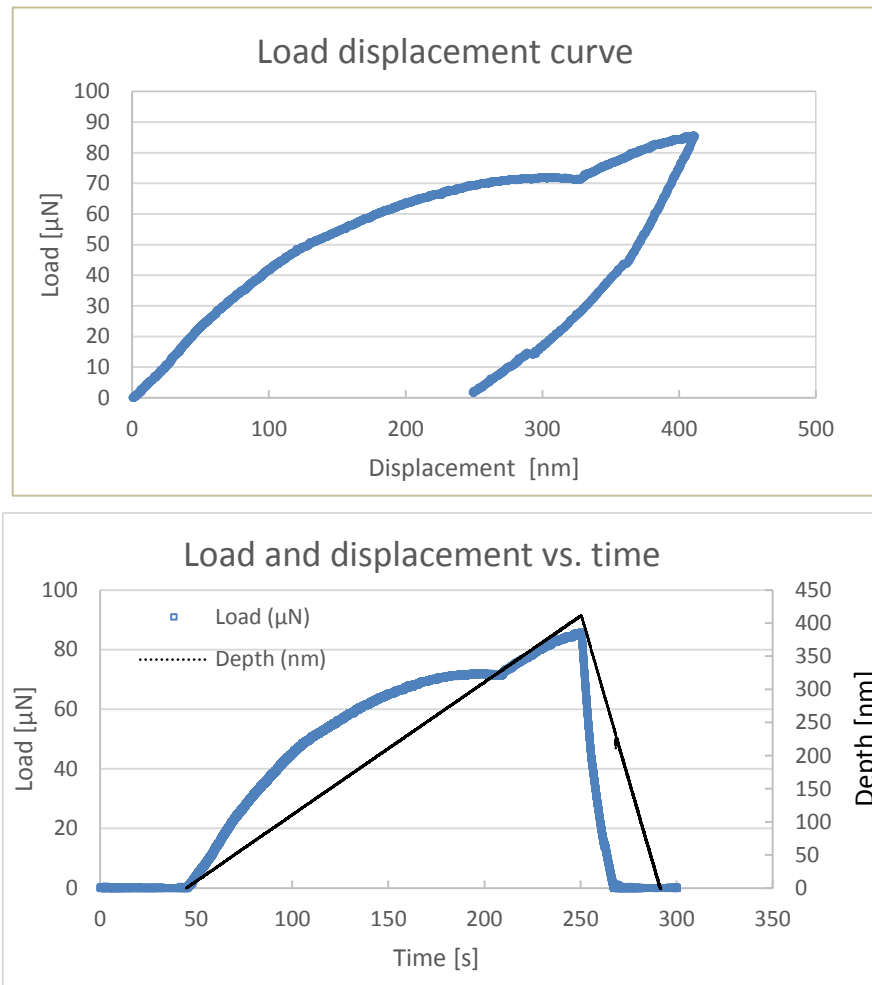


Figure 9.14 Plots of (a) load vs. displacement and (b) load/displacement versus time.

The increase in load near the end of the test (above 70 μN load) is due to contact of the indenter tip with material surrounding the micro-pillar, and is therefore not indicative of sample behavior.

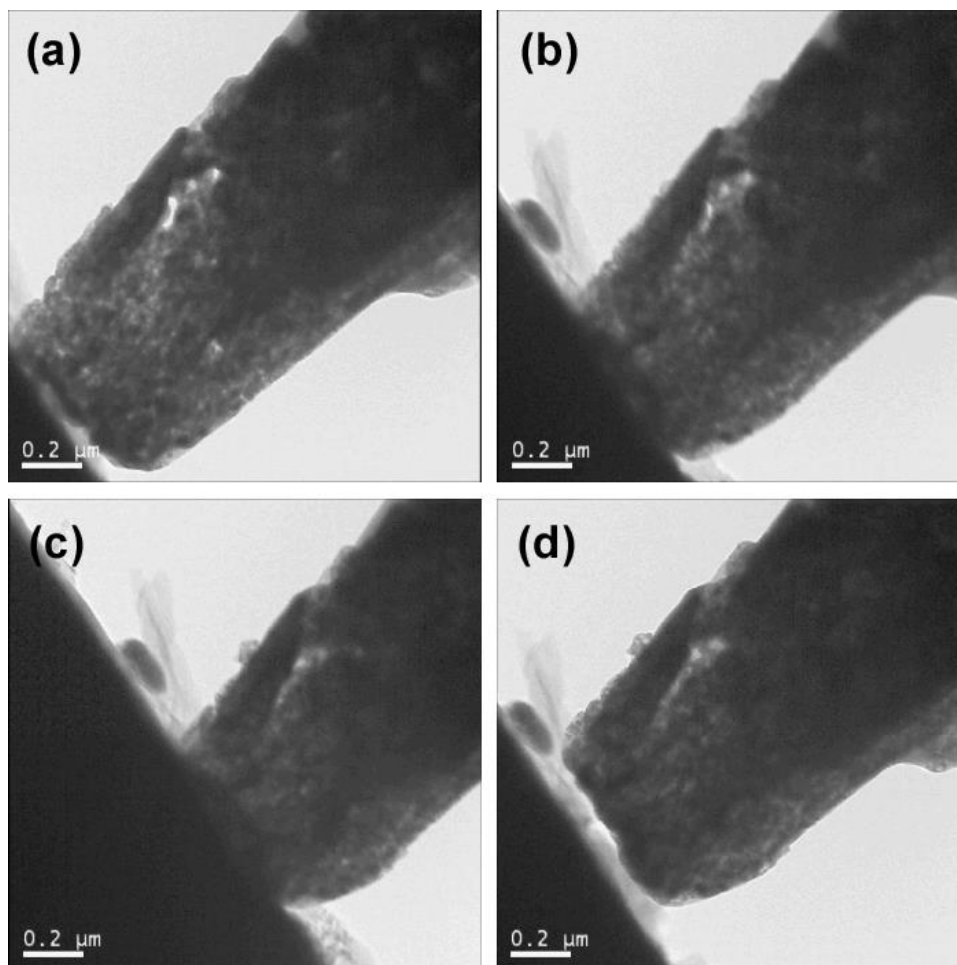


Figure 9.15 In-situ indentation test of np-Pd pillar (a) before indentation (b) indenter contact with the pillar (c) the max deformation point (d) after indentation.

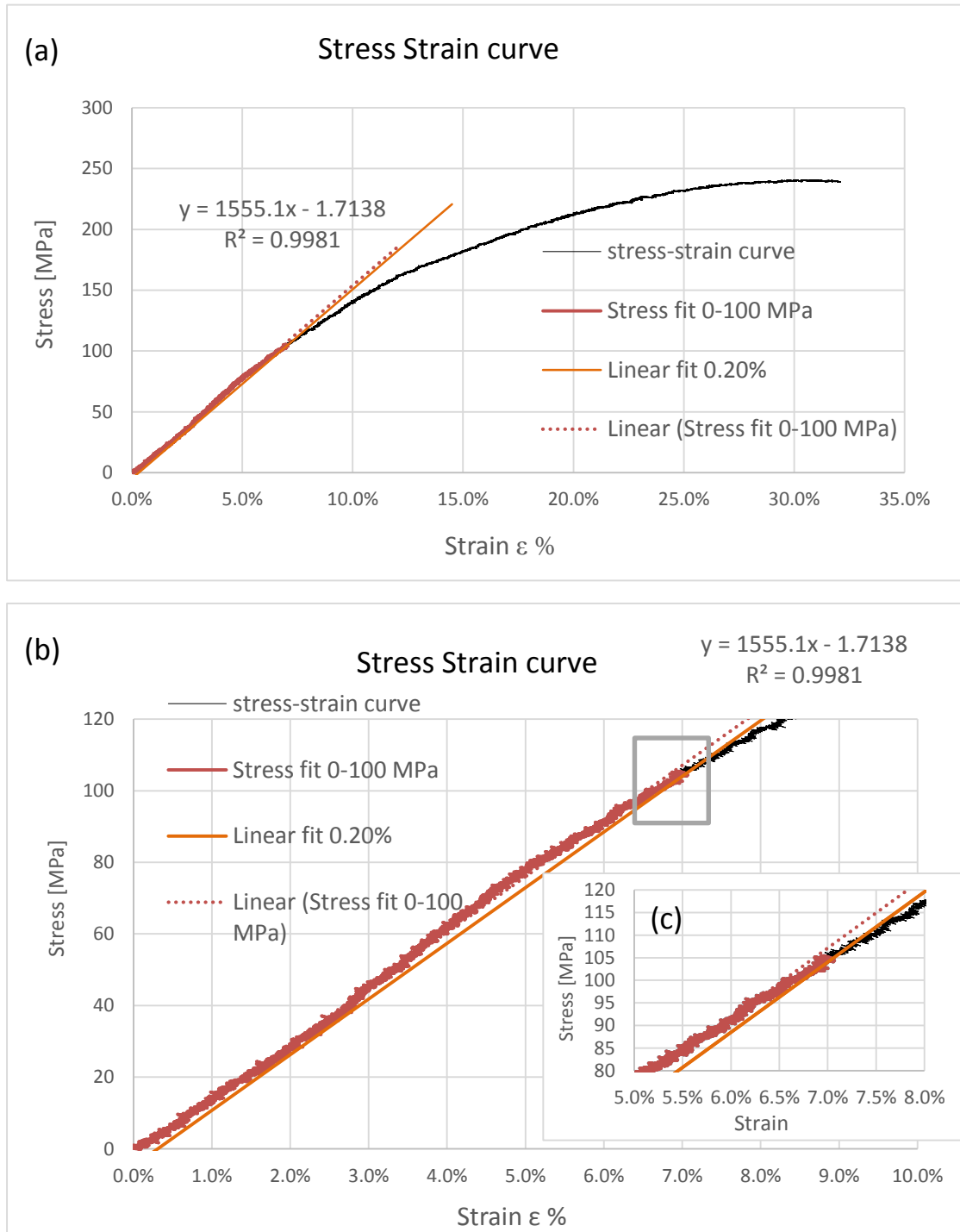


Figure 9.16 (a) Stress-Strain curve of np-Pd micro-pillar, (b) and (c) with a detailed showing the loading section from which elastic modulus was measured.

9.4 Summary

The optimized composition of precursor PdNi alloy that yields the best np structure after dealloying and the proper dealloying procured resulted in the finest pore size has been developed in the research of this chapter. The ultra-fine np-Pd has been successfully fabricated by electrochemically dealloying the as annealed Pd₁₈Ni₈₂ sample. The pore size of the as fabricated np-Pd is as small as 3-5 nm which has never been achieved before. The as presented ultra-fine nano structure has much more surface than previous np-Pd which provides remarkable potential of serving as a hydrogen storage material. However, although the annealing helps to grow the grain tens time, the crack issue along the grain boundary is still the vital problem. The mechanical behavior of the as fabricated bulk np-Pd has been tested by in-situ indentation. Although the entire sample is extremely brittle, the ligaments structured np-Pd compressed in to denser structure instead of break down after indentation. And it has the ability to recover its deformation like a sponge. For the future work, single crystal of Pd could be made by the Bridgman technique to avoid the cracking along the grain boundary. The in-situ indentation work carry out on none cracked sample would provide more accurate detailed results of the mechanical behavior of the bulk np-Pd.

Chapter 10. Conclusions and future work

10.1 Conclusion remarks

In this doctoral research work, two nanoporous alloy system np-Si and np-Pd have been studied. A novel method to fabricated np-Si using distilled water has been developed and the properties of the np-Si have been studied by various microscopic observation. The as fabricated np-Si served as the negative electrode in LIB in the experiments and exhibited very promising specific capacity. As well, the mechanical behavior of the np-Si has been studied by in-situ TEM compression test. For the np-Pd thin film, the hydridation and dehydridation behavior has been studied, in which it demonstrated that the multilayered np-Pd provided a possibility to manipulate the np structure of np-Pd films. The bulk np-Pd with ultra-fine pores and ligaments have been developed and the mechanical behavior of the bulk np-Pd has been studied by in-situ pillar compression test.

The key findings of this doctoral research are drawn as follows:

1. Np-Si has been successfully fabricated by dealloying the as deposited Si-Mg precursor thin film. The optimized composition of Si-Mg alloy film of is $\text{Si}_{53}\text{Mg}_{47}$ and the best dealloying method has been developed. Instead of the high concentration acid or HF that has usually been used to fabricated porous Si, the dealloying etchant in this method is distilled water, which is totally environment friendly.

2. The as-fabricated np-Si presents an open np structure with the ligament size ~20-30 nm. The as-dealloyed np-Si thin film is pure amorphous Si film and the amorphous film could be crystallized by annealing in vacuum at certain temperature.
3. The as-dealloyed np-Si thin film that has been tested as an anode in LIB with electrochemical battery testing. The specific capacity of the as fabricated LIB has achieved ~2000mAh/g. Different interlayers and film thickness have noticeable effect on the behave of the cell cycling performance and the capacity of the as tested LIB.
4. The mechanical behavior of the as fabricated amorphous np-Si has been studied by in-situ TEM indentation. The as dealloyed np-Si thin film exhibited a sponge-like behavior in in-situ nanoindentation test. Thickness of the np-Si thin film could be fully recovered after the indenter removed from the film under particularly strain. The maximum deformation in thickness was up to 30%.
5. The hydridation and dehydridation behavior of the np-Pd film with the ligaments size around 5~7nm has been investigated by monitoring the stress changing in the film during the absorption and desorption process. The as fabricated porous Pd film exhibited high sensitivity to low concentration H₂ gas.
6. Multilayer np-Pd thin film has been developed. The as dealloyed film presented layered architecture with periodic cells and ordered ligaments layers throughout the whole film. The bridge ligaments between the layers oriented vertically to the bounding layers. The pores and ligaments size could be controlled by tuning

the thickness of the PdNi alloy layer and the separation Pd layer.

7. The ultra-fine bulk np-Pd has been successfully fabricated by proper electrochemically dealloying the annealed arc-melted Pd₁₈Ni₈₂ sample. The unprecedented ultra-fine np-Pd presents as small as 3 nm ligaments. The ultra-fine ligaments and pores dramatically increased the surface area which provides remarkable potential of serving as a hydrogen storage material.
8. The np structured bulk np-Pd was test by in-situ pillar compression test. The pillar was compassed in to denser structure after indentation instead of breaking down which was unanticipated considered the extremely brittle character of the as fabricated bulk np-Pd.

10.2 Suggestion for future work

There are still more research work needs to be conducted on the related field of np-Si and np-Pd in the future.

The effective mass of np-Si on the electrode, which is important for the battery cycling current and specific capacity, is subjected to be exactly measured or calculated. The macro cracking issue due to the Cu foil substrate machining defect needs to be solved. The np-Si thin film which could allow the relaxation of the strain and stress during the volume expansion/ contraction with the lithiation/ delithiation for LIB will be further developed in the future.

The properties difference, such as the mechanical behavior, between the as dealloyed amorphous and as annealed nanocrystalline np-Si the of the np-Si thin film will also

need to be studied in the future.

Inspired by the multilayer np-Pd film, multilayer np-Si film could be fabricated in the further study. By manipulating the alloy / pure metal thickness, the desired np-Si structure made from the total environment friendly method with targeted ligaments and pore size would be able to promote the development of Si in LIB, photonics, biological imaging, sensors, drug delivery and energy storage field in future.

The np-Pd thin film and bulk np-Pd would be promising to be used as the hydrogen sensing materials in the future. The ultra-fine ligaments and pores dramatically increased the surface area which provides remarkable potential of serving as a hydrogen sensor or storage material.

For the future work, film with more layers should be explored to study the thickness effect of the alloy and separation layer on the final layered np structure. By adjusting thickens ratio of the alloy and pure element, the pore and ligaments size could be manipulated. Desired np structured Pd could be fabricated for sensing and storage application.

For the future work of bulk Pd, more careful controlled dealloying procedure could be investigated to reduce the formation of cracks during dealloying. Low potential electrochemical dealloying at elevated temperature or multistep free corrosion plus electrochemical dealloying would be attempted to achieve reduction in crack formation. A better understanding of the dealloying process and the volume shrinkage mechanisms would be studied.

For the future work, single crystal of Pd could be made by the Bridgman technique to avoid the cracking along the grain boundary. Bulk np-Pd pillar would be fabricated from dealloying single crystalline bulk PdNi alloy sample, to be meet the crack free requirement of the micro-pillar compression test. The in-situ indentation work carry out on none cracked sample would provide more accurate detailed results of the mechanical behavior of the bulk np-Pd.

Reference

- [1] R. E. Morris and P. S. Wheatley, "Gas storage in nanoporous materials," *Angewandte Chemie-International Edition*, vol. 47, pp. 4966-4981, 2008.
- [2] Y. G. Guo, J. S. Hu, and L. J. Wan, "Nanostructured Materials for Electrochemical Energy Conversion and Storage Devices (vol 20, pg 2878, 2008)," *Advanced Materials*, vol. 20, pp. 4384-4384, Dec 2 2008.
- [3] W. W. Ji-Guang Zhang, Jie Xiao, Wu Xu, Gordon L. Graff, Gary Yang, Daiwon Choi, Deyu Wang, Xiaolin Li, Jun Liu, *Batteries for Sustainability*: Springer New York, 2013.
- [4] L. L. Luo, J. S. Wu, J. Y. Luo, J. X. Huang, and V. P. Dravid, "Dynamics of Electrochemical Lithiation/Delithiation of Graphene-Encapsulated Silicon Nanoparticles Studied by In-situ TEM," *Scientific Reports*, vol. 4, Jan 24 2014.
- [5] D. L. Ma, Z. Y. Cao, and A. M. Hu, "Si-Based Anode Materials for Li-Ion Batteries: A Mini Review," *Nano-Micro Letters*, vol. 6, pp. 347-358, Oct 2014.
- [6] S. Goriparti, E. Miele, F. De Angelis, E. Di Fabrizio, R. P. Zaccaria, and C. Capiglia, "Review on recent progress of nanostructured anode materials for Li-ion batteries," *Journal of Power Sources*, vol. 257, pp. 421-443, Jul 1 2014.
- [7] T. Hubert, L. Boon-Brett, G. Black, and U. Banach, "Hydrogen sensors - A review," *Sensors and Actuators B-Chemical*, vol. 157, pp. 329-352, Oct 20 2011.
- [8] T. B. Flanagan and W. A. Oates, "The Palladium-Hydrogen System," *Annual Review of Materials Science*, vol. 21, pp. 269-304, 1991.
- [9] P. Tripodi, N. Armanet, V. Asarisi, A. Avveduto, A. Marmigi, J. P. Biberian, *et al.*, "The effect of hydrogen stoichiometry on palladium strain and resistivity," *Physics Letters A*, vol. 373, pp. 4301-4306, Nov 23 2009.
- [10] (1995). *HANDBOOK OF BATTERIES*.
- [11] J. Chen and F. Y. Cheng, "Combination of Lightweight Elements and Nanostructured Materials for Batteries," *Accounts of Chemical Research*, vol. 42, pp. 713-723, Jun 2009.
- [12] B. S. Walter A. van Schalkwijk, *Advances in Lithium-Ion Batteries*, 2002.
- [13] J. M. Tarascon and M. Armand, "Issues and challenges facing rechargeable lithium batteries," *Nature*, vol. 414, pp. 359-367, Nov 15 2001.
- [14] M. N. Obrovac and L. J. Krause, "Reversible cycling of crystalline silicon powder," *Journal of the Electrochemical Society*, vol. 154, pp. A103-A108, 2007.
- [15] J. Cho, "Porous Si anode materials for lithium rechargeable batteries," *Journal of Materials Chemistry*, vol. 20, pp. 4009-4014, 2010.
- [16] J. R. Szech and S. Jin, "Nanostructured silicon for high capacity lithium battery anodes," *Energy & Environmental Science*, vol. 4, pp. 56-72, Jan 2011.
- [17] R. A. Huggins and W. D. Nix, "Decrepitation Model For Capacity Loss During Cycling of Alloys in Rechargeable Electrochemical Systems," *Ionics*, vol. 6, pp. 57-63, Jan 2000.
- [18] V. A. Sethuraman, K. Kowolik, and V. Srinivasan, "Increased cycling efficiency and rate capability of copper-coated silicon anodes in lithium-ion batteries," *Journal of Power Sources*,

- vol. 196, pp. 393-398, Jan 1 2011.
- [19] H. Okamoto, "Section iii Supplemental Literature Review," *ASM International*, vol. 30, p. 2, 2009.
 - [20] R. A. Huggins. (2009). *Advanced Batteries*.
 - [21] C. K. Chan, H. L. Peng, G. Liu, K. McIlwrath, X. F. Zhang, R. A. Huggins, *et al.*, "High-performance lithium battery anodes using silicon nanowires," *Nature Nanotechnology*, vol. 3, pp. 31-35, Jan 2008.
 - [22] V. L. Chevrier, J. W. Zwanziger, and J. R. Dahn, "First principles study of Li-Si crystalline phases: Charge transfer, electronic structure, and lattice vibrations," *Journal of Alloys and Compounds*, vol. 496, pp. 25-36, Apr 30 2010.
 - [23] M. Holzapfel, H. Buqa, W. Scheifele, P. Novak, and F. M. Petrat, "A new type of nano-sized silicon/carbon composite electrode for reversible lithium insertion," *Chemical Communications*, pp. 1566-1568, 2005.
 - [24] G. C. Hui Wu, Jang Wook Choi, "Six Thousand Electrochemical Cycles of Double-Walled Silicon Nanotube Anodes for Lithium Ion Batteries " *SLAC-PUB-14379*, 2011.
 - [25] J. P. Maranchi, A. F. Hepp, A. G. Evans, N. T. Nuhfer, and P. N. Kumta, "Interfacial properties of the a-Si/Cu : active-inactive thin-film anode system for lithium-ion batteries," *Journal of the Electrochemical Society*, vol. 153, pp. A1246-A1253, 2006.
 - [26] J. C. Li, A. K. Dozier, Y. C. Li, F. Q. Yang, and Y. T. Cheng, "Crack Pattern Formation in Thin Film Lithium-Ion Battery Electrodes," *Journal of the Electrochemical Society*, vol. 158, pp. A689-A694, 2011.
 - [27] C. M. Park, J. H. Kim, H. Kim, and H. J. Sohn, "Li-alloy based anode materials for Li secondary batteries," *Chemical Society Reviews*, vol. 39, pp. 3115-3141, 2010.
 - [28] H. J. Ahn, Y. S. Kim, K. W. Park, and T. Y. Seong, "Use of Sn-Si nanocomposite electrodes for Li rechargeable batteries," *Chemical Communications*, pp. 43-45, 2005.
 - [29] M. H. Park, M. G. Kim, J. Joo, K. Kim, J. Kim, S. Ahn, *et al.*, "Silicon Nanotube Battery Anodes," *Nano Letters*, vol. 9, pp. 3844-3847, Nov 2009.
 - [30] C. Y. Du, C. H. Gao, G. P. Yin, M. Chen, and L. Wang, "Facile fabrication of a nanoporous silicon electrode with superior stability for lithium ion batteries," *Energy & Environmental Science*, vol. 4, pp. 1037-1042, Mar 2011.
 - [31] Z. F. Wei Chen, Abirami Dhanabalan,, "Mesoporous Silicon Anodes Prepared by Magnesiothermic Reduction for Lithium Ion Batteries," *The Electrochemical Society*, vol. 158(9), p. 5, 2011.
 - [32] G. W. Crabtree, M. S. Dresselhaus, and M. V. Buchanan, "The hydrogen economy," *Physics Today*, vol. 57, pp. 39-44, Dec 2004.
 - [33] T. K. N. Youngho Kim*, Wook Jang**, and Yong Wook Lee* "Optical Fiber Hydrogen Sensor based on Polarization-Maintaining Fiber Coated with Palladium " presented at the 2012 17th Opto-Electronics and Communications Conference, 2012.
 - [34] R. J. W. Cédric Perrotton, Nicolas Javahiraly, "A reliable, sensitive and fast optical fiber hydrogen sensor based on surface plasmon resonance," *OPTICS EXPRESS*, vol. 21, p. 9, 2013.
 - [35] J. Paillier and L. Roue, "Nanostructured palladium thin films prepared by pulsed laser deposition - Structural characterizations and hydrogen electro sorption properties," *Journal of the Electrochemical Society*, vol. 152, pp. E1-E8, 2005.

- [36] Y. Yürüm, *Hydrogen Energy System: Production and Utilization of Hydrogen and Future Aspects*, illustrated ed.: Springer Science & Business Media, 1995.
- [37] A. Pundt and R. Kirchheim, "Hydrogen in metals: Microstructural aspects," *Annual Review of Materials Research*, vol. 36, pp. 555-608, 2006.
- [38] A. S.-M. F.D. Manchester, and J.M. Pitre "The H-Pd (Hydrogen-Palladium) System " *Phase Equilibria*, vol. 15, p. 22, 1994.
- [39] M. Hakamada, H. Nakano, T. Furukawa, M. Takahashi, and M. Mabuchi, "Hydrogen Storage Properties of Nanoporous Palladium Fabricated by Dealloying," *Journal of Physical Chemistry C*, vol. 114, pp. 868-873, Jan 21 2010.
- [40] Y. I. Chou, C. M. Chen, W. C. Liu, and H. I. Chen, "A new Pd-InP Schottky hydrogen sensor fabricated by electrophoretic deposition with Pd nanoparticles," *Ieee Electron Device Letters*, vol. 26, pp. 62-65, Feb 2005.
- [41] F. Yang, D. K. Taggart, and R. M. Penner, "Fast, Sensitive Hydrogen Gas Detection Using Single Palladium Nanowires That Resist Fracture," *Nano Letters*, vol. 9, pp. 2177-2182, May 2009.
- [42] J. Villatoro and D. Monzon-Hernandez, "Fast detection of hydrogen with nano fiber tapers coated with ultra thin palladium layers," *Optics Express*, vol. 13, pp. 5087-5092, Jun 27 2005.
- [43] L. Z. A. Zaluska, J.O. Ström-Olsen*, "Structure, catalysis and atomic reactions on the nano-scale: a systematic approach to metal hydrides for hydrogen storage," *Appl. Phys. A*, vol. 72, p. 8, 2001.
- [44] L. J. T. J. A. Eastman, and B. J. Kestel, "Narrowing of the palladium-hydrogen miscibility gap in nanocrystalline palladium," *PHYSICAL REVIEW B*, vol. 48, p. 10, 1993.
- [45] A. Abburi and W. J. Yeh, "Temperature and Pore Size Dependence on the Sensitivity of a Hydrogen Sensor Based on Nanoporous Platinum Thin Films," *Ieee Sensors Journal*, vol. 12, pp. 2625-2629, Aug 2012.
- [46] S. Mubeen, T. Zhang, B. Yoo, M. A. Deshusses, and N. V. Myung, "Palladium nanoparticles decorated single-walled carbon nanotube hydrogen sensor," *Journal of Physical Chemistry C*, vol. 111, pp. 6321-6327, May 3 2007.
- [47] Z. C. Dongyan Ding, Chi Lu, "Hydrogen sensing of nanoporous palladium films supported by anodic aluminum oxides," *Sensors and Actuators B: Chemical*, vol. 120, p. 4, 2006.
- [48] M. K. Kumar, M. S. R. Rao, and S. Ramaprabhu, "Structural, morphological and hydrogen sensing studies on pulsed laser deposited nanostructured palladium thin films," *Journal of Physics D-Applied Physics*, vol. 39, pp. 2791-2795, Jul 7 2006.
- [49] J. M. L. a. W. L. Jin-Seo Noh, "Low-Dimensional Palladium Nanostructures for Fast and Reliable Hydrogen Gas Detection," *sensors*, p. 26, 2011.
- [50] A. M. H. Juergen Biener, Alex V. Hamza. (2007). *Deformation behavior of nanoporous metals*.
- [51] J. C. M. L. Fuqian Yang, *Micro and Nano Mechanical Testing of Materials and Devices: Technology & Engineering*, 2009.
- [52] S. A. H. W.W. Milfiganl, M. Ke, "IN SITU STUDIES OF DEFORMATION AND FRACTURE IN NANOPHASE MATERIALS," *NANOSTRUCTURED MATERIALS*, vol. 2, p. 10, 1993.
- [53] L. J. a. M. F. A. Gibson, *Cellular solids: structure and properties*, 2nd ed ed.: Cambridge University Press, 1997.
- [54] J. Biener, A. M. Hodge, J. R. Hayes, C. A. Volkert, L. A. Zepeda-Ruiz, A. V. Hamza, *et al.*, "Size effects on the mechanical behavior of nanoporous Au," *Nano Letters*, vol. 6, pp. 2379-2382,

Oct 11 2006.

- [55] J. Biener, A. M. Hodge, A. V. Hamza, L. M. Hsiung, and J. H. Satcher, "Nanoporous Au: A high yield strength material," *Journal of Applied Physics*, vol. 97, Jan 15 2005.
- [56] Y. Sun, J. Ye, Z. Shan, A. M. Minor, and T. J. Balk, "The mechanical Behavior of nanoporous gold thin films," *Jom*, vol. 59, pp. 54-58, Sep 2007.
- [57] T. J. Balk, C. Eberl, Y. Sun, K. J. Hemker, and D. S. Gianola, "Tensile and Compressive Microspecimen Testing of Bulk Nanoporous Gold," *Jom*, vol. 61, pp. 26-31, Dec 2009.
- [58] J. Weissmuller, R. C. Newman, H. J. Jin, A. M. Hodge, and J. W. Kysar, "Nanoporous Metals by Alloy Corrosion: Formation and Mechanical Properties," *Mrs Bulletin*, vol. 34, pp. 577-586, Aug 2009.
- [59] J. Erlebacher, M. J. Aziz, A. Karma, N. Dimitrov, and K. Sieradzki, "Evolution of nanoporosity in dealloying," *Nature*, vol. 410, pp. 450-453, Mar 22 2001.
- [60] D. V. Pugh, A. Dursun, and S. G. Corcoran, "Formation of nanoporous platinum by selective dissolution of Cu from Cu_{0.75}Pt_{0.25}," *Journal of Materials Research*, vol. 18, pp. 216-221, Jan 2003.
- [61] N. J. B. Lei Wang, Phillip D. Swartzentruber, "Magnesium Alloy Precursor Thin Films for Efficient, Practical Fabrication of Nanoporous Metals," *Metallurgical and Materials Transactions A*, vol. 45A, 2013.
- [62] H. Okamoto, "Mg-Si (Magnesium-Silicon)," *Journal of Phase Equilibria and Diffusion*, vol. 28, pp. 229-230, 2007.
- [63] W. C. Li and T. J. Balk, "Achieving finer pores and ligaments in nanoporous palladium-nickel thin films," *Scripta Materialia*, vol. 62, pp. 167-169, Feb 2010.
- [64] Y. Sun, K. P. Kucera, S. A. Burger, and T. J. Balk, "Microstructure, stability and thermomechanical behavior of crack-free thin films of nanoporous gold," *Scripta Materialia*, vol. 58, pp. 1018-1021, Jun 2008.
- [65] S. B. a. J. Kanungo. *Crystalline Silicon – Properties and Uses*
- [66] S. N. Sharma, G. Bhagavannarayana, U. Kumar, R. Debnath, and S. C. Mohan, "Role of surface texturization on the gas-sensing properties of nanostructured porous silicon films," *Physica E- Low-Dimensional Systems & Nanostructures*, vol. 36, pp. 65-72, Jan 2007.
- [67] P. Fauchet, "Porous Polycrystalline Silicon Thin Film Solar Cells," University of Rochester Rochester, New York 2003.
- [68] D. B. D.Sathis Kumar, "Nanostructured Porous Silicon-A Novel Biomaterial for Drug Delivery," *International Journal of Pharmacy and Pharmaceutical Sciences*, vol. 1, p. 9, 2009.
- [69] J. James A. Corno, "Structural And Chemical Modification of Porous Silicon for Energy Storage And Conversion " Doctor of Philosophy, School of Physics, Georgia Institute of Technology April 2008.
- [70] E. V. Astrova, G. V. Fedulova, I. A. Smirnova, A. D. Remenyuk, T. L. Kulova, and A. M. Skundin, "Porous silicon based negative electrodes for lithium ion batteries," *Technical Physics Letters*, vol. 37, pp. 731-734, 2011.
- [71] J. Cho, "Porous Si anode materials for lithium rechargeable batteries," *Journal of Materials Chemistry*, vol. 20, p. 4009, 2010.
- [72] M. Holzapfel, H. Buqa, L. J. Hardwick, M. Hahn, A. Würsig, W. Scheifele, *et al.*, "Nano silicon for lithium-ion batteries," *Electrochimica Acta*, vol. 52, pp. 973-978, 2006.

- [73] J. R. Szczech and S. Jin, "Nanostructured silicon for high capacity lithium battery anodes," *Energy & Environmental Science*, vol. 4, p. 56, 2011.
- [74] B. Hamilton, "Porous Silicon," *Semiconductor Science and Technology*, vol. 10, pp. 1187-1207, Sep 1995.
- [75] Y. Liu, Z. H. Xiong, Y. Liu, S. H. Xu, X. B. Liu, X. M. Ding, *et al.*, "A novel method of fabricating porous silicon material: ultrasonically enhanced anodic electrochemical etching," *Solid State Communications*, vol. 127, pp. 583-588, Aug 2003.
- [76] N. K. Ali, M. R. Hashim, and A. A. Aziz, "Pulse Current Electrochemical Deposition of Silicon for Porous Silicon Capping to Improve Hardness and Stability," *Electrochemical and Solid State Letters*, vol. 12, pp. D11-D14, 2009.
- [77] J. Z. Fang Dai, Ran Yi, "Bottom-up synthesis of high surface area mesoporous crystalline silicon and evaluation of its hydrogen evolution performance," *Nature Communication*, 2014.
- [78] X. Lu, T. J. Balk, R. Spolenak, and E. Arzt, "Dealloying of Au-Ag thin films with a composition gradient: Influence on morphology of nanoporous Au," *Thin Solid Films*, vol. 515, pp. 7122-7126, Jun 25 2007.
- [79] L. Wang, "Structural Tailoring of Nanoporous Metals and Study of Their Mechanical Behavior," Chemical and Materials Engineering, University of Kentucky, 2013.
- [80] J. Schoop and T. J. Balk, "Engineering Defect-Free Nanoporous Pd from Optimized Pd-Ni Precursor Alloy by Understanding Palladium-Hydrogen Interactions During Dealloying," *Metallurgical and Materials Transactions a-Physical Metallurgy and Materials Science*, vol. 45A, pp. 2309-2314, Apr 2014.
- [81] Z. D. Lu, N. Liu, H. W. Lee, J. Zhao, W. Y. Li, Y. Z. Li, *et al.*, "Nonfilling Carbon Coating of Porous Silicon Micrometer-Sized Particles for High-Performance Lithium Battery Anodes," *Acs Nano*, vol. 9, pp. 2540-2547, Mar 2015.
- [82] Y. Yao, M. T. McDowell, I. Ryu, H. Wu, N. A. Liu, L. B. Hu, *et al.*, "Interconnected Silicon Hollow Nanospheres for Lithium-Ion Battery Anodes with Long Cycle Life," *Nano Letters*, vol. 11, pp. 2949-2954, Jul 2011.
- [83] Z. Y. Jiang, C. L. Li, S. J. Hao, K. Zhu, and P. Zhang, "An easy way for preparing high performance porous silicon powder by acid etching Al-Si alloy powder for lithium ion battery," *Electrochimica Acta*, vol. 115, pp. 393-398, Jan 1 2014.
- [84] T. J. B. Xu Jiang, "New Fabrication Method of Nanoporous Silicon via Dealloying in H₂O."
- [85] W. C. Li and T. J. Balk, "Effects of substrate curvature on dealloying of nanoporous thin films," *Scripta Materialia*, vol. 61, pp. 1125-1128, Dec 2009.
- [86] F. Ostlund, K. Rzepiejewska-Malyska, K. Leifer, L. M. Hale, Y. Y. Tang, R. Ballarini, *et al.*, "Brittle-to-Ductile Transition in Uniaxial Compression of Silicon Pillars at Room Temperature," *Advanced Functional Materials*, vol. 19, pp. 2439-2444, Aug 10 2009.
- [87] A. J. Lockwood and B. J. Inkson, "In situ TEM nanoindentation and deformation of Si-nanoparticle clusters," *Journal of Physics D-Applied Physics*, vol. 42, Feb 7 2009.
- [88] E. A. Stach, T. Freeman, A. M. Minor, D. K. Owen, J. Cumings, M. A. Wall, *et al.*, "Development of a nanoindenter for in situ transmission electron microscopy," *Microscopy and Microanalysis*, vol. 7, pp. 507-517, Nov-Dec 2001.
- [89] R. C. Hughes and W. K. Schubert, "Thin-Films of Pd/Ni Alloys for Detection of High Hydrogen Concentrations," *Journal of Applied Physics*, vol. 71, pp. 542-544, Jan 1 1992.

- [90] J. P. R. Delmelle, "In-situ Study of Hydriding Kinetics in Pd-based Thin Film Systems," presented at the 18th World Hydrogen Energy Conference 2010 - WHEC 2010, Essen, 2010.
- [91] G. Korotcenkov. (2013). *Handbook of Gas Sensor Materials: . Volume 1: Conventional Approaches*.
- [92] P. Moriarty, "Nanostructured materials," *Reports on Progress in Physics*, vol. 64, pp. 297-381, Mar 2001.
- [93] Z. H. Zhang, Y. Wang, Z. Qi, W. H. Zhang, J. Y. Qin, and J. Frenzel, "Generalized Fabrication of Nanoporous Metals (Au, Pd, Pt, Ag, and Cu) through Chemical Dealloying," *Journal of Physical Chemistry C*, vol. 113, pp. 12629-12636, Jul 23 2009.
- [94] Y. Ding and M. W. Chen, "Nanoporous Metals for Catalytic and Optical Applications," *Mrs Bulletin*, vol. 34, pp. 569-576, Aug 2009.
- [95] J. Snyder, P. Asanithi, A. B. Dalton, and J. Erlebacher, "Stabilized Nanoporous Metals by Dealloying Ternary Alloy Precursors," *Advanced Materials*, vol. 20, pp. 4883-+, Dec 17 2008.
- [96] R. L. Xin, B. Li, L. Li, and Q. Liu, "Influence of texture on corrosion rate of AZ31 Mg alloy in 3.5 wt.% NaCl," *Materials & Design*, vol. 32, pp. 4548-4552, Sep 2011.
- [97] W. C. Li and T. J. Balk, "Achieving finer pores and ligaments in nanoporous palladium–nickel thin films," *Scripta Materialia*, vol. 62, pp. 167-169, 2010.
- [98] J. Erlebacher, "An atomistic description of dealloying - Porosity evolution, the critical potential, and rate-limiting behavior," *Journal of the Electrochemical Society*, vol. 151, pp. C614-C626, 2004.
- [99] L. H. Qian and M. W. Chen, "Ultrafine nanoporous gold by low-temperature dealloying and kinetics of nanopore formation," *Applied Physics Letters*, vol. 91, Aug 20 2007.
- [100] Y. Sun, K. P. Kucera, S. A. Burger, and T. John Balk, "Microstructure, stability and thermomechanical behavior of crack-free thin films of nanoporous gold," *Scripta Materialia*, vol. 58, pp. 1018-1021, 2008.
- [101] L. Wang and T. J. Balk, "Using Multilayer Precursors to Create Nanoporous Gold and Nanoporous Iridium Thin Films with Layered Architecture," *Metallurgical and Materials Transactions a-Physical Metallurgy and Materials Science*, vol. 45A, pp. 1096-1100, Mar 2014.
- [102] Y. Sun and T. J. Balk, "A multi-step dealloying method to produce nanoporous gold with no volume change and minimal cracking," *Scripta Materialia*, vol. 58, pp. 727-730, 2008.
- [103] L. Wang, and T. J. Balk, "Synthesis of Nanoporous Nickel Thin Film from Various Precursors," *Philos. Mag. Lett.*
- [104] J. R. Hayes, A. M. Hodge, J. Biener, A. V. Hamza, and K. Sieradzki, "Monolithic nanoporous copper by dealloying Mn–Cu," *Journal of Materials Research*, vol. 21, pp. 2611-2616, 2011.
- [105] X. J. a. T. J. Balk, "Novel Method for Fabrication of Nanoporous Silicon via Dealloying in H₂O."
- [106] X. Wang, W. Wang, Z. Qi, C. Zhao, H. Ji, and Z. Zhang, "High catalytic activity of ultrafine nanoporous palladium for electro-oxidation of methanol, ethanol, and formic acid," *Electrochemistry Communications*, vol. 11, pp. 1896-1899, 2009.
- [107] M. Hakamada and M. Mabuchi, "Preparation of Nanoporous Palladium by Dealloying: Anodic Polarization Behaviors of Pd-M (M=Fe, Co, Ni) Alloys," *Materials Transactions*, vol. 50, pp. 431-435, 2009.
- [108] M. Hakamada and M. Mabuchi, "Fabrication of nanoporous palladium by dealloying and its thermal coarsening," *Journal of Alloys and Compounds*, vol. 479, pp. 326-329, 2009.

- [109] A. N. a. P. Nash, "The Ni-Pd (Nickel-Palladium) System " *Bulletin of Alloy Phase Diagrams* vol. 5, p. 5, 1984.
- [110] P. V. Petrenko, A. V. Gavriyuk, N. P. Kulish, N. A. Mel'nikova, and Y. E. Grabovskii, "Structural Changes during Annealing of Deformed Pd-25 at % Ni Alloy," *Physics of Metals and Metallography*, vol. 108, pp. 449-454, Nov 2009.

Vita

Xu Jiang was born in JiXi, HeiLongjiang, China. She received the Bachelor's degree in Materials Science and Engineering from University of Science and Technology Beijing (USTB, Beijing, China) in 2005. After received the Master degree from the same department in USTB in 2008 she worked in RADI Beijing, Inc. as a mechanical Engineer. In 2010, she joined Dr. Balk's group in University of Kentucky to start a Ph.D. study in Materials Science and Engineering.

Presentations in conference

- Xu Jiang, Thomas John Balk, New Method to Fabricate Nanoporous Silicon for Lithium Ion Batteries, TMS 2012
- Lei Wang, Xu Jiang and Thomas John Balk , Structure and Thermal-Mechanical Behavior Study of Nanoporous Nickel Thin Films, TMS 2012
- Xu Jiang, Eita Tochigi, Andrew M Minor, T. John Balk, Xu Jiang, Eita Tochigi, Andrew M Minor, T. John Balk, TMS 2013
- Xu Jiang, Nicolas J. Briot, T. John Balk, Response of Nanoporous Palladium Thin Films to Hydrogen Gas (Poster), TMS 2013
- Xu Jiang, Thomas John Balk, Mechanical Behavior of Dealloyed Nanoporous Silicon, TMS 2014

Papers

- Xu Jiang and T. John Balk, Novel Method for Fabrication of Nanoporous Silicon via Dealloying in H₂O

- Xu Jiang and T. John Balk, Nanoporous Si Thin film Negative Electrode
Lithium Ion Battery
- Xu Jiang and T. John Balk, Mechanical behavior of nanoporous Silicon
- Xu Jiang and T. John Balk, Response of nanoporous Palladium thin films to
hydrogen gas